Characterization of Melanoma Brain Metastasis Cell Lines

Ole Vidhammer Bjørnstad

This thesis is submitted in partial fulfilment of the requirements for the degree of Master in Medical Biology - Biomedicine

The Faculty of Medicine and Dentistry - Department of Biomedicine

University of Bergen

Spring 2019

Acknowledgements

I would like to extend my sincerest gratitude to Professor Frits Thorsen for the pragmatic guidance and support you have given me throughout this project.

My thanks to Stian Knappskog for sequencing and initial analysis of the genomic data. Many thanks to the core facility personnel who have introduced me to instruments around the faculty. An especial thanks to Hans Olav Rolfnes for introducing me to MR imaging and tolerating my excessive questioning, Linda Sandven for the help preparing tissue samples, Endy Spriet for introducing me to the IncuCyte and finally Brith Bergum for introducing me to flow cytometry and showing me its analysis process.

I would like to express my most heartfelt thanks to all members of the Brain Metastasis Research Lab. I cannot imagine working with a more supportive and caring bunch. A special thanks to Himal for the animal handling training, showing me how to prepare cell for injections, MRI help and general cell culture. To Tuyen, thanks for the help with cell culture, showing me how to freeze down cells and general questions about the lab and finally a thank you to Krister, Synnøve and Jiwei for help with the MRI and great conversations.

I would like to mention Agathe & Christina for giving me such a warm welcome to the lab and for spending countless hours of way too long lunchtime conversations, wine clubs and group office therapy sessions. Thank you to Trond Are for all the great laughs we have had in the lab. I would like to thank Emma for the immense support you have given me and the help you have provided by editing my thesis.

My sincerest love to all the friends around Bergen who have encouraged and inspired me throughout the journey this master's has been.

Finally, I would like to thank my parents and sisters for the unconditional love and help you have offered through every step of this process.

Bergen, May 2019
Ole Vidhammer Bjørnstad

Table of contents

List of Abbreviations

Abbreviation	Full name
Av	Annexin V
BSC	Basal cell carcinoma
BBB	Blood-brain barrier
BDNF	Brain-derived neurotrophic factor
COSMIC	Catalogue of somatic mutations in cancer (COSMIC)
CNS	Central nervous system
CTC	Circulating tumor cells
CA	Contrast agent
CDKN2A	Cyclin-dependent kinase Inhibitor 2A
CPD	Cyclobutene pyrimidine dimers
DMEM	Dulbecco's Modified Eagle Medium
TE	Echo time
EMT	Epithelial-to-mesenchymal transition
ECM	Extracellular matrix
FANCA	Fanconi anaemia of complementation group A
FOV	Field-of-view
FITC	Fluorescein isothiocyanate
FSC	Forward scatter
FA	Fractional anisotropy
GEMM	Genetically engineered mouse models
GDP	Guanosine diphosphate
GTP	Guanosine-5'-triphosphate
H&E	Hematoxylin and eosin
HGF	Hepatocyte growth factor
ICD	Intracardiac injection
ICA	Intracarotid injection
IV	Intravenous injection
LMWH	Low molecular weight heparin
MRI	Magnetic Resonance Imaging
mTOR	Mammalian target of rapamycin

MMP	Matrix metalloproteinases
MAPK	Mitogen-activated protein kinase
NF1	Neurofibromatosis type I
NSC	Neuronal stem cells
NTRK2	Neurotrophic receptor tyrosine kinase 2
NHW	Non-Hispanic white
PFA	Paraformaldehyde
PTEN	Phosphatase and tensin homolog protein
PBS	Phosphate-buffered saline
PIP2	Phosphatidylinositol-4, 5-bisphosphate
PIP3	Phosphatidylinositol-3, 4, 5-triphosphate
PS	Phosphatidylserine
PI3K	Phospho-inositide-3 kinase
PI	Propidium iodide
BRAF	Proto-oncogene B-Raf
RF	Radiofrequency
RARE	Rapid acquisition with relaxation enhancement
ROI	Region of interest
TR	Repetition time
SSC	Side scatter
SNV	Single nucleotide variants
SSC	Squamous cell carcinoma
SRS	Stereotactic radiosurgery
T1w	T1 weighted
T2w	T2 weighted
TJ	Tight junctions
T1	Time point of 63 % recovery of longitudinal magnetization
T2	Time point of 37 % decary of transverse magnetization
TGF-B	Transforming growth factor-beta
M_{xy}	Transversal magnetization
M_z	Longitudinal magnetization
TrkB	Tropomyosin receptor kinase B
p53	Tumor protein 53
TNM	Tumor-node-metastasis

UV	Ultraviolet
WBRT	Whole brain radiation therapy

Summary

Brain metastasis is a major public health problem. Metastatic brain tumors are ten times more common than that of all other primary brain tumors combined. The estimated annual incidence in Europe is around 1.5 million cases per year and is increasing at an alarming rate. The majority of brain metastases originate from cancers in lung, breast or skin (melanoma). Untreated, the median survival time is around 1 month, while aggressive treatment (combinations of surgery, chemotherapy, radiotherapy and radiosurgery) extends survival to around 4 months.

In order to study the brain metastatic process, suitable animal models are needed. In this thesis, I developed several tumor/novel model systems, by injecting human patient derived metastatic tumor cell lines from melanoma intracardially into nod/scid mice. The tumor take in the mouse brains varied, depending on cell type. In H2 injected mice, all 5 mice developed one large and 1-5 small brain metastases, all with circumscribed borders. All H3 injected mice died shortly after injection of the cancer cell suspension. The one surviving mouse injected with the H5 cell line and the one surviving mice injected with H9 cells did not develop tumors. The H6 cell line proliferated too slow *in vitro* to produce enough cells for intracardial injections. Three of the H10 injected mice produced a large number of tumors with low tumor volumes. All Melmet 1 injected mice developed brain metastases, with four of them developing a large number and volume of tumors. All Melmet 5 injected mice developed brain metastases, however less in numbers and volumes than seen in Melmet 1 injected mice.

The mutational analysis showed that all 7 cell lines harbored BRAF mutations (6-BRAFV600E, 1-BRAFL577F), and to various degrees, mutations in CDKN2A, NRAS, PTEN and TP53.

A cell proliferation assay showed that the *in vitro* growth characteristics of the cells correlated to the growth patterns seen *in vivo*. A cell cycle assay by flow cytometry demonstrated that the Melmet 1 and 5 cell lines were in a relatively high S-phase percentage value compared to the H2 and H10 cell lines. An apoptosis assay by flow cytometry was used to check if there were any abnormal apoptotic tendencies *in vitro,* however this was not observed.

In conclusion, four novel melanoma brain metastasis models using the H2, H10, Melmet 1 and Melmet 5 cell lines have been developed and characterized.

1. Introduction

1.1 Epidemiology, Survival and Mortality of Skin Cancer

Skin cancers are neoplastic growth of skin related cells, of which there are three main types. The two most common types are basal cell carcinoma (BSC) and squamous cell carcinoma (SSC)[1] . BSC is derived from basal cells (Figure 1.1). Basal cells are found at the bottom layer of the epidermis, where they produce new epithelial cells. SSC is derived from squamous cells of the epidermis, which constitute most of the epidermis [2]. It is difficult to find reliable statistics about the prevalence of BSC and SCC, since these diagnoses are often omitted from cancer statistics, based on the minimal threat they pose to the patient [3]. However, the incidence rates are believed to be rising, and likely subcutaneous BSC and SCC accounts for around 65-75% and 20-30% of the skin cancers in the US, respectively [4].

The last type of skin cancer is malignant melanoma, referred to from here on as melanoma. Melanoma is derived from melanocytes [5], which are usually found in the basal layer of the epidermis, where they produce the pigment molecule melanin (Figure 1.1).

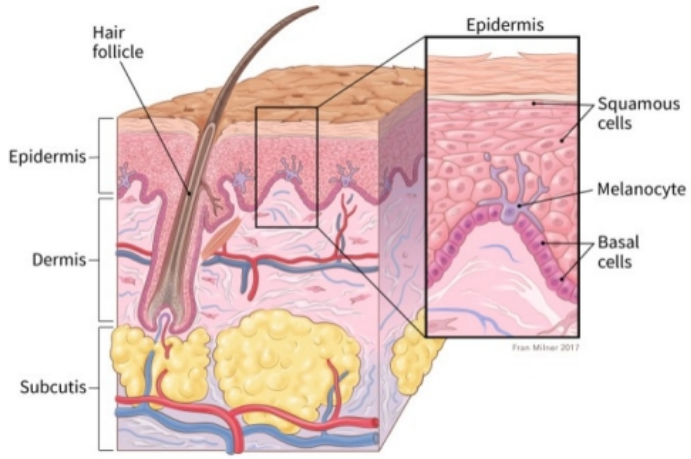

Figure 1.1 – Composition of the skin layer. Illustration of the skin, showing representative locations of the squamous cell layer, basal cell layer and melanocytes within the skin. Figure from the American Cancer Society (cancer.org) [1]

Melanoma is the most aggressive and lethal of all skin cancers, responsible for 80% of the skin cancer related deaths, while only accounting for around 5% of all skin cancers registered [6]. The incidence of melanoma world-wide is also increasing by 4-6% every year [7]. In the US,

it is estimated that there will be around 96480 new melanoma patients in 2019, and around 13% of these patients are expected to die [7].

In Norway, melanoma incidence including both invasive and non-invasive melanoma, is increasing steadily [8]. For men, the incidence rate per 100 000 was 31,1 in 2008 and 45,7 in 2017. For women, the yearly incidence rate increased from 25,4% to 38,2% during the same time period. Thus, there has been a large increase in melanoma prevalence for both genders the last years. Regarding 5-year relative survival rates per 100 000, localized melanoma increased from 70,5% for males and 86,1% for women during 1978-1982 to 90,6% and 93,9% during 2013-2017. For melanoma which induced distant metastasis, the 5-year survival changed from 7,0% for males and 22,7% for women during 1978-1982 to 22,7% and 39,4% during 2013-2017.

1.2 Causes and Risk Factors of Melanoma

There are several known causes of melanoma. The most important being exposure to ultraviolet (UV) light from sun tanning, especially for the older generation, but also the use of tanning beds for the younger generations [8]. A pigment group called melanin, originally produced in melanocytes, is able to absorb 99,9% of the incoming UV-light [8]. UVA plays a minor role in the suppression of the immune system and may also produce oxidative products which can damage DNA and induce cyclobutene pyrimidine dimers (CPD) and 6-3 photoproducts formation, both being dimerization by DNA bases. However, the effects of UVA are minimal compared to the main mutagenic driver which is UVB. UVB light, with a wavelength of 290-320nm is the most energic and carcinogenic of UV light absorbed by the skin, and is directly absorbed by DNA, producing CPD dimers 6-3 photoproducts directly. UVC is completely absorbed by the atmosphere and its relevance to melanoma is therefore nonexistent.

There are also other exogenous and endogenous risk factors which have been shown to play a role in the development of melanoma. The risk of developing melanoma may be increased up to 10-fold if a person harbors acquired melanocytic nevi, also known as moles [9]. Lower nevus counts could be seen in children who regularly applied sunscreen, compared to those who did not.

Ethnicity also plays a role for melanoma risk factors [10]. Regarding Hispanic people and non-Hispanic white (NHW) people in California, although NHW had a higher incidence of melanoma, Hispanic people harbored thicker melanomas and generally had a worse outcome than NHW harboring melanoma. When comparing African American people to NHW people in the US, incidence rates per 100 000 increases from 1,1% to 27,5%, respectively, showing a clear correlation with skin color [11]. It also seems that melanoma has a genetic heritability factor, with some low susceptibility genes being inherited, as 5-10% of melanoma incidences tend to be familial, with a high correlation of the gene cyclin-dependent kinase inhibitor 2A (CDKN2A) being mutated [12,13].

1.3 Biological Aspects of Melanoma

Melanocytes are neural crest derived cells and are mostly found in the basal layer of the epidermis and hair follicles [13]. However, populations of melanocytes can also be found in the uvea of the eye, stria vascularis within the cochlea of the ear, mucosal surfaces of the gastrointestinal tract, the urogenital tract and in the meninges. [14]. The main goal of melanocytes is to produce melanin. Production of cutaneous melanin is conducted in a specialized membrane-bound, lysosome-related organelle called the melanosome, before further transport into adjacent keratinocytes, for protection against UV light [15]. The melanin pigments produced have been broadly classified in the groups pheomelanin and eumelanin [16]. Pheomelanin encompasses the red/blonde pigments and eumelanin the brown/black pigments. Regarding UV radiation, pheomelanin pigments offers weak shielding capacity compared to eumelanin pigments, and have also been shown to amplify UVA induced reactive oxygen species [17]. Despite varying constitutive pigmentation, people seem to have a fixed number of cutaneous melanocytes, so different skin color seems to arise from the type of melanin expressed and the degree of expression.

1.4 Molecular Aspects of Melanoma

There are several signaling pathways which have been shown to be important for the initiation and development of melanoma, the most important ones being the mitogen-activated protein kinase (MAPK) pathway, and the phospho-inositide-3 kinase (PI3K) pathway [18]. Mutations in genes within signaling pathways may lead to uncontrolled cellular proliferation [19]. Mutations in tumor suppressor genes, such as CDKN2A, inhibits the ability of cells to turn off

intracellular, proliferative signaling [20], while mutations can also induce the transition of a proto-oncogene into an oncogene. Oncogene activation induces continuous activation of proliferative signals [21]. Upon activation of oncogenes and inactivation of tumor suppressor genes, the cells will have increased genome instability upon replication, eventually leading to additional mutations within the cellular genome [22].

The most prevalent mutations found in melanoma appear in the proto-oncogene B-Raf (BRAF) [23]. BRAF, a member of the Raf kinase family, plays an important role in the MAPK signaling pathway, which mediates cellular responses to growth signals [24]. Mutations in this pathway lead to increased replicative potential, apoptosis evasion and angiogenesis. The mutation frequency of the BRAF gene is around 41-66% in melanoma, mostly within the kinase domain of the protein [25–27]. The most common mutation within BRAF is the BRAFV600E mutation, constituting 80% of total BRAF V600 mutations, substituting valine (V) to glutamic acid (E), in the kinase domain of BRAF [25,28]. Other frequent activation mutations are also seen, such as BRAFV600K and BRAFV600R [29]

The second most common oncogenic mutation in melanoma is within the Ras family of small GTPases (15-20%) [30]. These mutations are mostly found within the GTPase domain of the protein, often with multiple substitutions at Q61, most commonly Q61R or Q61K. The three genes coding for the Ras family are NRAS, HRAS and KRAS [31]. Ras family proteins are plasma membrane-associated GTP-binding enzymes, involved in the MAPK pathway by activating Raf. During an oncogenic mutation, a defective Ras will activate Raf constitutively, thereby increasing cell proliferation [32].

Neurofibromatosis type I (NF1) is one of the most frequently mutated genes in melanoma (12-18 %), with R440 substitution being the most common mutation [33]. NF1 is a tumor suppressor gene that negatively regulates the MAPK pathway through the hydrolysis of Guanosine-5'-triphosphate (GTP) into Guanosine diphosphate (GDP) bound to NRAS. When mutated, the deactivation of MAPK pathway is turned off. Although the NF1 gene contains a high frequency of mutations, there is no specific domain overrepresented for substitutional mutations, as seen in other oncogenic mutations such as BRAF [30].

Another commonly over-activated pathway in melanoma is the PI3K pathway, often due to the loss of function of the phosphatase and tensin homolog protein (PTEN), through mutation,

deletion or methylation. PTEN is a tumor suppressor protein, acting as a phosphatase on phosphatidylinositol-3, 4, 5-triphosphate (PIP3) into phosphatidylinositol-4, 5-bisphosphate (PIP2), preventing PDK1 binding and subsequent Akt binding and activation, leading to downregulation of the PI3K pathway. Loss of PTEN function is seen in between 10% to 30% of melanomas and is commonly associated with the $BRAF^{V600E}$ mutation. Increased activity in the PI3K pathway has also been related to an acquired resistance to BRAF and MEK inhibitors after therapy[29].

1.5 Grading and Staging of Melanoma

Grading- and staging systems are used to classify the anatomic extent of a cancer, and to quantify the expansion and malignant capabilities of the primary tumor. As melanoma is one of the most aggressive human cancers, grading aims to distinguish the extent of melanoma aggressiveness and categorize the cancer into Grades I-IV [21] [34]. Grade I is a slow growing tumor, the cells look morphologically normal, and metastasis is unlikely. For patients with Grade I tumors, surgery is the preferred option for treatment. A Grade II tumor contain tumor cells with a higher proliferative capacity than a Grade I tumor, the cells appear more abnormal, but metastasis is unlikely. However, the tumor is more likely to reoccur after local, surgical treatment. A Grade III tumor is rapidly expanding, cells are very abnormal, but the tumor does not contain any necrotic tissue. A Grade IV tumor is rapidly expanding, contains highly undifferentiated cells, the tumor is necrotic and the cancer cells are inducing angiogenesis of nearby blood vessels.

Staging is used to properly assign a prognosis and to determine the most suitable treatment for melanoma [35]. In staging, the expansion of the primary tumor as well as the extent of metastatic spread is determined. Staging is more focused on metastasis than the abnormal cell growth of the primary tumor. The staging system most widely used for melanoma is the tumor-node-metastasis (TNM) staging system [36]. Within the TNM system, T denotes the extent of the primary tumor, by either expansion or malignancy into nearby tissue. N denotes regional lymph node cancer expansion. M denotes the presence of metastases to organs that are not the regional lymphatic vessels near the primary tumor, often called distant metastases [37] .

Melanomas can then be grouped into stages 0-IV [38]. Stage 0 melanoma is often called cancer *in situ,* a neoplasm without classic cancerous traits, such as rapid expansion and metastases, and can be easily treated with surgery. Stage I encompasses a melanoma that has not spread deeply into nearby tissues or lymph nodes, with its thickness being under 2mm and no ulceration is shown. A stage II melanoma is a localized tumor that is over 2 mm thick, and ulcerates. For a stage III melanoma, thickness and depth is no longer accounted for, and it can be ulcerated or not. Stage III is categorized as a melanoma that is involved with the regional lymph nodes. Stage IV tumors have metastasized beyond regional lymph nodes and into distant organs.

1.6 The Metastatic Process

The invasion of cancer cells from the main tumor mass and into distant tissues and organs of the body is known as metastasis. Metastasis induces systemic failure, and is the main cause of mortality in cancer patients [39]. When a tumor harbors the ability to metastasize, the tumor is classified as malignant [40]. Shedding of metastatic cancer cells into the circulatory system may happen early or late in cancer development, after which metastatic cells will invade distant organs by the use of lymphatic or hematogenous dissemination [41].

Metastasis can be divided into five main steps: Local invasion, intravasation, transport, extravasation and metastatic colonization [42]. To begin the metastatic process, cancer cells must first break free from cell-cell adhesion constraints found within the tumor mass to invade local tissues. Therefore, the first step of metastasis is an epithelial-to-mesenchymal transition (EMT) of the tumor cells [43]. EMT starts when the cancer cells get stimulated for transition into a more mobile, undifferentiated mesenchymal cell type. EMT may be stimulated by fibroblasts in the tumor stroma, which release growth factors such as transforming growth factor-beta (TGF-B) and hepatocyte growth factor (HGF) [44]. During transition, cell polarity and cell-cell adhesion molecules such as E-cadherin, are lost and mesenchymal proteins such as N-cadherin and fibronectin are upregulated.

Metastatic cells must also free themselves from the surrounding, rigid extracellular matrix (ECM) [45]. Altered integrin receptor expression and degradation of the ECM by serine proteases and matrix metalloproteinases (MMPs) enable the cancer cells to move into nearby tissue. Such altered expression is typical for melanoma, where the leading edge of the cancer

cell has a distinct integrin $\alpha_v\beta_3$ expression profile, likely preventing anoikis and increasing cell motility [46].

As the cancer cells invade local tissue, they will eventually reach a blood or lymphatic vessel [47]. Intravasation is the process of cancer cells to traverse the endothelial wall of a vessel, through the release of MMPs, which through enzymatic activity will allow the cancer cells to enter the circulation. Once inside a vessel, the cancer cells can circulate throughout the body (step 3 – transport)[48].

There are two main ways for circulating tumor cells (CTCs) to halt their journey throughout the circulatory system, either through molecular attachment to endothelial cells or by mechanical force [40]. Mechanically, CTCs are more likely to metastasize to organs *en route*, to the first organ encountered by the circulation system, from the primary tumor site. *En route* metastasis is thought of as frequent since tumor cells are generally 20 um, while a capillary is around 3-8 um, trapping CTC in the capillaries [49]. During molecular attachment, selectins and integrins act as brakes for CTCs, binding them to the endothelium cells of the hematological circulation system, enabling extravasation [50].

Once the CTCs stop within the circulation system, they will start the step of extravasation (step 4) [51]. Extravasation is the process of CTCs crossing from the luminal side of the vessel, through or between the endothelial cells of the vessel wall and into the tissue of the secondary organ. This is aided by degradation of the cell-cell adhesion molecules and the basement membrane by MMPs [52].

The final step in the metastatic process is metastatic colonization and tumor outgrowth [42]. As cancer cells are dependent on the new local environment of the organ to expand, metastatic cells may lie dormant for long periods of time before colonizing an organ [53]. It is also likely that the metastatic cells must go through a mesenchymal-epithelial transition before colonization. As the tumor starts to grow in the secondary site, an increased blood supply is needed [54]. Angiogenesis and lymphangiogenesis, formation of new blood and lymph vessels, will therefore be induced by the tumor cells to provide nutrients and tumor waste drainage.

It should be noted that the metastatic process is highly ineffective, with only around 0,01% of the CTC present in the circulatory system being able to form metastatic foci [55] [40].

1.7 The Blood-Brain Barrier (BBB)

The blood-brain barrier (BBB) is a dynamic and selective diffusion barrier that selectively regulates the transport of molecules and substances between the blood and the brain. The BBB consist of brain endothelial cells, interconnected by tight junctions (TJ), which are situated on a basal lamina. The TJs help to maintain a diffusion barrier between the blood and the central nervous system (CNS), selectively excluding most blood solutes from entering the brain [56]. Pericytes are layered around the endothelial cells, providing structural support and vasodynamic capacity [57]. Finally, astrocytic end-feet cover the blood vessels, and they seem necessary for the induction and maintenance of the endothelial cell-cell adhesion characteristics of the BBB [58] (Figure 1.2).

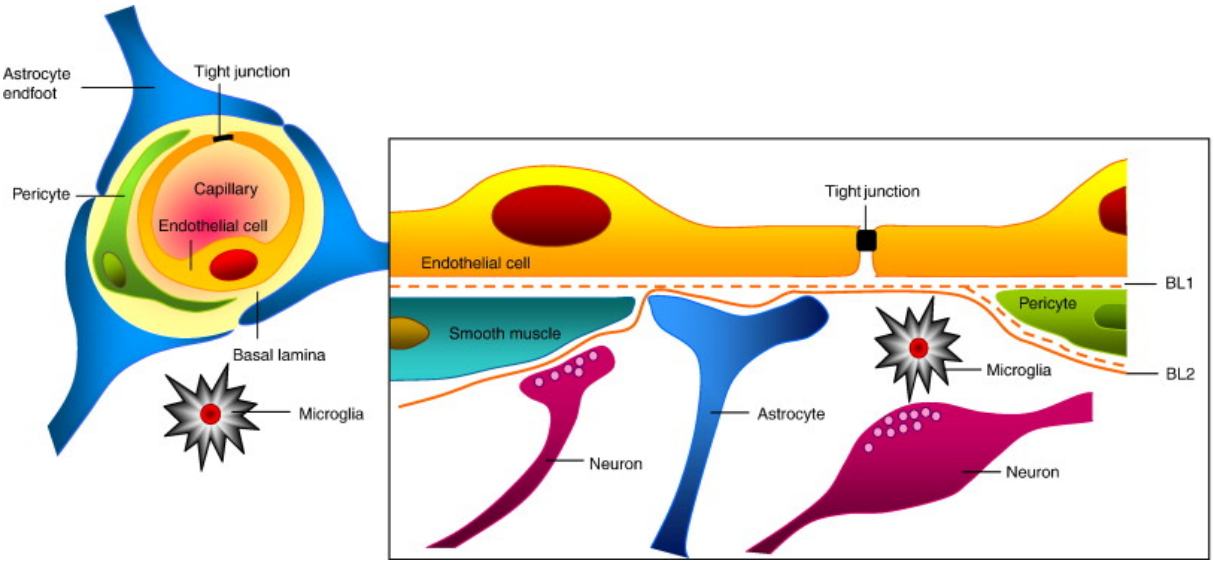

Figure 1.2 – Composition of the blood-brain barrier. Illustration of the blood brain barrier, showing the endothelial cell seals made by tight junctions, which prevents paracellular diffusion from the blood vessel to the brain. Arteriolar smooth muscle is also connected to the neurons, regulating local blood flow. Partly surrounding the endothelium, one can sporadically find pericytes. Both the basal lamina covering the endothelial cells (BL1) and the basal lamina binding the brain parenchyma (BL2) aids in the structural upholding of the BBB, where astrocytic end-feet initiate and maintains barrier properties. The microglia are the dwelling immune cells of the brain. Figure from Abbott, Patabendige, Dolman, Yusof, & Begley, 2010.

The BBB prevents cells and large or hydrophilic molecules from entering the CNS from the blood [59]. This makes drug treatment of brain metastases challenging, as ~100% of large-molecule drugs and more than 98% of small-molecule drugs are not able to cross the BBB [60]. For a drug to pass the BBB, it must have a molecular mass under 400-500 Da and a high lipid solubility[60].

1.8 Brain Metastasis

Brain metastases are the most common type of malignant tumors in the brain [61]. In the US, it is estimated that there are around 200 000 new brain metastases cases every year, and between 20% and 40% of all systemic cancer patients eventually develop brain metastases [62] [63]. The three most common cancers metastasizing to the brain are lung cancer (50-60%), breast cancer (20-30%) and melanoma (5-10%). The high mortality rates for melanoma as described above, is partly attributed to the fact that this tumor type has the highest propensity to metastasize to the brain of all cancers [64]. A study on advanced stage melanoma (stages III and IV) showed that 44% of the patients developed brain metastases. Independent factors showing increased chances of developing brain metastases were elevated levels of lactate dehydrogenase, primary tumors located in the head, neck or trunk region, increased thickness of the primary melanoma and visceral metastases [65]. The distribution of brain metastases also seems to follow the blood flow within the brain, where brain tumor occurrences prevail 80% in the cerebral hemispheres, 15% in the cerebellum and meninges and 5% are located in the brainstem [66] [67]. Patients diagnosed with brain metastases has a median survival of 1 month after diagnosis if the cancer is left untreated, and 3-4 months if treated [68].

1.9 Current Treatment of Metastatic Melanoma

The 5-year survival rate of patients with metastatic melanoma is around 5-19% and the 10-year survival is under 10%, necessitating the improvement of more aggressive therapeutics for this patient group [69,70]. Surgery, radiation therapy and systemic therapy are the main treatment choices for metastatic melanoma.

Surgery is often the first choice after diagnosis, to limit tumor expansion, as well as to reduce neurological symptoms [71]. After tumor resection, a histological and immunohistological analysis is performed to verify the origin of the tumor, thereby aiding further treatment, such as targeted therapies.

Corticosteroids and anticonvulsants are also often given as a first line treatment to relieve neurological symptoms, although they do not have an effect on decreasing the tumor burden. Corticosteroids have been shown to reduce symptoms such as brain edema, muscle weakness

or seizures in two thirds of patients with brain metastases [72]. Anticonvulsants are administered to patients who experience seizures upon tumor diagnosis.

Patients with multiple brain metastasis are commonly treated with whole brain radiation therapy (WBRT), a therapy that directs high-energy x-rays to the whole brain or to targeted areas. Low radiation doses causes chromosomal damage within the cells, subsequently inducing apoptosis, whereas high radiation doses induce tumor cell necrosis [73]. Surgery and radiation treatment are often combined in the management of brain metastasis. In the 1990s, it was shown that surgery in combination with WBRT increased the survival median to 9-10 months for patients with a single brain metastasis with no systemic spread [74,75].

In more recent years, stereotactic radiosurgery (SRS) is being used as the main treatment method for local brain metastases, in addition to surgery. SRS uses multiple radiation beams that converges into a focus point, directed to the brain tumor itself. This minimizes radiation to normal brain tissue and thus peripheral tissue damage [76]. SRS is non-invasive, therefore it is a good alternative for patients with tumors in inoperable areas of the CNS, such as the brainstem. SRS is optimal for brain metastases, as they are generally small, non-invasive and circumscribed tumors [77]. Radioresistant tumors, such as melanomas, also responds well to the high radiation doses administered by SRS. The median survival for patients treated with SRS harboring melanoma brain metastasis has been reported in a study to be 8 months with a 77,8% chance to revert or stop neurological symptom progression [78].

Systemic treatment using chemotherapeutic drugs are usually not considered for first line treatment for brain metastases, as most chemotherapeutics are large complex molecules that cannot cross an intact BBB [79,80]. However, BRAF inhibitors such as dabrafenib and vemurafenib, and anti-CTLA4 monoclonal antibodies such as ipilimumab have shown promising results in the treatment of melanoma brain metastases [81,82]. Although drug resistance has been a major problem in the treatment of melanomas, patients have had a 63% relative reduction in the risk of death and 74% reduction in disease progression when treated with vemurafenib [83]. Ipilimumab treatment inhibits CTLA-4, enabling a cytotoxic T-cell response towards cancer cells that previously evaded the immune system [84]. Ipilimumab treatment has thus been shown to be the first immunotherapeutic treatment for malignant melanoma with long-term efficacy [85]. However, a developed multi drug resistance for brain metastases continues to be problematic [86] .

Despite the many options available, current treatment strategies are not curative for patients with brain metastasis, and the patient survival is still poor, despite these aggressive therapies. There is therefore an urgent need to develop novel therapeutic strategies.

1.10 Animal Models to Study Brain Metastasis

Basic, cellular and molecular cancer research, and development of new treatment strategies is commonly first conducted in cell culture, followed by the use of murine models. Mice are the preferred model system, since mice are small in size, inexpensive to purchase and sustain, have large and frequent litters and can be genetically manipulated [87]. Tumor cells injected or induced within mice can be both murine and human derived (Figure 1.3). If human tumor materials are being used, immunosuppressed animals are utilized to prevent any immune response to the xenograft[88].

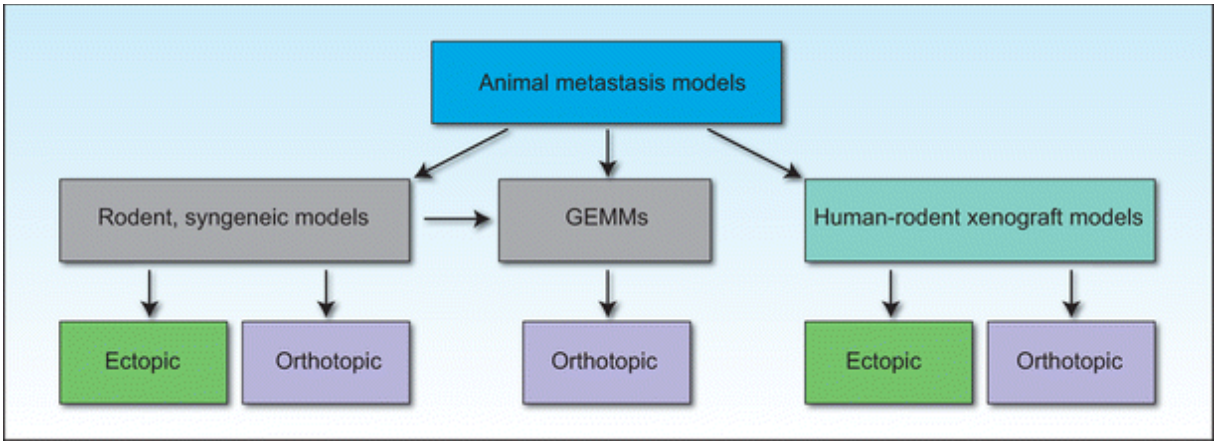

Figure 1.3 – Schematic grouping of current animal metastasis models. Current animal metastasis models that are available can be grouped based on where the tumor tissue is derived from. Tissues derived from rodents can be grouped into syngeneic models, where the tumor tissue has the same genetic background as the animal used. Two sub groups can be made within the syngeneic models: ectopic, where the tumor sample is injected into the bloodstream of the animal or orthotopic, where the tumor sample is injected into the same type of organ the sample is derived from. A parallel can be made from the syngeneic orthotopic model to a genetically engineered mouse model (GEMM), where genetic changes within the germline of the mouse induces cancer and potentially metastasis. A human-rodent xenograft model encompasses models where a human derived cancer cell line or a patient biopsy is injected into mice. An ectopic model would be the injection of human cancer cells into the bloodstream, and orthotopic is the injection of human cancer cells into the corresponding native organ in mice. Figure from [29]

1.10.1 Spontaneous Models

In rare instances, spontaneous tumors have occurred in mice kept in the laboratory [89]. Although the development of new spontaneous murine animal models is rare, they do have

certain advantages. These mice still have functioning immune systems, which can offer insight into host-tumor interactions that cannot be studied in immunodeficient mice that lack T and/or B cells. Another advantage to consider is the fact these tumors develop *de novo*. New mutations within a cancer type can thus be discovered, where spontaneous tumors might be unnoticed in a genetically inbred background [90]. However, as spontaneous autochthonous tumors are rare, the time frame for generating such models is long, and a large number of mice would also be needed, therefore such models such would be impractical in cancer research [91]. A spontaneous model also does not reflect the genetic composition of a human. Murine cancer is a murine disease, and results from a murine study likely do not reflect the human situation completely.

Other animals, such as cats and dogs, also develop tumors spontaneously. These animals have a high level of veterinary care, and consequently a substantial amount of treatment data is available [92]. Since animal companions develop similar tumors to humans in a much shorter time span and respond similar to most treatment regimes, the animal companion registries have a large potential for being used in preclinical research [93].

1.10.2 Induced Brain Metastasis Models

Induction of melanomas in mice is primarily done by exposing the animal to UV-light, but may be done by injection of carcinogenic compounds [29]. Induced tumors offer advantages similar to spontaneous models, such as tumor formation in an immunocompetent background and orthoptic primary tumor growth. An orthoptic tumor growth offers insight into tumor histology devoid of changes induced by transplantation, while also offering insight into local invasion by the primary tumor into nearby lymphatic vessels and tissue [94, 95]. However, these models also present with their own challenges. To identify mutations responsible for initiation and expansion of the primary tumor, high throughput sequencing is necessary, making this method very laborious and expensive. It can also be an unpredictable method, as tumor frequency and occurrence varies within the animal cohorts [96].

1.10.3 Genetically Engineered Mouse Models

A more reliable system of studying autochthonous cancer growth in a murine model is by the use of genetically engineered mouse models (GEMMs), where one alters the germline of the animal [97]. By utilizing targeted homologous recombination, one can disrupt or overexpress

certain genes. A knock-out GEMM has one or multiple genes inactivated, while a knock-in increases expression of a protein within the germline [98]. Generating an orthotopic primary tumor model in an immunocompetent mouse is often seen as the main advantage of a GEMM. A functional immune system enables a more complete study of the tumor stroma, homologous to the interactions seen in human tumors. GEMMs however have a low incidence of metastatic spread that can be explained by the rapid expansion of the primary tumor, and its subsequent symptoms and morbidity if not surgically removed [51]

1.10.4 Human Xenotransplantation Models

Human xenotransplantation murine models are based on the explantation of human tumor tissue and subsequent injection of the tissue or a cultured cellular suspension into immunodeficient mice [99]. An ectopic model emulates the metastatic spread of cancer by directly injecting human cancer cells into the bloodstream of the mouse. By injecting tumor cells derived from humans into the murine models and utilizing specific blood routes, one can ensure a metastatic spread which is similar to human metastatic spreading patterns. In an orthotopic model, the human tumor cells are injected directly into the corresponding murine organ [29]. Advantages of this model is that it enables testing of a wide range of human samples with their corresponding mutations. However, this model suffers from a lack of adaptive immune interactions with the immunocompromised host[51].

1.11 Routes of Tumor Cell Inoculation

In the brain metastases models mentioned above, the inoculation route during both ectopic and orthotopic injections is crucial for determining which organ are being able to establish metastases [29].

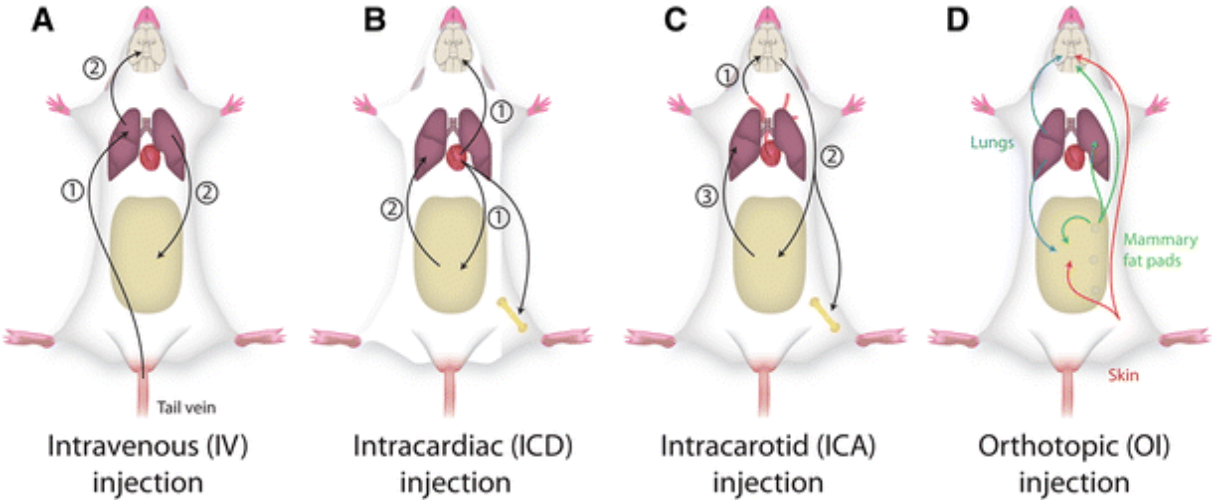

Figure 1.4 – Inoculation routes for establishment of brain metastases. The schematic represents primary (*1*), secondary (*2*) and tertiary (*3*) routes of metastases based on the original injection site. A) Following an ectopic intravenous (IV) injection, the first metastases pathway follows to the lungs (*1*), with secondary pathways from the lungs to both the brain and other organs present in the abdominal cavity (*2*). B) With ectopic intracardiac (ICD) injections, the first metastasis pathway will be to the brain, organs present in the abdominal cavity and bone (*1*) with secondary metastases from the abdominal organs to the lungs (*2*). C) Ectopic intracarotid (ICA) injections, the first metastasis pathway will be the brain (*1*), with secondary to both the abdominal cavity organs and bones (*2*), before finally as a third going from the abdominal cavity organs to the lungs (*3*). D) Regarding orthotopic (OI) injections: Initial tumor growth will happen at the injected tissue site followed by metastatic spread. Development of OI brain metastasis models have been generated for melanoma (*red arrows*), lung carcinomas (*blue arrows*) and breast carcinomas (*green arrows*). Figure from [29]

The different inoculation routes for the establishment of brain metastasis is illustrated in Figure 1.4. To emulate CTCs, tumor cells are injected into the bloodstream. The use of intravenous injection (IV) to establish brain metastases is primarily used to induce lung metastases, while the route to metastasize to the brain is secondary from the lungs when injecting IV [100]. To discriminate hematological non-brain metastasis spread after inoculation, the use of intracardiac injection (ICD) and intracarotid injection (ICA) are the most efficient. ICD and ICA injections bypass interfering sites such as the pulmonary circulation site, but do not mimic establishment of primary tumors and spread from them [101]. ICD does however metastasize to extracranial sites, considerately compared to ICA. ICA on the other hand is technically challenging and requires well-trained personnel to repeatedly perform successful injections [102]. While OI can produce metastases to the brain, the primary tumor grows quite aggressively in most cases, and must be removed to give distal metastasis time enough to develop [103].

1.12 Magnetic Resonance Imaging (MRI)

Magnetic Resonance Imaging (MRI) is a non-invasive imaging method producing detailed anatomic images without the use of ionizing radiation. Instead, MRI uses magnetic waves and

radiofrequencies [104]. The MRI machine consists of a primary magnet, gradient coils, radiofrequency (RF) coils and a computer system. The primary magnet produces a static primary magnetic field, also called B_0. Gradient coils allow special encoding for the MR images in the x, y and z axis. The RF coil will transmit a radio signal, which interacts with tissue placed within the MRI, while also detecting electromotive force (electrical actions from a non-electrical source) changes within the MR machine upon interacting with the radiofrequency signals sent out. The computer system itself will process the matrix of signals and produce an image [105].

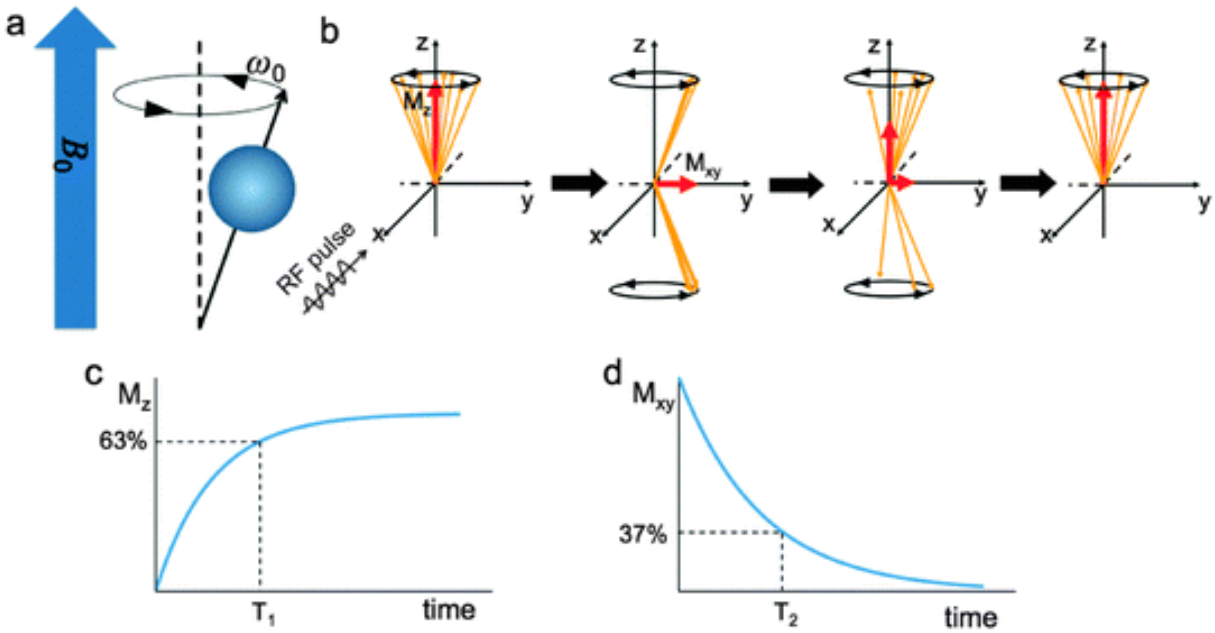

Figure 1.5 – Basic principles of MRI. (A) Showing the magnetic field B_0, with the hydrogen spin aligning parallel or antiparallel to it. (B) Upon an RF pulse, the net magnetic moment will shift in phase either parallel or antiparallel to B_0, decreasing the longitudinal magnetization (M_z) and generate a transverse magnetization (M_{xy}). After some time, the net longitudinal magnetization will decrease, and the hydrogen atoms will spin decreasingly out of phase. (C) Shows the net nuclear spin increased longitudinal magnetization over time, with T_1 being the decay constant of the polynomial function. (D) Depicts the decrease of transverse magnetization over time, with T_2 being the decay constant of the polynomial function. Figure is taken from Lee & Hyeon, 2016.

The mechanism by which the MRI detects a signal relies on the hydrogen atoms inherent magnetic properties [106]. A hydrogen atom contains a net positive charge within its nucleus, as the nucleus only consists of a proton. The positive charge will induce a spin on the proton itself, which in turn will produce a magnetic moment, as depicted by the vector in Figure 1.5A. Upon contact with B_0, the hydrogen will also undergo a physical phenomenon called Larmor precession. Larmor precession describes precession of the magnetic moment of an object, the hydrogen, under an external magnetic field, B_0, as seen in Figure 1.5A.

During B_0, the hydrogen atoms will align parallel (a lower energy state) or antiparallel to B_0 (a higher energy state). The net magnetic moment of the hydrogens produced in the z-direction under B_0 is called longitudinal magnetization (M_z), as seen in Figure 1.5B. Since antiparallel hydrogens are in a high energy state, they will eventually degenerate into the lower energy parallel state. Registering the time degradation takes, one can plot the increase of the longitudinal magnetization versus time and plot as in Figure 1.5C. To plot such a function, one assumes that longitudinal magnetization will eventually decay to equilibrium. By the function of M_z (t) = $M_{z,eq}(0)$-[$M_{z,eq}(0)$ - $M_{z,eq}$ (0)] $e^{-t/T1}$, we are left with a decay constant of 63% which is then marked as T_1 (an innate constant for every tissue, primarily depending on the number of hydrogens within the tissue). [107]

As the RF pulse interjects the system, the transversal magnetization (M_{xy}) vector will increase, as hydrogens start to precess together, as seen in Figure 1.5B. By time, the in-phase hydrogens will start to precess out of phase, decreasing M_{xy}, until the hydrogen atoms precess in a random pattern again. The transversal magnetization decay to equilibrium, zero, is described by the function of M_{xy} (t) = $M_{xy}(0)e^{-t/T2}$, which leaves us with a decay constant of 37%, which is marked as T_2 (an innate constant for every tissue, primarily depending on the number of hydrogens within the tissue). [107]

While processing images for the MRI, image contrast is based on whether T_1 or T_2 image parameters are selected. For imaging in general, both the longitudinal and transversal magnetization times varies based on the tissue composition [108]. Tissues containing a lot of water will produce a higher T_1, since the water molecules moves around more rapidly and enters a lower energy state slower. A longer T_1 will cause the longitudinal magnetization to recover slower, concurrently making water filled tissues darker areas on an MR image.

When imaging a T_2 image, the dephasing of hydrogen atoms precession is faster than mathematically expected because of field inhomogeneities in the B_0 field. Such inhomogeneities will induce a faster dephasing of T_2. When imaging tissues containing a lot of water, transversal magnetization will recover slower, because of few field inhomogeneities within the water, which in turn will cause a higher T_2 value. Transversal magnetization will thus recover slower, concurrently making water filled tissues brighter areas on an MR image[108].

A contrast agent (CA) is often injected before taking T_1 and/or T_2 images [109]. Most of current CA are paramagnetic metal ion-ligands, such as gadolinium, or superparamagnetic particles, such as ferromagnetic nanoparticles. These CA work by shortening the T_1 and T_2 values of water hydrogens by aiding degradation from a higher energy state. A T_1 CA will work by catalyzing the transition from anti-parallel to a parallel state, making longitudinal magnetization happen faster, decreasing the T_1 value. A lower T_1 value will make fluid rich tissue become brighter. A T_2 CA works by catalyzing the transition of hydrogens precessing in-phase to out of phase, inducing a faster degradation of the transversal magnetization vector and thus a lower water signal intensity. A lower T_2 value will make fluid rich tissue become darker.

1.13 Flow Cytometry

1.13.1 Basics of Flow Cytometry

A flow cytometer measures specific properties of single cells or particles which pass through a focused laser beam [110]. The cell suspension is taken up into the flow cytometer and is transported through tubing containing sheath fluid. Individual cells within this fluid will pass one by one through a laser beam, causing a scattering of the lasers light. In addition, labeled cells will emit fluorescent light when passing through the laser, which will be registered by detectors, selected by dichroic mirrors, as seen in Figure 1.5.

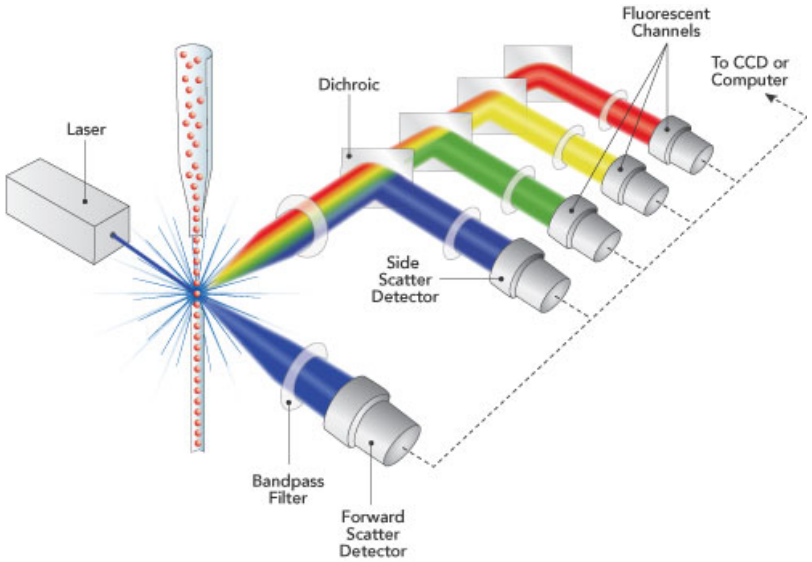

Figure 1.5 – Basic principles of flow cytometry. The figure displays a simplified display of flow cytometry. With the samples being collected at the top, mixed with the sheath fluid, for then to be sent into a line further into the machine. A laser will hit the sample events, causing both forward and side scatter. Forward scatter is picked up by the forward scatter detector. The side scatter light will be filtered by dichroic mirrors and registered by side scatter detectors. The detected signal is further analyzed *in silico*. Figure from semrock.com.

Flow cytometry measures the fluorescent characteristics of a single cell or particle [111]. Light scatter within the flow cytometer along the laser path is detected as forward scatter (FSC) and another detector will register light scatter in a 90-degree angle from the laser, called side scatter (SSC). FSC will enable discrimination based on cell size, while SSC discriminates cells based on cellular granularity, protein expression and ion concentration. Flow cytometry also enables cell discrimination based on fluorescence, by labeling proteins, lipids or structures within the cell.

Labeling can be enabled by fluorescent intercalating agents, such as propidium iodide (PI). PI intercalates with DNA and RNA, with an excitation/emission maxima of 493/636 nm. PI cannot permeate the cellular membrane, it can therefore be used as a marker for late apoptosis and necrosis, where the integrity of the cellular membrane is compromised. Another labeling commonly used is fluorescein isothiocyanate (FITC) conjugated to Annexin V (Av) [112]. Av is a protein that binds to the glycerophospholipid phosphatidylserine (PS), Ca2+ - dependently. PS is a key cell marker for apoptosis, present in the cellular membrane. PS becomes inverted from its cytosolic side at normal cell function to the extracellular side upon an apoptotic signal from the cell. Av as a protein has no inherent fluorescent activity, but it acts as a binding partner to PS. FITC is therefore conjugated to Av, making it a fluorescent marker for early and late apoptosis with an excitation/emission maxima of 495/519 nm.

1.13.2 Flow Compensation Used During Apoptosis Measurements

Compensation is an essential part of proper experimental setup for multiplexed flow assays [113]. Whenever more than one fluorescent marker is expressed on a single cell, the presence of one fluorescent marker can contribute significantly to an optical background when the fluorescent signal from the other marker is being detected. This phenomenon is called spillover. Spillover is due to the physical overlap among the emission spectra of certain commonly used fluorochromes (an example is shown in Figure 1.6). This occurs whenever the fluorescence emission of one fluorochrome is registered in a detector designated to recognize signal from another fluorochrome. The amount of spillover is a linear function, so the measured average signal levels can be corrected (i.e., the population medians aligned) by a process called compensation.

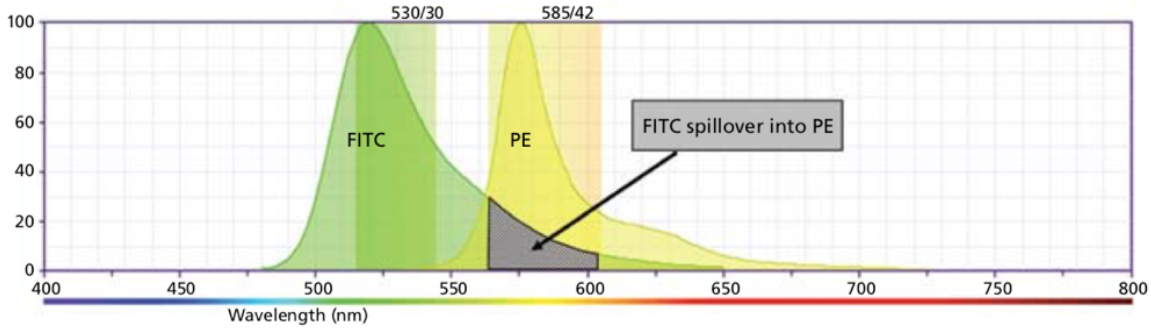

Figure 1.6. FITC spillover in the PE channel. Illustration of how the fluorescent signal tail (between 543-627nm) from FITC will be registered in the detector used to detect phycoerythrin (PE). Figure from bdbiosciences.com

The primary goal of compensation is to remove the signal from a given fluorochrome from all neighboring channels where it was also detected [114]. To correct for spillover, spectral overlap values are measured for all fluorophores and in all detectors, via single-color controls. The spillover values are then placed in a symmetrical matrix. To determine the actual compensation values for correction of the data, the measured spectral overlap values (of all colors in all detectors) are inverted by matrix algebra to yield compensation values. This matrix algebra operation calculates the simultaneous solution of the equations for the contributions of the spectral overlaps of each of the colors into every detector. Finally, the compensation values (not spectral overlap values) are used by the flow cytometer to correct the contributions of other colors overlapping into a given detector.

2. Aims

The main aim of this master thesis was to establish novel mouse metastasis models, which will be used by the research group for later preclinical and experimental testing of new treatment strategies for melanoma brain metastasis.

Five sub aims were defined within the work of this master thesis:

1. To study in detail the brain metastasis tumor expansion and spread in mice, by using 8 different human, metastatic melanoma cell lines.
2. Based on the results from sub aim 1, select the cell lines most suitable for animal work, for further *in vitro* characterization.
3. By using flow cytometry, characterize apoptosis and cell cycle profiles of the selected cell lines.
4. Use viability assays to study proliferation rates of the selected cell lines.
5. Characterize the mutational status for the selected cell lines.

3. Material and Methods

3.1 Cell Lines and Cell Culture

In this work, the following cell lines were used: H2, H3, H5, H6, H9, H10, Melmet 1 and Melmet 5. More information about the cell lines is displayed in Table 3.1. All cell lines were derived from primary melanoma tumors that had metastasized to a secondary site before being resected. All "H" cell lines were made in-house in the Brain Metastasis Research Lab. The Regional Ethical Committee (#013.09) and the Norwegian Directorate of Health (#9634) approved the tissue collection and storage. Tumor specimens were brought to the lab, minced into small pieces, and transferred to T75 culture flasks (Nunc, Roskilde, Denmark). All tumor specimens were grown in complete ALT DMEM (see below). The specimens were kept in a standard tissue culture incubator at 37 °C with 100% humidity and 5% CO2. The growth medium was exchanged twice a week. After a few weeks, monolayer cultures formed in the flasks. These were trypsinized, and frozen in aliquots in liquid nitrogen for later use (see below).

The Melmet cell lines were kind gifts from Prof. Øystein Fodstad, at the University of Oslo.

Table 3.1 - Cell lines used: Gender, age, tumor location of cell lines and the use of the cell line within the thesis. Use in thesis categorizes what the functional aspect of the cell line was during the thesis work. G denotes genetic analysis, I denotes that the cell line was planned for *in vivo* injection, V denotes that *in vitro* characterization was conducted.

Cell line	Gender	Age	Location of tumor	Use in thesis
H2	Female	65	Brain	G/I/V
H3	Female	63	Brain	G/I
H5	Male	57	Brain	G/I
H6	Female	28	Brain	G/I
H9	Female	44	Brain	G/I
H10	Female	62	Brain	G/I/V
Melmet 1	Female	36	Subcutaneous	G/I/V
Melmet 5	Male	56	Lymph node	G/I/V

3.2 Cell Culture Techniques, Cell Medium and PBS

All cell culture work was performed within a laminar air flow cabinet. Before use, the cabinet as well as items placed within the cabinet were sterilized with 70% ethanol. Filtered cap

EasYFLask™ of 25 cm^2, 75 cm^2 and 175 cm^2 size (Nunc) were used for cell culturing. All cells were kept in a standard tissue culture incubator at 37 °C with 100% humidity and 5% CO_2.

The cell lines were grown in Dulbecco's Modified Eagle Medium (DMEM, Sigma-Aldrich Inc., St. Louis, MO, USA) supplemented with 10% heat-inactivated fetal calf serum (Thermo Fisher Scientific, Waltham, MA, USA), 4 times the prescribed concentration of non-essential amino acids (BioWhittaker, Verviers, Belgium), 2% L-glutamine (BioWhittaker), penicillin (100 µL/mL, BioWhittaker) and streptomycin (100 µL/mL, BioWhittaker) (hereafter called ALT DMEM).

A phosphate-buffered saline (PBS) solution was prepared using 10x Dulbecco's phosphate-buffered saline (Sigma-Aldrich Inc.). Water used was de-ionized and filtrated (Milli-Q; Merck, Darmstadt, Germany) before being autoclaved. The PBS solution was then diluted to a working concentration of 1xPBS, using Milli-Q water.

3.3 Cell passaging

When cells achieved a 70-80% confluency, sub-culturing was done. 50% of the amount of complete ALT DMEM from the flask was transferred into a 15 mL or a 50 mL conical centrifugation tube (Thermo-Scientific, NY, USA), and the remaining medium in the flask was discarded. The culture flask was then washed with 1xPBS (the amount of PBS in mL corresponded to 0.05xarea of the flask), and the PBS was thereafter removed. The cells were detached using 0.25% Trypsin/EDTA (BioWhittaker) (the amount of Trypsin in mL corresponded to 0.02xarea of the flask). After the cell had detached (3-5 min), a volume equaling the Trypsin/EDTA solution + 1 mL of complete ALT DMEM was added to neutralize the enzymatic effect of Trypsin. To prevent cell clumping, the cell suspension was pipetted up and down several times, and then approximately 1/3 of the cell suspension was transferred into a new culture flask. The old cell medium was the added into the new culture flask, along with the same amount of fresh complete ALT DMEM.

For experimental use, cell cultures 10 passages after thawing from the N_2 tank was discarded to prevent potential, unknown genotypic and phenotypic changes within the cell population over time.

3.4 Cell Counting

Cells used for *in vitro* and *in vivo* experiments were counted using a Countess™ Automated Cell Counter (Invitrogen, Carlsbad, CA, USA), according to the manufacturer's instructions. Briefly, cell suspensions were made as described above. 10 uL of Trypan Blue (Invitrogen) was mixed with 10 uL of the cell suspension in a 0,5 mL Eppendorf tube (Eppendorf, Hamburg, Germany) and resuspended multiple times using a pipette, before aliquoting 10 uL of the sample to each side of a Countess® Cell Counting Chamber Slide. The slide was placed in the Countess™ Automated Cell Counter (Invitrogen), the focus was adjusted manually, and the cell numbers were then automatically counted.

3.5 Cell Thawing and Cryopreservation

Before fetching a vial of cell suspension from the liquid N_2 tank, a 25 mm^2 flask was prepared by adding 5 mL of complete ALT DMEM and placed in the incubator. A cell sample was then retrieved from the N_2 tank and thawed by placing it into a water bath holding 37 ^{0}C. After a brief thawing, the cell suspension was relocated into the flask, and put back into the incubator.

Cryopreservation of cells was done by freezing the cells in a liquid N_2 tank at -196 °C. A 70% confluent 225 cm^2 flask was washed, trypsinized and the proteolytic activity was neutralized by ALT DMEM as previously explained in cell passaging. Cells were then counted and centrifuged at 900 rpm for 4 min. The supernatant was removed, and the cell pellet was resuspended into a freezing solution consisting of 10 % calf serum (Thermo Fisher Scientific), 10 % DMSO (Sigma-Aldrich Inc.) and 80 % complete ALT DMEM. The cell solution was then aliquoted into 1 mL cryotubes (Thermo-Scientific Inc.) and frozen in -80 °C for at least 24 h before stored in liquid nitrogen.

3.5 *In Vivo* Cell Injections

All cell lines were grown in a 175 cm^2 culture flask to 70% cell confluency. Cells were washed once with 1xPBS and detached using 0.25% Trypsin/EDTA (BioWhittaker). The cell solution was then transferred to a 15 mL falcon centrifugation tube, centrifugated at 900 rpm for 4 min, and resuspended in 1xPBS. The cell concentration in the suspension was counted using a Countess™ Automated Cell Counter (Invitrogen; see procedure above), and the

concentration was adjusted to $5x10^6$ cells/mL using 1xPBS. Cells were then kept on ice until further use.

The mice were anesthetized with 3% isofluorane (in oxygen), and then maintained with 1.5% isofluorane (in oxygen). Fur in the thoracal area was shaved off before applying hair removal cream. The thoracal area was then cleaned with lukewarm water and dried.

The animal was placed on its backside on a heated table at the ultrasound machine. The feet were securely fastened by tape. An insulin needle containing $5x10^5$ tumor cells (in 100 uL PBS) was placed in a dedicated syringe holder close to the table, and the ultrasound probe was fastened onto another holder at the table. Ultrasound gel, prewarmed to 37 °C, was applied onto the thoracal area of the animal, and the ultrasound probe was lowered until the left cardiac ventricle was seen on the monitor of the ultrasound machine.

The needle was then inserted 6 mm into the chest, while tracing the needle on the monitor. The needles tip was guided into the heart until it could be clearly seen in the centre of the left cardiac ventricle. 0.02 mL of cardiac blood (which is bright red) was withdrawn into the syringe in order to verify that the left ventricle had been penetrated, the tumor cell solution was then injected over 20 sec. The needle was kept in position for another 5 sec to avoid back flow of cells, before the needle was retracted. Five mice were injected per cell line.
After cell injections, the animals were monitored daily, scanned by MRI (see below) and euthanized when significant morbidity symptoms were observed.

3.6 Apoptosis Assay

To further characterize the cell lines which will be used *in vivo* in later projects in the research group (H2, H10, Melmet 1 and Melmet 5, see Results section), apoptosis and necrosis was measured, using an apoptosis kit (AlexaFluor®488 Annexin v/dead cell apoptosis kit; Molecular Probes, Life Technologies).

Cells were seeded in a 6-well plate (Nunc) at a density of $3x10^5$ cells/well and incubated for 24 h. The culture medium was then removed, the cells were washed with PBS, trypsinized using 0.25% Trypsin/EDTA, collected and centrifuged as explained in chapter 3.3. The supernatant was discarded, and 100 µL of Av binding buffer containing 5 µL Av and 5 µL PI

(AlexaFluor®488 Annexin v/dead cell apoptosis kit; Molecular Probes, Life Technologies) was added to the cells before incubating for 15 min.

A positive control for apoptosis was made by adding hydrogen peroxide 30% (v/v) in H_20 at 10mM (Sigma, Steinheim, Germany) for 4 h, before collecting the cells for analysis. Three other controls were also prepared, to control for spillover in the flow detectors: One sample was stained with 5 µL Av, one sample was stained with 5 µL PI, and one sample was left unstained.

The cells were put in Falcon® 5 mL Round-Bottom tubes (Sarstedt, Nümbrecht, Germany), placed on ice and analyzed using an AccuriTM C6 flow cytometer (Accuri Cytometers Inc., Ann Arbor, MI, USA). Fluorescence in the FITC-Av-A and PE-A channels were gated to a two-parameter plot, and 20000 gated events were registered per sample. Each experiment was conducted three times and three technical replicates was made for each one. Data analysis was performed using FloJo software (Tree Star Inc., Ashland, OR, USA; Figure 3.1).

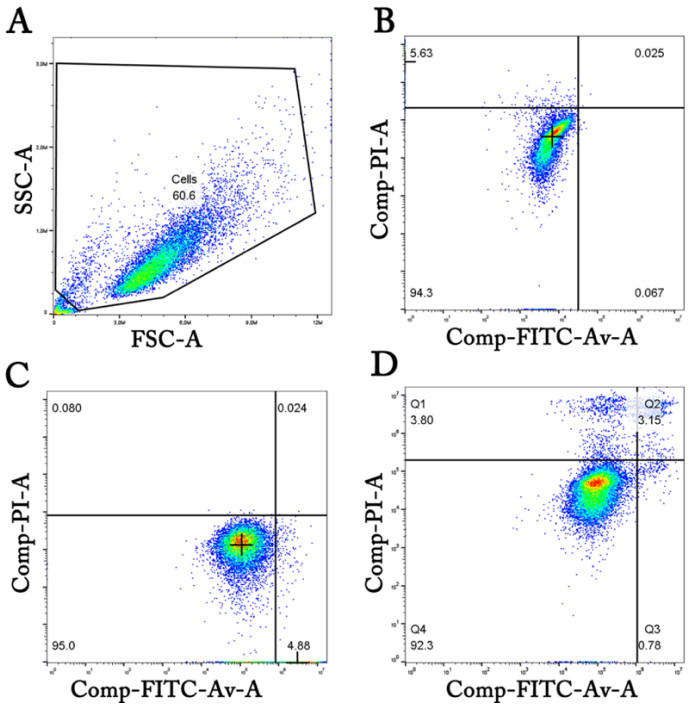

Figure 3.1 – Schematic representation of the apoptosis and necrosis analysis. A) A representative figure of events from an unstained sample by the flow cytometer. Single events, of which most are single cells, are primarily shown within the pentagon, also called a gate. FSC-A: Forward scatter area, SSC-A: Side scatter area. Figure B, C and D shows the cells and apoptotic bodies using gating parameters from Figure A. Figure B) displays a sample stained with PI. The quadrant gate is placed to border the events from a FITC-Av signal and divides the live and necrotic cell populations. A quadrant gate was also placed in Figure C), where the sample was stained with FITC-Av. The gate in Figure C borders the events from a PI signal and divides the live from early apoptotic cells. D) Figure displays a sample stained with both FITC-Av and PI. The quadrant gate was placed based on the Y-coordinates of the B) gate and X-coordinates of the C) gate. Comp-FITC-Av-A: Compensated FITC conjugated to Annexin V signal area. Comp-PI-A: Compensated PI signal area.

The gating for the apoptosis assay was done in accordance to Figure 3.1. To select for the cells and for removing cellular debris, the gating shown in Figure 3.1A was used. To analyze a sample stained with both PI and FITC-Av, the Y-coordinates from the quadrant gating in Figure 3.1B and the X-coordinates from Figure 3.1C were used to assemble the final gating construct in Figure 3.1D.

3.7 Cell Cycle Analysis

For cell cycle analysis, a cellular suspension of $2x10^5$ cells was harvested into a 15 mL tube and centrifuged at 900 rpm for 4 min. The supernatant was discarded, and 2 mL of 1xPBS was added, the cell pellet was resuspended, and again centrifuged at 900 rpm for 4 min. For fixation, 2 mL of -20 ^{0}C 70% ethanol diluted in distilled autoclaved water was added dropwise to the cellular pellet while pulse-vortexing the suspension. The samples were then stored in -20 ^{0}C for up to 2 weeks before being processed further. At the day of analysis, the samples were centrifuged and resuspended twice in 1 mL PBS. Then, the cell suspension was moved to Falcon® 5 mL Round-Bottom tubes. To remove all RNA present in the cell, 5 µL of 1 mg/mL Pancreatic bovine Ribonuclease A (RNase A; Sigma-Aldrich Inc., St. Louis, MO, USA) was added to all samples. For each cell line, three samples were stained with 5 uL PI (50 µg/mL in PBS) (Sigma-Aldrich Inc.), while one sample was left unstained. During analysis, 20000 events were registered per sample. The experiment was conducted three times with three technical replicates per experiment.

The data was analyzed using FloJo software (Tree Star Inc.) to determine the % of cells in the different phases of the cell cycle (Figure 3.2). The gating strategy is shown in Figure 3.2A-C. To find the G1/G0 phase cells, the lowest intensity cell population was determined, and a gaussian distribution curve was applied. The G2/M phase cells were determined by applying a gaussian distribution to the peak situating around twice the average intensity value of the gaussian distribution found for G0/G1. The S-phase was approximated by FloJo by fitting a polynomial function between G0/G1 and G2/M (Figure 3.2D).

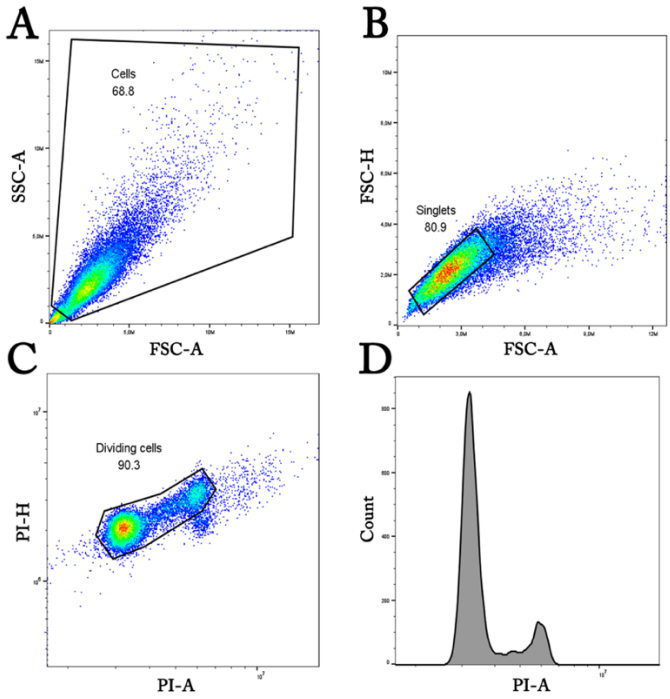

Figure 3.2 – Schematic representation of the cell cycle analysis. A) Representative figure of all events registered from one sample, by the flow cytometer. Cells are shown within the pentagon, also called a gate. FSC-A: Forward scatter signal area, SSC-A: Side scatter signal area. B) Figure showing the cells gated from A). Single cells are within the gate marked "singlets" in the figure. FSC-A: Forward scatter signal area, FSC-H: Forward scatter signal height. C) Figure showing the cells gated from B). The cells of interest are located within the gate shown. Cells outside this gate would be for instance doublets, triplets, etc. PI-A: Propidium iodide signal area, PI-H: Propidium iodide signal height. D. The results from Figure C, plotted in a one-parameter DNA histogram (PI-A versus number of cells).

3.8 *In Vitro* Cell Proliferation

The H2, H10, Melmet 1 and Melmet 5 cell lines were trypsinized, counted and centrifuged as previously explained in chapter 3.3. The supernatant was discarded, and the cell pellet was resuspended in 5 mL of DMEM ALT in a 15 mL conical centrifugation tube (Thermo Scientific, Nunc, NY, USA). The cell lines were seeded in a 96-well plate (Nunc) as shown in Figure 3.3, and complete ALT DMEM was added to obtain a volume of 200 µL per well. A gradient of cell concentrations was made over three columns in the 96-well plate for H2, H10, Melmet 1 and Melmet 5 to account for different cell confluences during analysis.

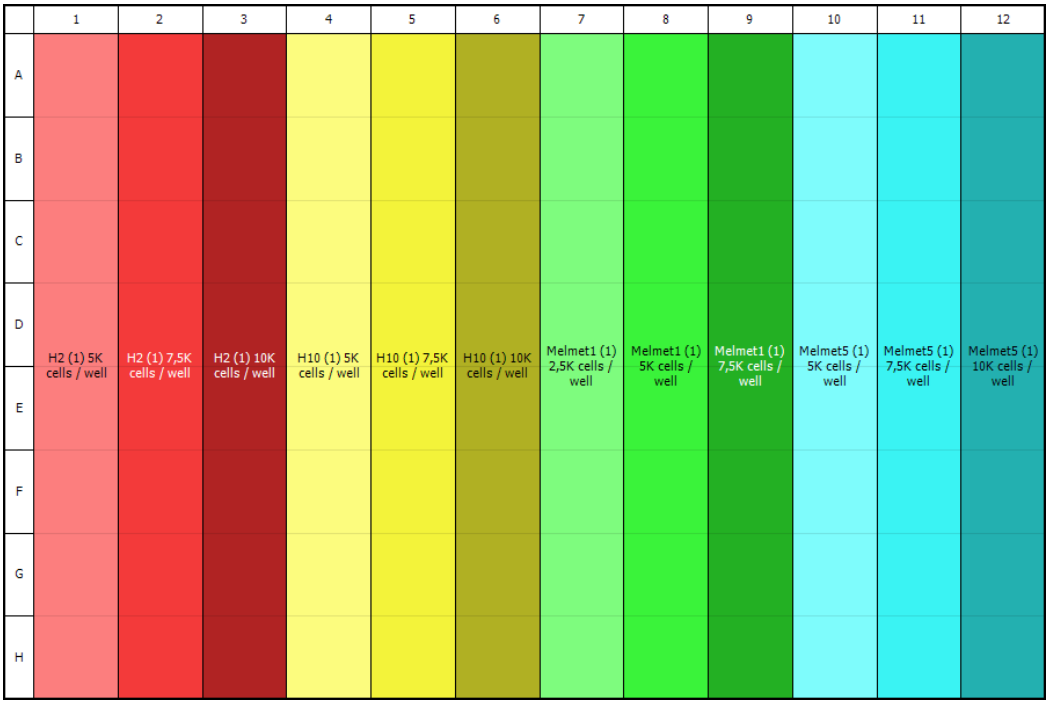

Figure 3.3 - Cell concentrations per well for each cell column in a 96-well plate. Cell concentrations for the H2 cell line: 1-3 column. H10 cell line: 4-6 column. Melmet 1 cell line: 7-9 column. Melmet 5 cell line: 10-12 column.

The increase in confluency over time (i.e. cell proliferation) was then measured using an IncuCyte Zoom live cell analyzer (Essen Bioscience, Ltd., Hertfordshire, UK). After placing the 96-well in the machine, the IncuCyte system obtained light microscopy pictures using the 10x objective, every 2 h for 4 days.

The data was analyzed using the IncuCyte software. First, representative pictures of cells at different time points were chosen for processing. Around 10-15 pictures were collected for each cell line. Melmet 1 was processed alone due to its cell morphology, while H2, H10 and Melmet 5 cells were processed together.

By manually changing the IncuCyte Zoom live cell analyzer software parameters to detect what a cell is, a digital mask was made over the presence of cells in the well. Based on the mask, the software assigned each picture a value relating to how many percentages each picture was covered by the cellular mask. This process was conducted for each picture taken by the machine. The percentage values for cell confluency over time was then exported and a graph plotting the cell confluency over time was made.

3.9 Mutational Analysis

Even though only 4 cell lines were eligible for *in vivo* experiments, mutational analysis was carried out for all cell lines for future experimental designs within the lab. H6 was not analyzed *in vitro* due to its slow proliferation rate.

To characterize the mutations which the cell lines harbor, DNA was first extracted. $4x10^6$ cells were harvested per cell line as described during Cell Passaging (chapter 3.3). For extracting and purification of DNA, DNeasy Blood & Tissue Kit (Qiagen, Venlo, Netherlands) was used. The extraction process was executed according to the manufacturer's description. A NanoDrop™ One^C Microvolume UV-Vis Spectrophotometer (Thermo Scientific) was used for DNA purity control. The purified dsDNA was then tested on a panel, checking for unique 360 mutations within known and suspected oncogenic and tumor suppressor proteins. Fragmentation of 2000 ng dsDNA was achieved using a Covaris M220 Focused-ultrasonicator™ (Covaris, Woburn, MA, USA). Library preparation was performed using the Agilent SureSelectXT reagent kit (Illumina, Santa Carla, CA, USA), with the individual samples of dsDNA investigated on a MiSeq instrument (Illumina, San Diego, CA, USA). To cover potential splice site mutations, the design had a margin of +/- 10 nucleotides at the exon-intron border. After the sequencing event, mutational data was extracted using baits targeting, as explained in Yates *et. al, 2015* [115]. The mutation data panel used is also presented in Yates *et. al, 2015* [115]. Single nucleotide variants (SNV) were detected within the dataset by the use of the CaVEMan algorithm, presented in Jones, D. *et al., 2016* [116]. The Pindel algorithm was used to detect small insertions and deletion events, as presented in Raine, K. *et al.*, 2015 [117].

3.10 Magnetic Resonance Imaging

Brain metastasis development in the nod/scid mice after intracardiac cancer cell injection was studied using a 7 Tesla small-animal MR scanner (Bruker PharmaScan; Bruker BioSpin MRI, Ettlingen, Germany) equipped with a 1-channel circular transmit coil and a 4-channel receive surface coil. Transversal, T1 weighted (T1w) images were taken before and after injection of Omniscan CA (GE Healthcare, Oslo, Norway) and images were produced with the following rapid acquisition with relaxation enhancement (RARE) sequence scan parameters: Field-of-

view (FOV) 2.0x2.0 cm, matrix size 256x256, 0.5 mm slice thickness, repetition time (TR) 1000, echo time (TE) 9, fractional anisotropy (FA) 90,0 and 4 averages. T2 weighted (T2w) transversal images were obtained with the following RARE sequence scan parameters: FOV 2.0x2.0 cm, matrix size 256x256, 0,5 mm slice thickness, TR 3200, TE 38, FA 90 and 4 averages.

Visualization of the total tumor numbers and the total tumor volume for each mouse was done by displaying the MR images in Osirix Lite v.10.0.0 freeware (Pixmeo SARL, Geneva, Switzerland). For tumor numbers and volumes, a single diameter of each tumor was measured with a region of interest (ROI) line. For each scan time, all the ROI lines for a single animal was exported into a .txt file and processed using a software program specially developed during this thesis work (Supplementary Figure 6.1). The output from the program was tumor numbers and total tumor volume for a single mouse. The program was executed in the open source freeware Spyder v.3.2.8 within the Anaconda Navigator (Anaconda, Inc., Austin, USA)

3.11 Histology

For each cell line injected *in vivo*, 3 animals were euthanized when they showed significant morbidities and their brains and other organs were extracted for hematoxylin and eosin (H&E) staining. Mouse brains were extracted and fixed in 4% paraformaldehyde (PFA). The mouse brains were kept in the PFA solution for 4 days before being dehydrated in escalating ethanol concentrations beginning at 70% to absolute ethanol overnight. The brains were then embedded in paraffin. Sectioning was done by the use of a microtome, with sections being cut in 4 µm slices directly into a water bath holding 40 ^{0}C. A glass slide was then used to pick up the sectioned tissue and this slide was placed in an incubator overnight at 37 ^{0}C. Sections were then deparaffinized by xylene in 2 rounds of 4 min. Tissues were rehydrated in absolute ethanol in 2 rounds for 2 min, then 96% ethanol for 2 min, then 70% ethanol for 2 min. Slides were then washed in distilled water. Hematoxylin (Harris Haematoxylin, CellPath, Newton, Great Britain) was added for 2 min before the sample was washed for 10 min in distilled water. Eosin was then added for 20 sec, before adding distilled water, then washing in 5 drops of 96% ethanol, then 5 drops of absolute ethanol. The sample was then cleared in 2 changes of xylene for 2 min each before the sample was mounted using xylene based mounting medium. The organs collected for histology are shown in Table 3.2.

Table 3.2 – Organs collected from each cohort. Organs collected were all embedded and paraffined, for then to be sectioned and stained. For H2, H9, H10, Melmet 1 and Melmet 5 injected mice 4,1,3,3,3 mice were collected organs from, respectively.

	Brain	Heart	Kidney	Leg	Liver	Lung	Lymph	Spleen
H2	x	x	x		x	x	x	x
H9	x						x	x
H10	x			x			x	
Melmet 1	x	x				x	x	x
Melmet 5	x	x					x	

3.12 Generation of New Tumor Cell Lines

Tumor specimens from mouse brain metastasis were collected to generate new tumor cell lines, in order to study if cell lines with higher brain-targeting abilities could be generate. After explanting mouse brains harboring tumors from H2, H10, Melmet 1 or Melmet 5 cell lines, the brains were first washed three times in 1xPBS, placed in petri dishes (Nunc) containing 3 mL of 1xPBS, and mechanically minced into small pieces using No. 11 stainless steel surgical blades (Swann-Moston, Sheffield, England). The brain-PBS suspensions were pipetted up and down for 10 sec before adding 5 mL of trypsin. After incubating for 5 min, the suspensions were pulse-vortexed for 15 seconds, the trypsin was neutralized with 6 mL of complete ALT DMEM, and the suspensions were then centrifuged at 900 rpm for 4 min. The cell/tissue pellets were resuspended in 10 mL of complete ALT DMEM before the cell suspensions were placed in either a T25 or T75 flask, depending on the amount of available tumor tissue, as well as the proliferative capacity of the original cell line.

4. Results

4.1 Metastatic potential

To visualize the metastatic progression of each cell line studied *in vivo*, MRI scanning was performed. Scanning was conducted in accordance to Table 4.1. The planned scanning was every two weeks, however, before mice were euthanized, they were scanned off schedule.

Table 4.1 – Scanning schedule of mice. Number of mice scanned in each week. If there were mice scanned on different days within a week, due to euthanization, all scans during that week is counted as within the same week. "✝" denotes that all mice were euthanized. "-" denotes that mice died shortly after injecting cancer cells. "*" denotes that cells were very slow-growing *in vitro*, thus we were not able to harvest sufficient number of cells for injection. "+" denotes that no mice were not scanned that week.

	Week 2	Week 4	Week 5	Week 6	Week 7	Week 8	Week 9	Week 10	Week 11
H2	5	5	+	5	3	2	✝	✝	✝
H3	-	-	-	-	-	-	-	-	-
H5	1	1	+	1	+	1	+	1	✝
H6	*	*	*	*	*	*	*	*	*
H9	1	✝	✝	✝	✝	✝	✝	✝	✝
H10	5	5	+	5	+	3	3	✝	✝
Melmet 1	5	5	+	5	1	4	✝	✝	✝
Melmet 5	5	5	5	✝	✝	✝	✝	✝	✝

In accordance to Table 4.1, animals were euthanized when showing morbidity symptoms. The abdominal cavity was opened up and inspected for extracranial metastases. Table 3.2 shows which organs were studied by histology, while Table 4.2 demonstrates the distribution of tumors within different organs of the mice, confirmed by Hematoxylin staining. The organs confirmed by H&E staining to contain tumors were the brain, heart, leg and lymph. The cell lines H2, H10, Melmet 1 and Melmet 5 successfully metastasized to the brain in all five mice of each cohort and were thus the cell lines chosen to be characterized further by *in vitro* studies.

Table 4.2 - Tumor distribution in organs. Location and number of tumor sites seen in the mice cohorts. Brain tumors were observed using MRI, while extracranial tumors were detected post mortem by the use of sectioning and H&E staining of paraffin-embedded organs. The parenthesis within brain tumor number indicates the first week tumors could be detected by MR imaging. Tumors were observed in most of the mice for the Melmet 5 mice, however, they were not confirmed by sectioning, and therefore not included in the table. "o" denotes that there were no tumors registered. "-" denotes that mice died shortly after injecting cancer cells. "*" denotes that cells were very slow-growing *in vitro*, thus we were not able to harvest sufficient number of cells for injection.

	Brain	Heart	Kidney	Leg	Liver	Lung	Lymph	Spleen
H2	5/5 (w2)	o	2/5	o	o	o	1/5	o
H3	-	-	-	-	-	-	-	-
H5	o	o	o	o	o	o	o	o
H6	*	*	*	*	*	*	*	*
H9	o	o	o	o	o	o	o	o
H10	5/5 (w4)	o	o	1/5	o	o	1/5	o
Melmet 1	5/5 (w4)	o	o	o	o	o	3/5	o
Melmet 5	5/5 (w4)	1/5	o	o	o	o	o	o

The average brain tumor numbers for each cell line is shown in Table 4.3, and the average total brain tumor volumes are shown in Table 4.4. Mice injected with H2 cells had the lowest tumor numbers, albeit not the lowest tumor volumes. The largest number of tumors was found in the mice cohort injected with the H10 cell line, which seemed to have an abundant number of tumors with lesser volumes, compared to the other cohorts. The number of tumors observed in the Melmet 1 injected mice were considerably less than for the H10 injected mice but showed the largest total average volume at 93.1 mm^3. The Melmet 5 injected mice were all euthanized in week 5, however the average amount of tumors and the average total volumes were low, compared to the others. H3 injected mice were euthanized right after intracardiac injection, due to adverse reactions after the injection procedure. Of the five H9 mice, four were euthanized due to the same reasoning as H3 injected mice. The last surviving H9 mouse produced no tumors. In the H5 mouse cohort, four died immediately after injections, and the remaining mouse did not develop brain tumors. The H6 cell line grew too slow in vitro, therefore there were not enough cells to inject. Based on these results, further *in vitro* studies were performed with the cell lines H2, H10, Melmet 1 and Melmet 5.

Table 4.3 - Average numbers of brain metastases in mice for the different cell lines. Tumor numbers were quantified by interpreting MR images. 5 mice were imaged per week, except: 4 mice in week 7 and 1 mice in week 8 for H2, 3 mice in week 9 for H10, 4 mice in week 8 for Melmet 1 and 3 mice in week 5 for Melmet 5. "†" denotes that all the mice had been euthanized. "o" denotes that there were no tumors detected. "-" denotes that mice died shortly after injecting cancer cells. "*" denotes that cells took too long to grow *in vitro* to be injected. NA indicates that MRI was not done that week.

	Week 2	Week 4	Week 5	Week 6	Week 7	Week 8	Week 9	Week 10
H2	1,00	1,00	NA	1,60	3,25	2,00	†	†
H3	-	-	-	-	-	-	-	-
H5	o	o	o	o	o	o	o	o
H6	*	*	*	*	*	*	*	*
H9	o	o	o	o	o	o	o	o
H10	o	1,00	NA	14,80	NA	60,33	92,00	†
Melmet 1	o	1,00	NA	12,80	NA	35,20	†	†
Melmet 5	o	7,80	14,80	†	†	†	†	†

Table 4.4 – Average total volumes of brain metastases in mice for the different cell lines. 5 mice were imaged per week, except: 4 mice in week 7 and 1 mice in week 8 for H2, 3 mice in week 9 for H10, 4 mice in week 9 for Melmet 1 and 3 mice in week 5 for Melmet 5. "†" denotes that all the mice had been euthanized. "o" denotes that there were no tumors detected. "-" denotes that mice died shortly after injecting cancer cells. "*" denotes that cells took too long to grow *in vitro* to be injected. NA indicates that MRI was not done that week. The numbers displayed are in mm^3.

	Week 2	Week 4	Week 5	Week 6	Week 7	Week 8	Week 9	Week 10
H2	6,21	7,35	NA	17,08	52,53	90,00	†	†
H3	-	-	-	-	-	-	-	-
H5	o	o	o	o	o	o	o	o
H6	*	*	*	*	*	*	*	*
H9	o	o	o	o	o	o	o	o
H10	o	0,05	NA	1,97	NA	20,37	34,08	†
Melmet 1	o	0,03	NA	5,78	NA	93,05	†	†
Melmet 5	o	1,32	4,32	†	†	†	†	†

4.2 MRI and Histology of Cell Lines that Developed Metastases in the Brain

Representative MR images of one mouse brain from each cohort was chosen for demonstating tumor growth and expansion over time. In Figure 4.1, the distribution and progression of a brain metastatic tumor located caudally can be seen in a mouse injected with the H2 cell line. The same placements and tumor expansions were also found in the remaining 4 mouse brains in the cohort.

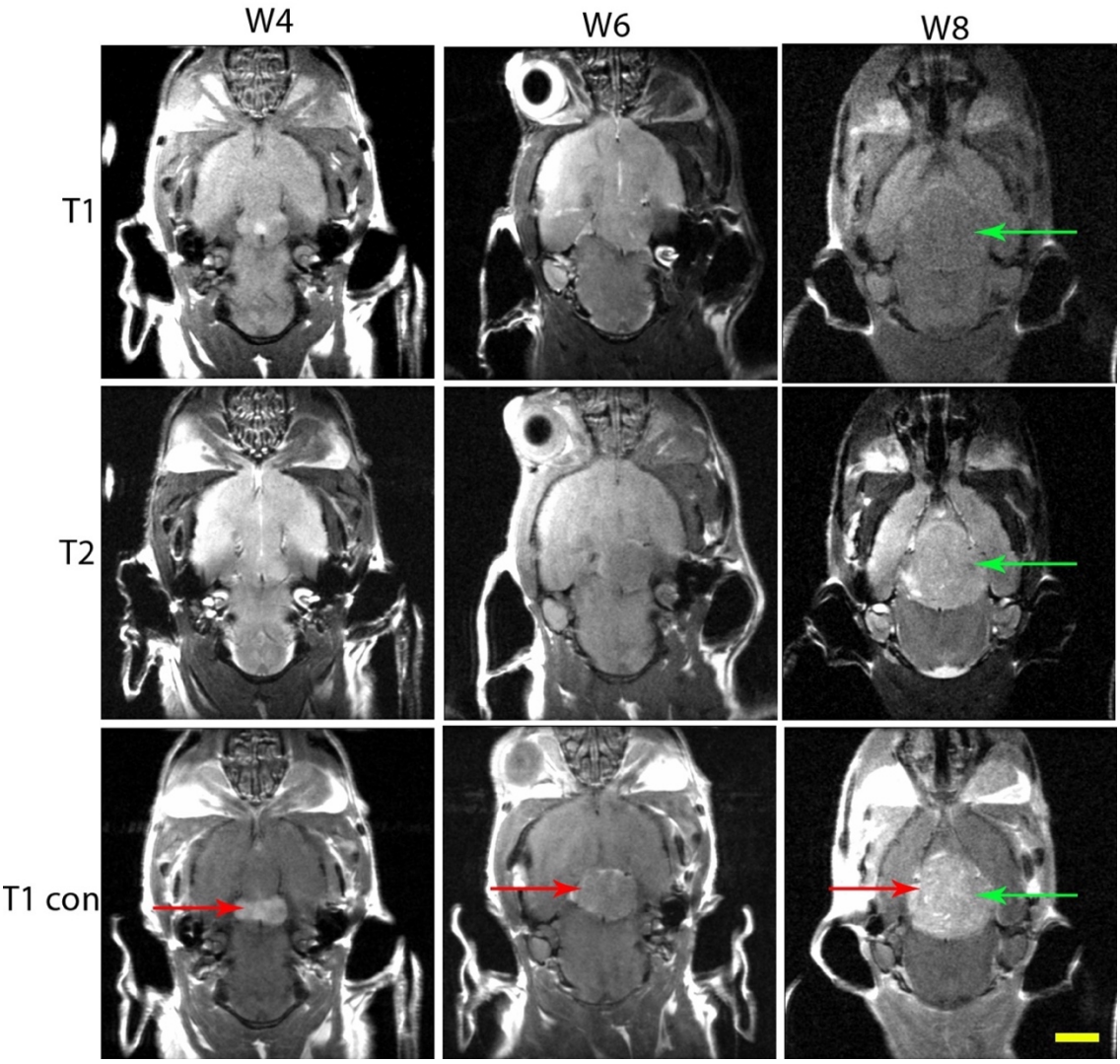

Figure 4.1 – MR images obtained of a mouse brain (mouse M3, see also Figure 4.2 below) at different time points after injection of the H2 cell line. In these images, expansion of a caudally located brain metastasis can clearly be seen, especially on T1 weighted images after contrast injection (bottom row, red arrows). Green arrows indicate the tumor visibility difference between the different imaging relaxation times. T1 = T1 weighted MR image, T2 = T2 weighted MR image, T1 con = T1 weighted MR image after contrast injection. W4 = week 4, W6 = week 6 and W8 = week 8 after tumor cell injections. Scale bar = 2,5 mm

The numbers and volumes of brain metastases in mice harboring H2 tumors were then quantified, as shown in Figure 4.2. For 3 of the mice (M1, M2 and M3). 1 or 2 tumors were detected at week 7, with total tumor volumes between 70-90 mm^3. For the 2 remaining mice (M4 and M5), a larger number of tumors (3 or 5) were detected at week 7, with total tumor volumes of around 20 mm^3. From this data, there appeared to be a negative correlation between tumor numbers and total tumor volumes.

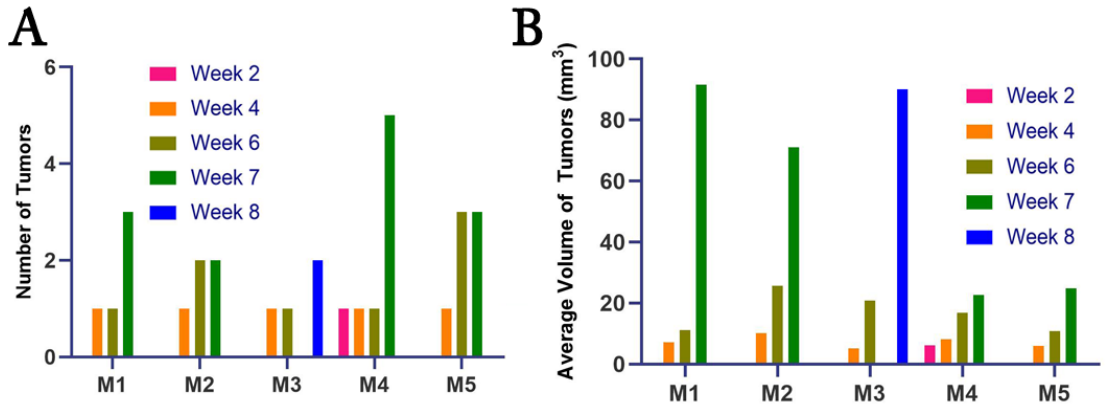

Figure 4.2 – Number and volume of brain tumors for each individual mouse injected with the H2 cell line. Showing five mice over eight weeks (A) Number of brain tumors of the H2 injected cohort. (B) Total average volume of brain tumors of the H2 injected cohort.

Figure 4.3 displays light microscopy images of an of a hematoxylin stained slide of a mouse brain with an H2 tumor. Typically, the large tumors were situated near the hypothalamus, midbrain and pons (Figure 3A). A circumscribed border between the tumors and the normal brain could be seen (Figure 3B).

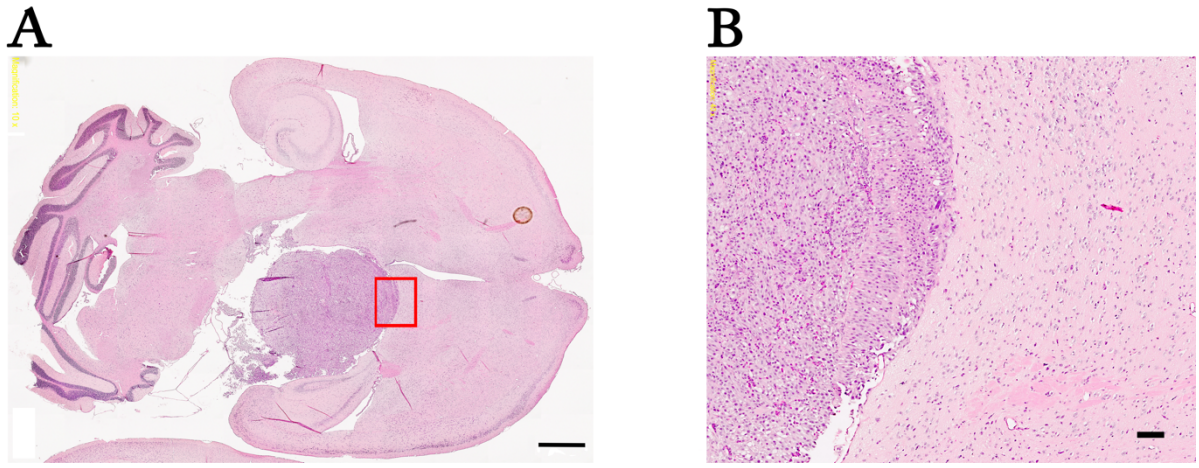

Figure 4.3 - H2 injected mouse brain slice (mouse M3, see also Figure 4.2 above) stained with Hematoxylin. The images are color corrected after light microscopy. (A) is a whole brain sliced in a transversal direction scanned at 10x. Scale bar = 1 mm. The red square present in (A) displays where (B) is imaged from. (B) is a transversal light microscopy image obtained with a 20x objective. Scale bar = 100 um.

In Figure 4.4, the distribution and progression of brain metastatic tumors can be seen on MR images, in a mouse injected with the H10 cell line. Multiple smaller tumors appearing in the cerebral cortex were found.

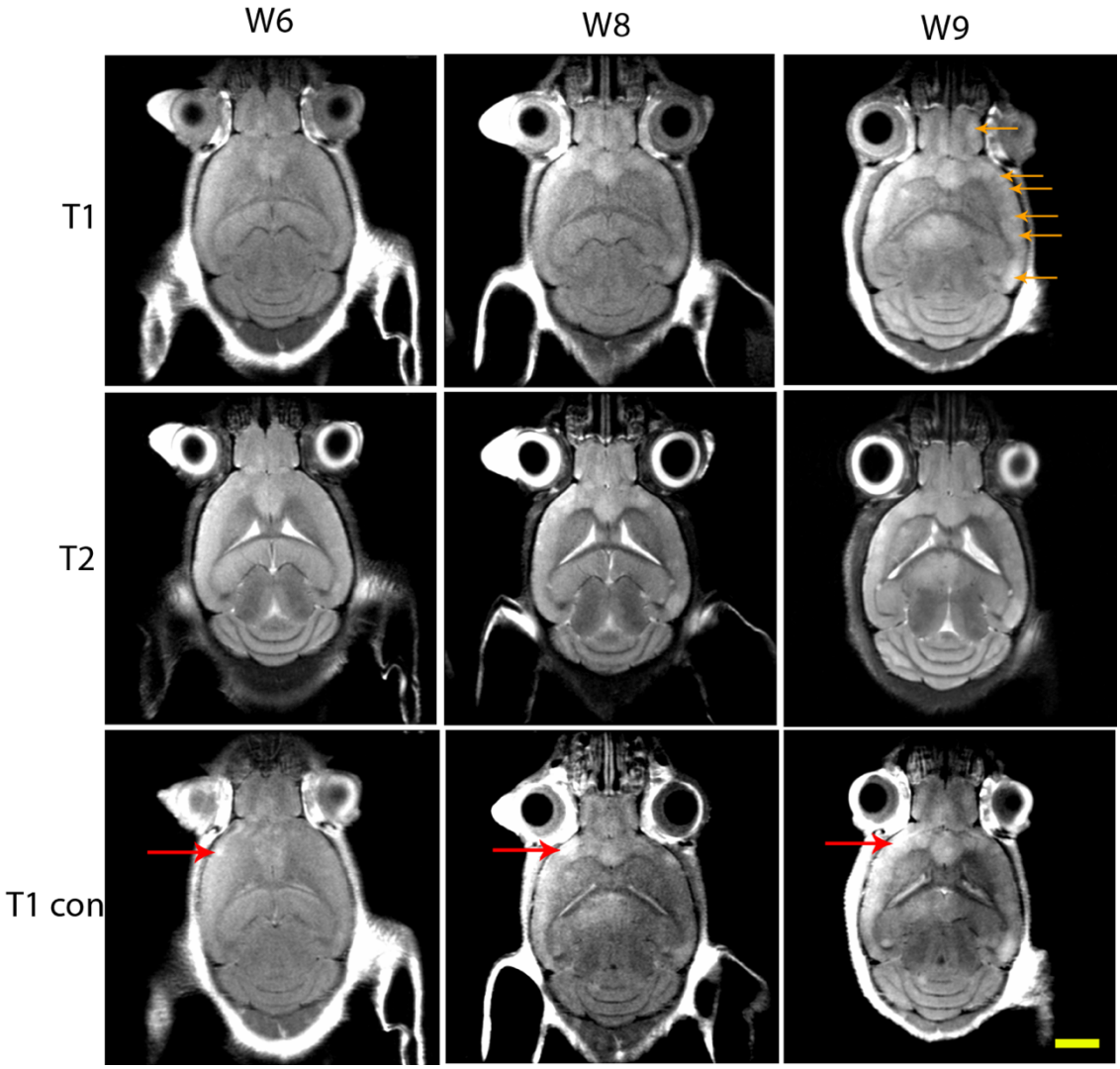

Figure 4.4 – MR images obtained of a mouse brain (mouse M2, see also Figure 4.5 below) at different time points after injection of the H10 cell line. In these images, expansion of a brain metastasis in the left frontal cortex can clearly be seen, especially on T1 weighted images after contrast injection (bottom row, red arrows). Orange arrows show some of the multiple small tumors that grow characteristically for the H10 cell line. T1 = T1 weighted MR image, T2 = T2 weighted MR image, T1 con = T1 weighted MR image after contrast injection. W6 = week 6, W8 = week 8 and W9 = week 9 after tumor cell injections. Scale bar = 2,5 mm

The numbers and volume of brain metastases in mice harboring H10 tumors were then quantified, as shown in Figure 4.5. Between 80 and 120 individual small tumors could be detected at week 9 for 3 of the mice (M2, M3 and M5). The total tumor volumes varied between 25 mm^3 and 50 mm^3. Small tumors were detected for M1 and M4 at week 6, however, the tumor numbers and volumes were minimal.

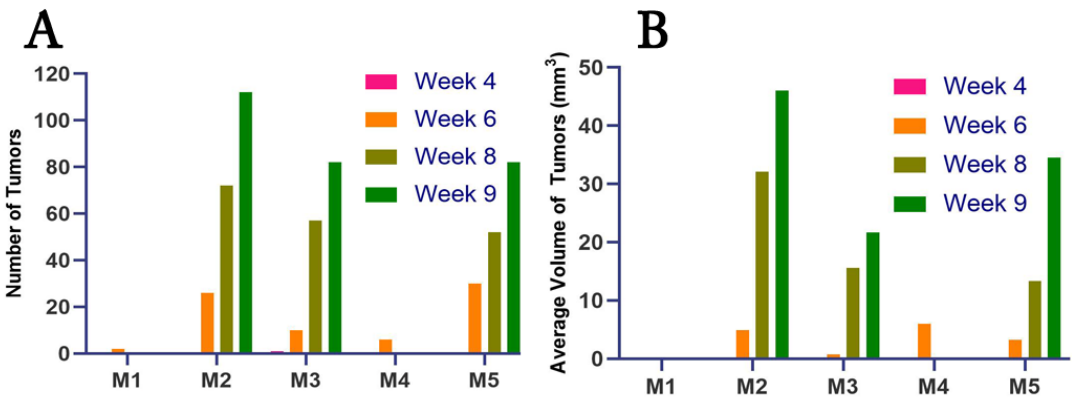

Figure 4.5 – Numbers and volumes of brain tumors for each individual mouse injected with the H10 cell line. (A) Number of brain tumors of the H10 injected cohort. (B) Total average volume of brain tumors of the H10 injected cohort.

Figure 4.6 displays light microscopy images from a hematoxylin stained slide of a mouse brain with H10 tumors. A diffuse tumor cell infiltration was seen within the whole brain parenchyma (Figure 4.6A), and tumor cell growth seemed to be aligned in clusters around the brain capillaries (Figures 4.6B and 4.6C). As seen by Supplementary Figure 6.1, these tumors are not distinctly vascularized.

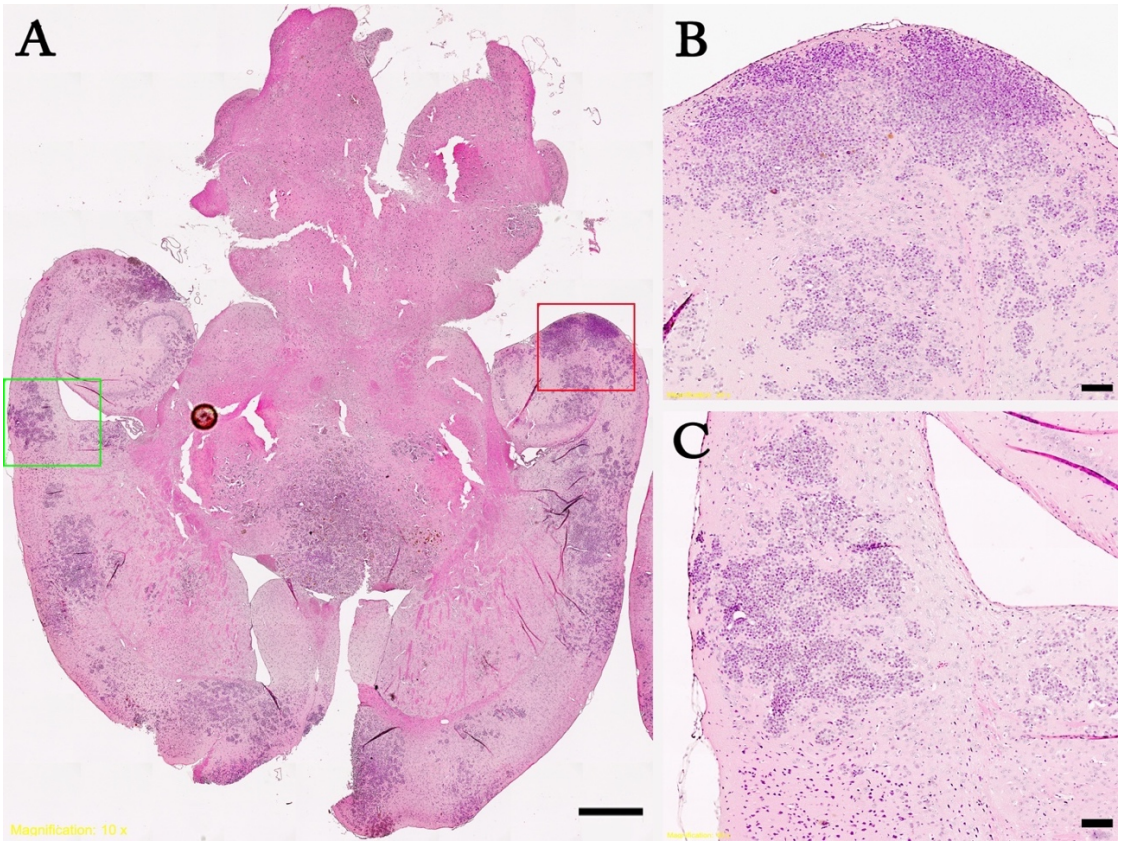

Figure 4.6 – H10 injected mouse brain slice (mouse M5, see also Figure 4.5 above) stained with hematoxylin. The light microscopy images are color corrected after imaging. (A) is a whole brain sliced in a transversal direction scanned at 10x. Scale bar = 1 mm. The red square in (A) displays where (B) is imaged from and the green where (C) is imaged from. (B) and (C) are both transversal slices scanned at 20x and 40x, respectively. Scale bars = 100 um.

In Figure 4.7, the distribution and progression of brain metastatic tumors can be seen on MR images, in a mouse injected with the Melmet 1 cell line. A large, centrally located tumor was detected at week 8 on T2- and T1-weighted images after contrast injection. Also, expansion of a brain metastasis in the left olfactory bulb could clearly be seen on T2 weighted images (middle row, red arrows), which was invisible on T1 weighted MR images after contrast injection, until week 8. At week 8, a tumor in the right frontal lobe was hardly visible on T1 weighted images, but could be clearly detected after contrast injection, or on T2 weighted images (green arrows).

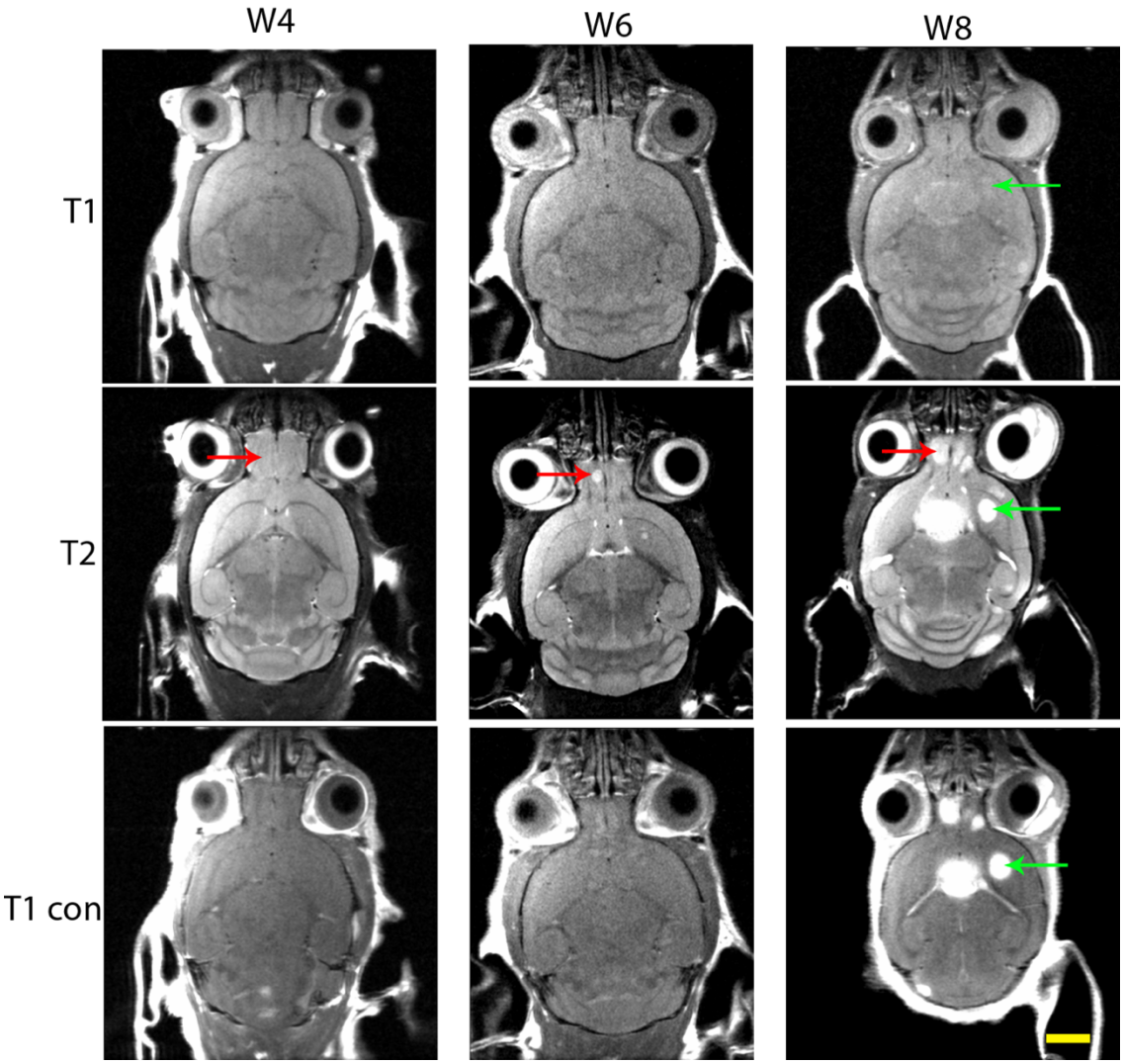

Figure 4.7 – MR images obtained of a mouse brain (mouse M3, see also Figure 4.8 below) at different time points after injection of the Melmet 1 cell line. An expansion of a central subcortically located brain metastasis is seen at week 8. Further, expansion of a lesion in the olfactory bulb is seen over time (red arrows). A tumor hardly visible on T1 weighted images was clearly seen on T2- and T1-weighted images after contrast injection (green arrows). T1 = T1 weighted MR image, T2 = T2 weighted MR image, T1 con = T1 weighted MR image after contrast injection. W4 = week 4, W6 = week 6 and W8 = week 8 after tumor cell injections. Scale bar = 2,5 mm

The numbers and volumes of brain metastases in mice harboring Melmet 1 tumors were then quantified, as shown in Figure 4.8. At week 8, between 25 and 60 tumors was detected in the individual mouse brain (Figure 4.8A). At the same time point, there was a wide range in total tumor volumes, spanning from around 5 mm^3 to 170 mm^3 (Figure 4.8B).

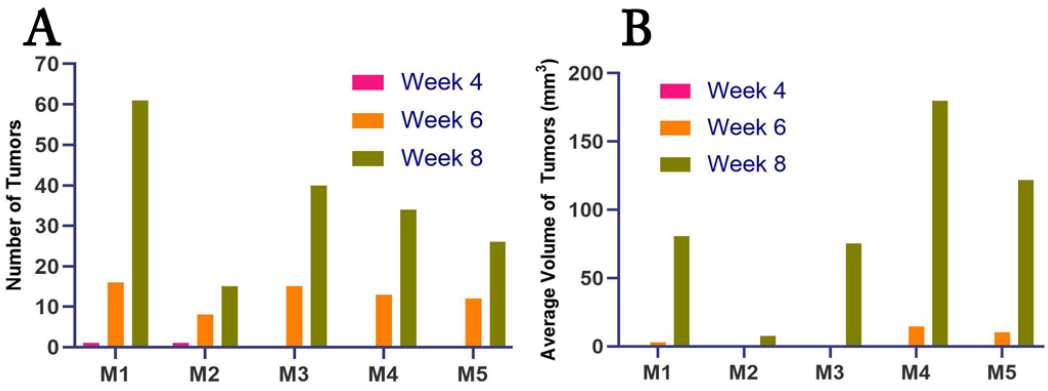

Figure 4.8 – Number and volume of brain tumors for each individual mouse injected with the Melmet 1 cell line. Showing five mice over eight weeks (A) Number of brain tumors of the Melmet 1 injected cohort. (B) Total average volume of brain tumors of the Melmet 1 injected cohort.

The histology of Melmet 1 tumors (Figure 4.9) showed a combination of larger, circumscribed tumor masses (Figures 4.9A and 4.9B), and areas of tumor clusters proliferating around brain capillaries (Figure 4.9C). As seen by Supplementary Figure 6.2, these tumors were highly vascularized.

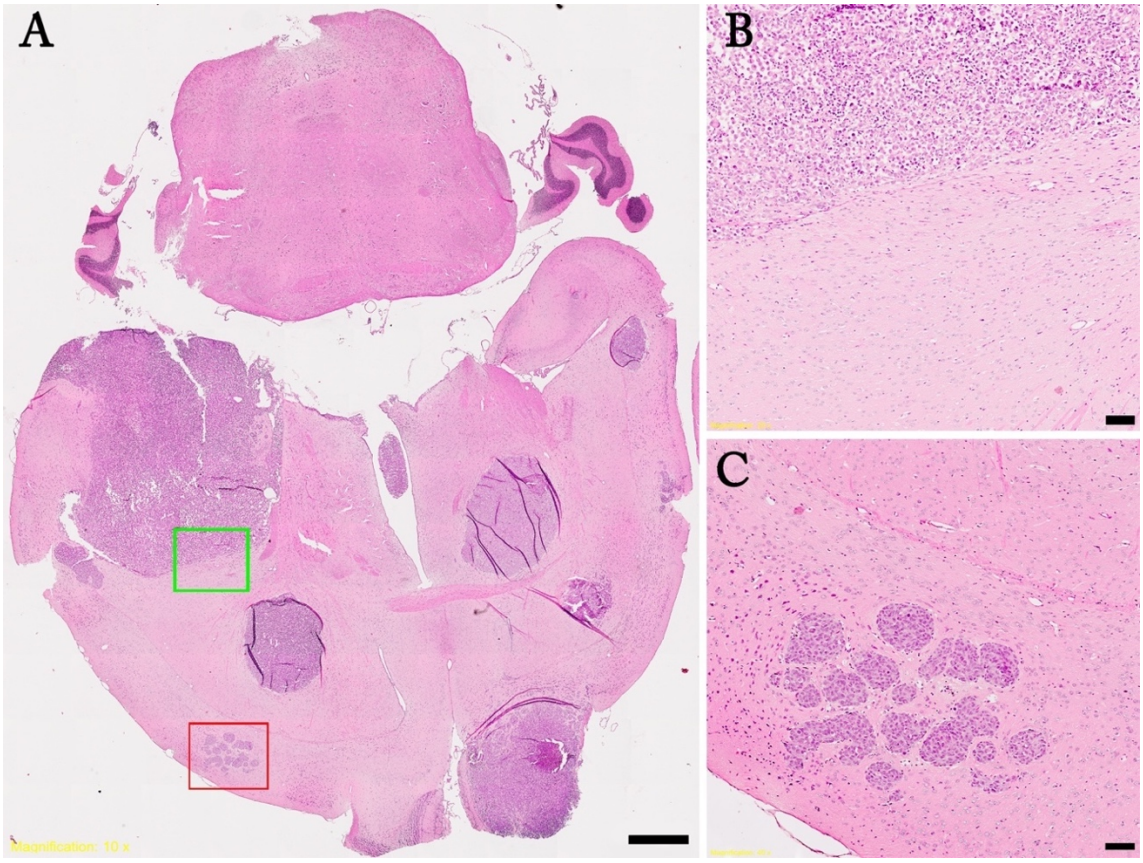

Figure 4.9 – Melmet 1 injected mouse brain slice (mouse M4, see also Figure 4.8 above) stained with hematoxylin. The light microscopy images are color corrected after imaging. (A) is a whole brain sliced in a transversal direction scanned at 10x. Scale bar = 1 mm. The green square in (A) displays where (B) is imaged from and the red where (C) is imaged from. (B) and (C) are both transversal slices scanned at 20x and 40x, respectively. Scale bar = 100 um.

In Figure 4.10, the distribution and progression of brain metastatic tumors can be seen on MR images, in a mouse injected with the Melmet 5 cell line. In general, very few tumors were detected, even after 5 weeks, when the animals were sacrificed. Again, longitudinal monitoring of tumors (red arrows) and the importance of detecting tumors by performing T1 weighted MRI after contrast enhancement (green arrows) were demonstrated.

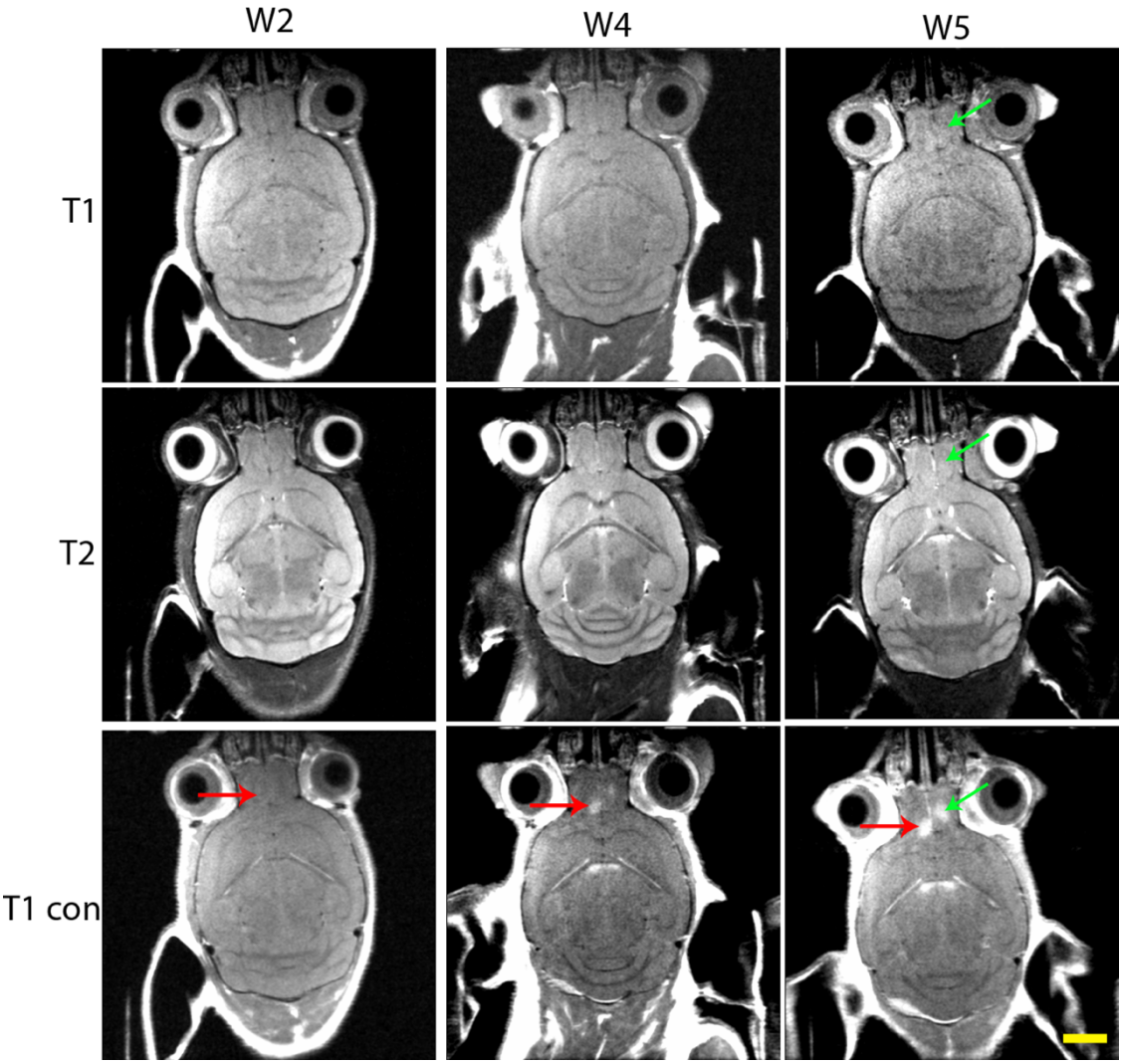

Figure 4.10 MR images obtained of a mouse brain (mouse M2, see also Figure 4.11 below) at different time points after injection of the Melmet 5 cell line. An expansion of a lesion in the olfactory bulb is seen over time (red arrows). Also, a tumor not visible on T1- or T2 weighted images was clearly seen T1-weighted images after contrast injection (green arrows). T1 = T1 weighted MR image, T2 = T2 weighted MR image, T1 con = T1 weighted MR image after contrast injection. W2 = week 2, W4 = week 4 and W5 = week 5 after tumor cell injections. Scale bar = 2,5 mm

The numbers and volumes of brain metastases in mice harboring Melmet 1 tumors were then quantified, as shown in Figure 4.11. At week 5, between 5 and 25 tumors were detected in the individual mouse brain (Figure 4.11A). At the same time point, there was a relatively homogenous range in total tumor volumes, from around 3 mm^3 to 11 mm^3 (Figure 4.12B).

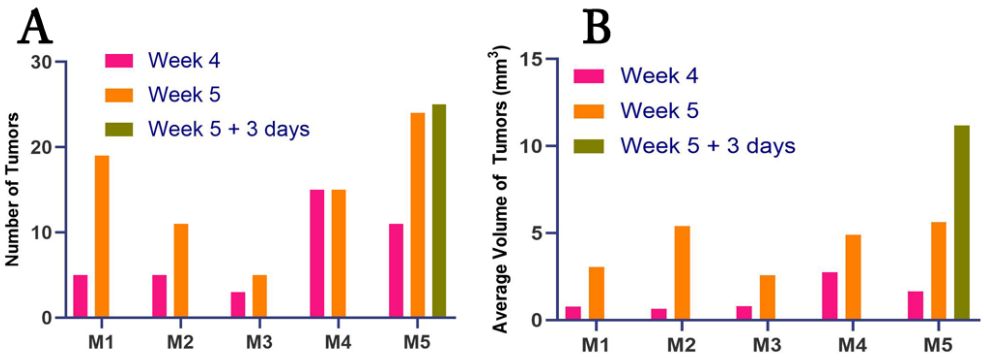

Figure 4.11 – Numbers and volumes of brain tumors for each individual mouse injected with the Melmet 5 cell line. Tumor burden is shown in five mice over five weeks. (A) Number of brain tumors of the Melmet 5 injected cohort. (B) Total average volume of brain tumors of the Melmet 5 injected cohort.

The hematoxylin stained histological section slide images presented in Figure 4.12 shows a Melmet 5 injected mouse brain sliced in a sagittal orientation. With a characteristic low brain tumor load and volume, the tumors displayed in Figure 4.12 are situated in the olfactory bulb and one around the caudate putamen, basal forebrain and the ventral striatum. The tumors are also circumscribed, with the olfactory tumors being more diffuse than the ones within the main part of the brain.

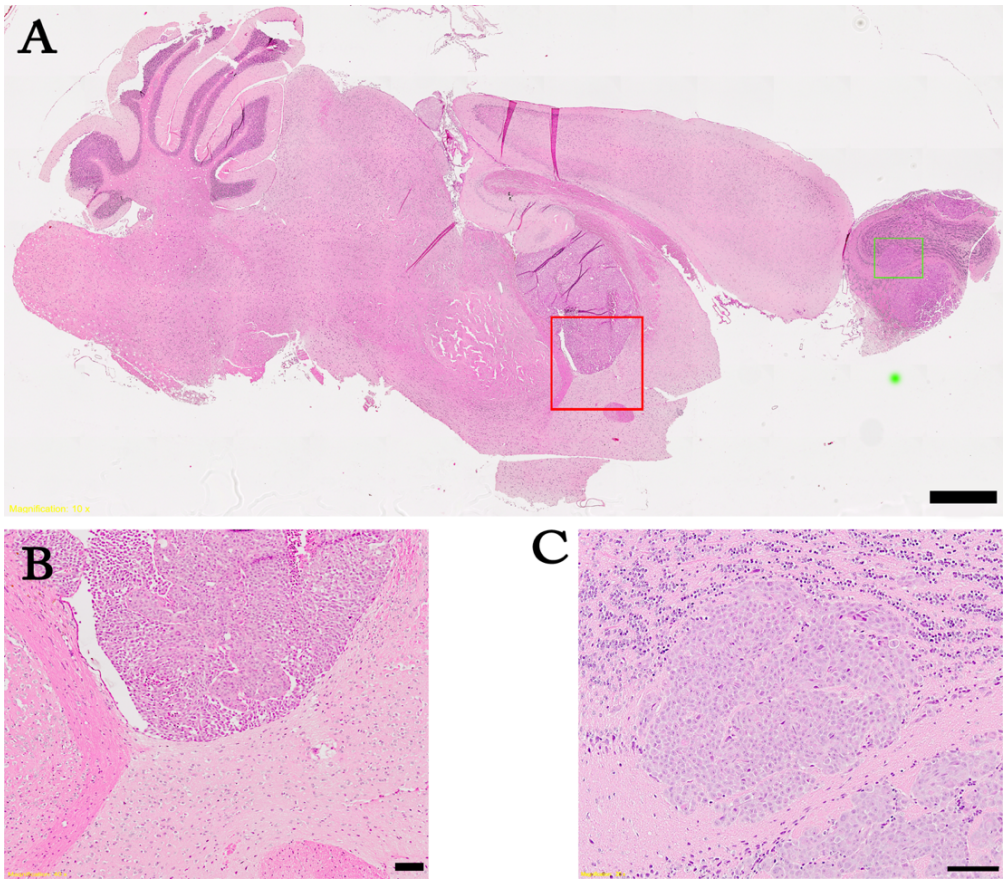

Figure 4.12 – Melmet 5 injected mouse brain (mouse M3, see also Figure 4.11 above) slice stained with hematoxylin. The light microscopy images are color corrected after imaging. (A) is a whole brain sliced in a sagittal direction scanned at 10x. Scale bar = 1 mm. The red square in (A) displays where (B) is imaged from and the green where (C) is imaged from. (B) and (C) are both sagittal slices scanned at 20x and 40x, respectively. Scale bars = 100 um.

4.3 Anatomical Distribution of Brain Metastases

Figure 4.13 shows the anatomical tumor distribution in mouse brains of the H2, H10 and Melmet 1 tumors, 6 weeks after tumor cell injections, and the Melmet 5 tumors, 5 weeks after tumor cell injections. Indicators were places in the middle of each tumor, if a tumor spanned over multiple slices, the middle slice was chosen as the tumor location. The H2 tumors were mainly situated within the lower middle part of the brain in slices 2, 4 and 5. However, also two tumors were found in the upper cortex (slices 11 and 12). H10 tumors were mainly distributed in the middle cerebral cortex, as evident by slices 4-10. The Melmet 1 tumor distribution seemed to be quite randomly scattered throughout the brain, with no clear propensity towards a certain area. Melmet 5 tumors however, seems to be found mainly in the olfactory bulb, as seen in slices 5, 6 and 7, with some tumor growth in the upper layers of the cerebral cortex, as seen in slices 9, 10, 11 and 12.

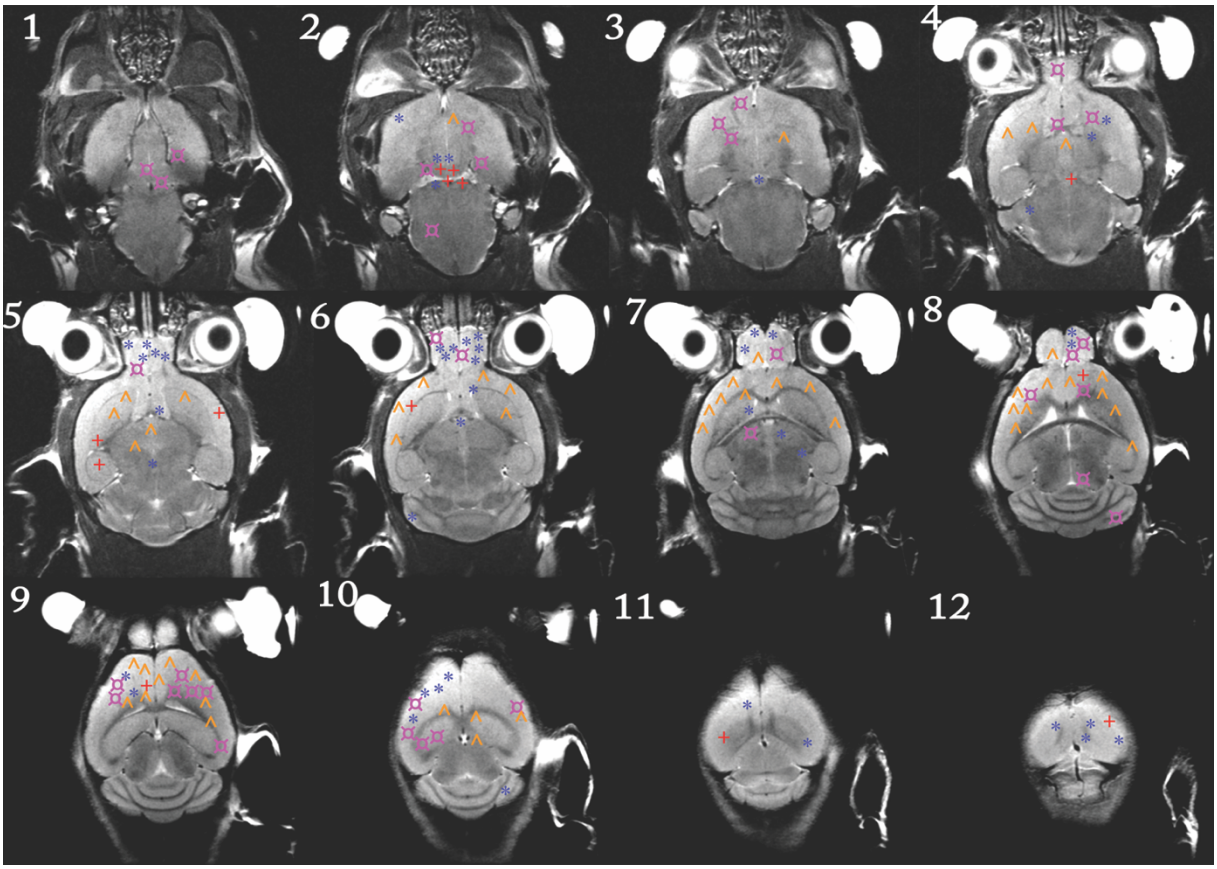

Figure 4.13 - Tumor distribution within the mouse brain. The central position of each registered tumor was mapped onto MR images taken of a control mouse brain. Red plus signs = H2, orange circumflexes = H10, pink circles = Melmet 1 and blue stars = Melmet 5. Numbering 1-12 accounts for one slice image of transversal plane MR, starting at the caudal parts of the brain at 1. The tumor distribution figure is based on tumor growth of all five mice within the cohort at week 6 for H2, H10 and Melmet 1 with Melmet 5 mapping being based on week 5. The slice thickness of the MR images is 0,5mm.

4.5 Mutational Analysis

Table 4.6 shows the 5 most common mutations for melanoma, as reported by the catalogue of somatic mutations in cancer (COSMIC) database and the distribution of these mutations within the cell lines characterized [118]. Mutations within the cell lines were confirmed to be tumor derived by filtering the data using genetic results from corresponding blood samples, with the exception of Melmet 1 and Melmet 5, where it is unknown if the mutations are germline derived or not (no corresponding blood samples available).

The most common mutation, BRAFV600E, was found in 7 of the 8 cell lines investigated, as seen in Table 4.6. For the last cell line (H3), a BRAF L577F mutation was detected. It is currently not known if this mutation is pathogenic or not. CDKN2A mutations were found in the cell lines H9 with a N421 mutation and the H10 harboring a R80X mutation. The H3 cell line harbors an NRAS Q61H mutation. A PTEN T131I mutation was detected in the H9 cell line. Also, TP53 mutations were found in H3 with R248Q being mutated, H9 with Y327X being mutated and Melmet 5 with G134E being mutated, where the G134E mutation is unknown to be pathogenic or not.

For a complete overview of all detected mutations within the selected cell lines, see Supplementary Figure 6.2.

Table 4.6 – Mutational analysis of H2, H3, H5, H9, H10, Melmet 1, Melmet 5 cell lines. The selected cell lines were tested on a panel of 360 mutations. Shown in the table are the most prevalent genes mutated found for melanoma, with the corresponding genomic DNA change. Genomic DNA changes are marked as N/A if it was not provided by the software. AA changes are marked orange if they are known to be pathogenic drivers, while left unmarked if unknown. Cosmic ID is provided for known pathogenic drivers. Melmet 1 and Melmet 5 mutations are unknown to be germline or somatic mutations.

Gene	g.DNA mutation	AA Change	Cosmic ID	H2	H3	H5	H9	H10	Melmet1	Melmet5
BRAF	140453999 G>A	L577F	-		x					
	140453136 A>T	V600E	COSM476	x		x	x	x	x	x
CDKN2A	21974702 T>A	N42I	COSM4428602				x			
	21971120 G>A	R80X	COSM12475					x		
NRAS	115256528 T>A	Q61H	COSM586		x					
PTEN	89692908 C>T	T131I	COSM5104				x			
TP53	7577538 C>T	R248Q	COSM10662		x					
	7576865 A>T	Y327X	COSM4398579				x			
	N/A	G134E	-							x

4.6 *In Vitro* Cell Proliferation

Based on the *in vivo* results, the H2, H10, Melmet 1 and Melmet 5 cell lines were studied further *in vitro,* for a more complete characterization. A confluency assay for proliferation was done, to assess the proliferative capabilities of the cell lines in culture. The confluency coverage over time is shown in Figure 4.14. Melmet 1 cells were growing to the highest confluency, indicating the highest proliferative capacity. A plateau of the logarithmic growth curve was reached after around 70 h. H2 followed Melmet 1 in terms of confluency coverage. However, by 90 h, the logarithmic growth plateau of H2 was not reached. H10 and Melmet 5 were the slowest growing cell lines, with Melmet 5 reaching the highest confluency of the two. Neither H10 nor Melmet 5 reached the logarithmic growth plateau within the 90 h displayed. A one-way ANOVA showed statistically significant differences among the cell line proliferation groups when comparing the cell line proliferation at 72h and 90h, respectively with an α value of 0,05. While a *post hoc* t-test with Bonferroni correction showed significant mean differences between all cell lines at both 72h and 90h with a *p* value of < 0,0125.

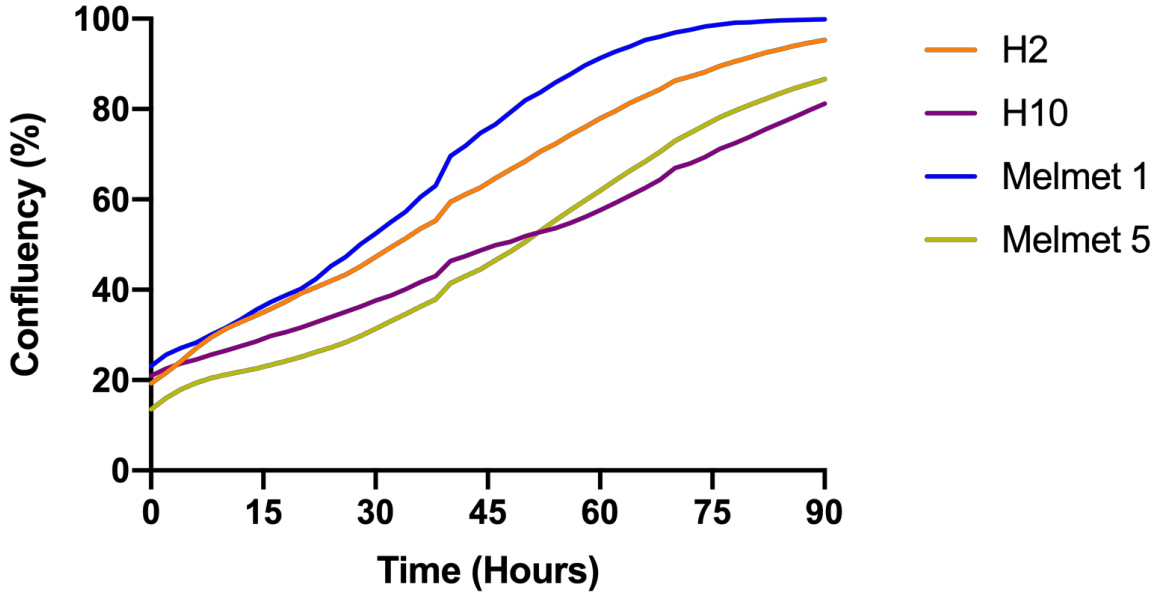

Figure 4.14 - Confluency progression of H2, H10, Melmet 1 and Melmet 5 cell lines. Confluency of the H2, H10, Melmet 1 and Melmet 5 cell lines measured over time in a 96-well plate with the IncuCyte system. H2, H10 and Melmet5 cells were plated with 10k cells/well and Melmet 1 was plated with 7.5k cells/well. Confluency percentage values are based on n = 3 with technical replicates ranging from 4-8 for each concentration of cells**.**

4.7 *In Vitro* Cell Cycle Analysis

To further study the proliferative capabilities, a cell cycle analysis was performed. Representative figures for cell cycle progression analysis for the H2, H10, Melmet 1 and Melmet 5 cell lines is displayed in Figure 4.15 with a Watson pragmatic analysis graphic showing distribution of cells in G0/1 in blue, S in yellow and G2/M phase in green. Table 4.7 displays the distribution of the H2, H10, Melmet 1 and Melmet 5 cell lines for each stage of the cell cycle. H10 showed the highest G0/G1 phase of all 4 cell lines at 70,99%, followed closely by H2 at 67,11%. Melmet 1 and Melmet 5 also followed each other in terms of the G0/G1 distribution, at 55,68% and 54,58% respectively. The S phase also follows in the same trend, with H2 and H10 at 23,41% and 17,07%. Melmet 1 and Melmet 5 cells seem to occupy the S phase more than G0/G1, being at 31,56% and 36,96%. Finally, during G2/M of the cell cycle, all four cell lines seemed to be relatively close, ranging from 8% to 11%. A one-way ANOVA showed statistically significant differences among the cell cycle groups when comparing with an α value of 0,05. While a *post hoc* t-test with Bonferroni correction showed a significant mean difference between H2 and H10, H2 and Melmet 1, H10 and Melmet 1 for the G0/G1 group. Significant mean difference was also shown for H2 and Melmet 5, H10 and Melmet 1, H10 and Melmet 5 for the S group. Finally, for the G2/M group, significant mean difference was shown for H10 and Melmet 5. All groups showed significance with a *p* value of < 0,0125. There is a miniscule sub G0/1 population for all the cell lines, which accounts for a < 1 % of all the populations. However, this population is not accounted for, as it is most likely attributed to apoptotic vessels near the G0/1 population.

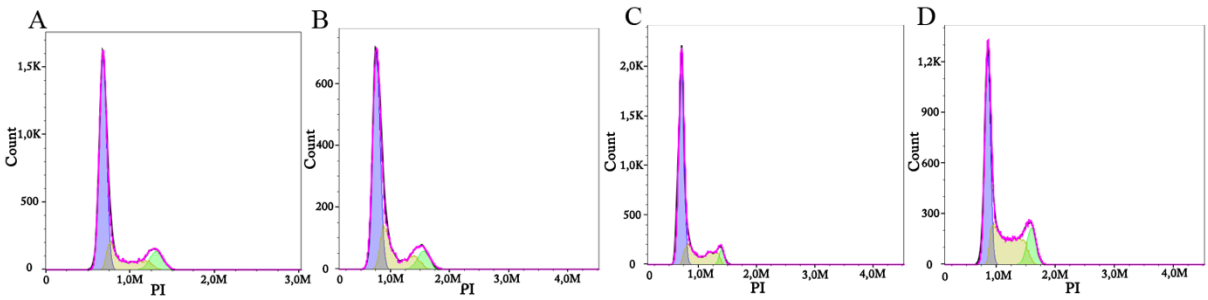

Fig 4.15 - Cell cycle distribution. A, B, C and D denotes H2, H10, Melmet1 and Melmet 5 cell lines respectively. The blue, yellow and green integrals indicates G0/G1, S and G2/M phase of the cell cycle respectively. All cells were stained with PI.

Table 4.7 - Cell cycle analysis statistics for H2, H10, Melmet1 and Melmet 5 cell lines. Percentages are mean values based on triplicate experiments conducted (n = 3) and brackets indicate the standard deviation.

	G0/G1 (%)	S (%)	G2/M (%)
H2	67,11 [2,55]	23,41 [2,24]	08,41 [2,29]
H10	70,99 [4,01]	17,07 [5,57]	10,66 [1,51]
Melmet 1	55,68 [8,22]	31,56 [8,15]	11,00 [4,10]
Melmet 5	54,58 [12,65]	36,96 [10,21]	07,19 [2,13]

4.8 *In Vitro* Apoptosis Analysis

To study the amount of cell death during *in vitro* culture, an apoptosis assay was conducted. Figure 4.16 displays apoptosis and necrosis values from a 70-80% confluent cell culture flask. Alive cells are detected in lower left quadrant, early apoptotic cells are detected in lower right quadrant, late apoptotic cells are placed in upper right quadrant and necrotic cells are shown in upper left quadrant. Table 4.6 shows the mean results from the triplicate experiments, displaying a live cell percentage from 89%-95%. The H10 cells showing the lowest live population at 89,93% and the highest apoptosis with both early and late apoptosis showing around 4-5%. A one-way ANOVA showed statistically significant differences among the cell line proliferation groups for early apoptosis with an α value of 0,05. While a *post hoc* t-test with Bonferroni correction showed significant mean differences between H10 and Melmet 1 in the early apoptosis group with a *p* value of < 0,0125.

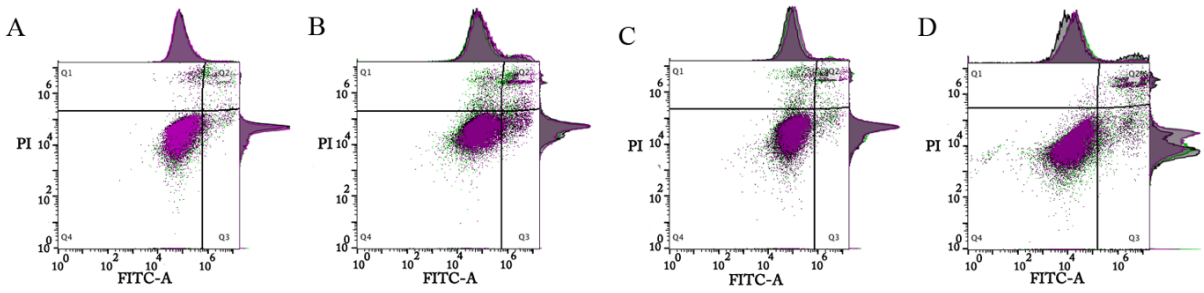

Fig 4.16 - Flow cytometry apoptosis assay. A, B, C and D denotes H2, H10, Melmet 1 and Melmet 5 cell lines respectively. Purple, black and green dots overlaid indicates the technical triplicate experiment conducted. Samples were stained with PI and FITC conjugated to Annexin-V.

Table 4.8 - Apoptosis assay statistics for H2, H10, Melmet1, Melmet 5 cell lines. Percentages are mean values based on n = 3, and brackets indicate the standard deviation.

	Live cells (%)	Early apoptosis (%)	Late apoptosis (%)	Necrosis (%)
H2	92,57 [2,34]	2,84 [0,90]	3,54 [1,50]	1,10 [0,65]
H10	89,93 [3,87]	4,62 [2,04]	4,19 [1,52]	1,30 [1,20]
Melmet 1	94,17 [3,49]	1,53 [1,17]	3,00 [1,86]	1,33 [1,19]
Melmet 5	93,08 [3,85]	2,50 [2,10]	3,94 [2,27]	0,56 [0,58]

5. Discussion

Around 20-40% of all systemic cancers produce brain metastases [63]. Brain metastasis is associated with a poor prognosis, with a median survival of around 1 month if left untreated and 3-4 months if treated [68]. The poor prognosis of brain metastases is often attributed to the almost impenetrable blood brain barrier and the inability of the hematological system to deliver most drugs across it [70]. Although stereotactic radiosurgery and conventional surgery encompass some of the main methods for dealing with brain metastases, the 10-year survival remains under 10% [70]. New therapeutic methods are needed, however they must be tested *in vivo* before being brought into the clinic. The goal of this project was to develop new *in vivo* brain metastasis models, for the pre-clinical development and testing of possible new therapeutics.

In this project, 5 animals were used in each cohort to screen for the metastatic ability of each tumor cell line, which is a reasonable compromise between workload and statistical validity of the results. Commonly, 10 mice have been used to achieve statistical valid results [119,120], and future work in our group will also increase the cohorts accordingly. However, since this was a pilot study to test the potential of most cell lines within the lab, 5 mice were chosen to minimize unnecessary expenses and animal euthanization.

In this project, we have developed 4 novel brain metastases models for further *in vivo* work and characterized these and additional cell lines.

5.1 Brain Metastatic Tumor Take in Mouse Brains

To study brain metastasis development in this project, the mice were injected ICD with a tumor cell suspension. The injection of tumor cells IV in the tail vein was not chosen based on the fact that metastasis then commonly appears in the lungs, and metastasis to the brain is only secondary [29]. Additionally, it would not be optimal for this project to have mice potentially suffering from morbidity symptoms due to lung tumors before proper visualization of brain tumors by MRI could be made. Injection of cancer cells directly into the brain (stereotactic orthotopic injection) was also considered, as there is a high probability of forming brain tumors and limiting the number of extracranial tumors. However, the physical relevance of such a method can be debated, as the cancer cells never crosses the BBB, thereby

not undergoing the necessary steps to categorize tumor growth as metastatic. One could argue that the injection of tumors by ICA would be the optimal way to induce brain metastases, as it has a very high success rate in producing brain metastases. However, ICA injection is a technically challenging injection method to do and it does not reflect the complete metastatic spread which an ICD injection does, since tumor cells mainly just go to the brain[121]. Therefore, it was decided tumor cell injection would be performed via ICD.

As shown in Table 4.2, injection of the tumor cells by ICD successfully resulted in brain metastases from the H2, H10, Melmet 1 and Melmet 5 cell lines. The majority of mice injected with the H3 and H9 cell line died immediately after injecting the cellular suspension, with only one mouse from the H9 cohort surviving (Figure 4.1). The death of the can most likely be attributed to clot formation (thrombosis) after cell injection. For future injections, low molecular weight heparin (LMWH) injected prior to injection of the cellular suspension might prevent thrombosis as discussed by Li and collegues[122]. Alternatively, one could also add LMWH into the cell suspension before injection. The slow growth of the H6 cell line prevented us from injecting these cells, as the cell line did not reach a high enough confluency and cell number. The proliferation rate of the cell line may be increased by the addition of more serum within the medium, or by changing the medium used to a neuronal cell medium to further mimic the extracellular fluid in the brains.

Extracranial tumors were also seen (Table 4.2) and locations were confirmed by histology from the extracted tissues. Organ collection was only conducted when visible tumors were observed during autopsy of the mouse carcasses. Tumor observations within the brain seemed to align with earlier published research, as Sundstrøm and colleagues detected brain tumor formation from 2-4 weeks by bioluminescence imaging when injecting the cellular suspension by ICD [123]. In our work, extracranial tumor formation was not problematic when regarding the H2, H10 and Melmet 1 cell lines, as the mice showed no morbidity symptoms for several weeks. The Melmet 5 cell line injected mice, however, did not develop large tumor numbers and volumes compared to the other models, potentially due to the observed extracranial tumor growth. Regarding organ collection, the Melmet 5 injected mice were the first to be euthanized, so organ collection was not started until after euthanizing the first two animals. The heart tumor detected in one of the Melmet 5 mice may be due to a mishap during the injection, where some tumor cells may have been arrested in the heart wall when pulling the needle out.

As previously shown by Sundstrøm within our laboratory group, the H1 cell line, injected at $5x10^5$ cells ICD, formed around 2-4 tumors by week 4, 2-10 tumors by week 6 and 3-20 tumors by week 8 [123]. Tumor numbers and volumes found in Figure 4.3 and 4.4 shows that the H2 cell line expanded less within the brain than the H1 line used by Sundstrøm. The H2 cell line produced one large tumor and a few very small ones within the brain, compared to the relatively large numbers of smaller tumors seen by injection of the H1 cell line. During earlier timepoints, such as week 4 and 6, the H10 injected mice seemed to show comparable tumor numbers to the H1 injected mice. However, by week 8, the tumor numbers for H10 was increased way beyond the H1 numbers. The histology of H10 tumors (Figure 4.6) showed an uncircumscribed and invasive growth, indicating that proliferating tumor cells could potentially be able to migrate within the brain and form additional metastases, leading to the increased tumor numbers seen within week 8. Melmet 1 injected mice seemed to harbor rapidly expanding tumors, compared to the H1 injected mice. This rapid expansion may be attributed to the large proliferative capabilities shown by the cell line *in vitro* (Figure 4.14.) Still, brain function of the mice appeared to be normal, with few neurological symptoms considering the high tumor load. The Melmet 5 injected mice seemed to develop fewer tumors and needed to be euthanized before the H1 injected mice, seemingly from the extracranial tumor burden.

In this work, the results indicated an inverse correlation between numbers of brain metastases and tumor volumes (see Tables 4.3 and 4.4, week 6). Similar findings have been described previously by Perera and colleagues, who injected breast cancer cell lines and studied brain metastases growth *in vivo,* by the use of MRI [124]. It was shown that when a cell line produces a high number of tumors, the volume of such tumors seems to be reduced. A large number of tumors may produce lesser volumes due to competition for resources within the brain. Inversely, fewer numbers of tumors may expand significantly more because there is more room for expansion before the intracranial pressure becomes too high [125].

5.2 Characterization of Brain Metastasis by MRI and Histology

A suitable brain metastasis model should produce an experimentally satisfactory amount and volume of tumors, without causing morbidity symptoms in the mice too early. In this context, a brain metastasis model showing multiple tumors with a survival time of 6 -10 weeks would

allow sufficient time to study treatment effects of novel targeted therapies, which is one of the major research aims of the Brain Metastasis Research Group (Prof. Frits Thorsen, personal communication).

MRI was used to study which tumor cell lines were able to colonize the brain, to determine the tumor numbers and volumes that developed from these cell lines, as well as to visualize the metastatic spreading patterns of the cell lines. The histology was used to confirm the metastatic spread seen by MRI, and to evaluate the invasiveness and vascularity of the individual tumors in more detail.

As seen by Table 4.3 and the MRI images illustrated in Figure 4.1, the H2 cell line only developed 1 brain metastasis at weeks 4 and 6, while 1-4 more tumors could be detected at later time points. In this respect, the H2 model may be regarded as a solitary brain metastasis model at early stages of tumor development, which to our knowledge has not been described in literature before, when tumor cells are injected directly into the blood stream of nod/scid mice. Such a model would be appropriate to use when studying the effects of stereotactic radiosurgery because of the large tumor presented by the cell line. Stereotactic frames used during radiosurgery are available for rodents, and thus the H2 model could be of interest for future radiation studies. The H2 model would likely not be suitable for studying targeted therapies, as the tumor number displayed is too low. The H2 model also seemed to reflect melanoma brain metastases patterns observed within human patients, as there was a distinct border between the tumor and the brain parenchyma, with no single cell invasion into the normal brain and no micrometastases detected by H&E [126].

The H2 model also verifies the need for multiple imaging sequences during evaluation of the brain tumor burden [127]. A combination of T2 weighted MRI, T1 weighted MRI before and after contrast injection was used in this project. The high vascularity of the H2 tumors could clearly be demonstrated on the MR images (Figure 4.1, bottom row). The MR data also indicates the breakdown of the BBB at later stages of tumor development (Figure 4.1, comparing bottom, middle picture with bottom, right picture), as a high contrast uptake could be seen.

For the H10 model, MRI images showed a high number of small tumors scattered throughout the whole brain (Figure 4.5). This is in line with clinical observations, as late stage melanoma

patients often have multiple lesions at first brain MRI, and subsequent, longitudinal MRI shows emergence of additional, new brain lesions [128] . In this work, tumor expansion over time could also be seen by MRI (Figure 4.4) for the H10 model.

The H10 model produced a very high number of tumors, as seen by MRI (Figures 4.4 and 4.5), indicating a more aggressive and/or diffuse growth pattern. The tumors did not load contrast very well, however the multi-sequence MRI was still able to detect the brain lesions. For instance, melanoma cells are known to be melanotic (produce melanin), which will disturb the MR signal intensity on T1 weighted MR images, thereby producing hyper intensive (paramagnetic) signal areas [129]. This could clearly be seen also in this project (Figure 4.4, upper row).

The more aggressive tumor growth was confirmed by histology, showing a diffuse spread of tumor cells within the whole brain, both manifested as single tumor cells and cell clusters of varying sizes (Figure 4.6). The diffuse clustering may explain the low visibility of the H10 tumors by MRI scans after contrast injections, as seen in Figure 4.4. The diffuse tumor cell spread is uncommon for brain metastases, however poorly defined borders and diffuse invasion patterns have been observed previously[130] . Some of the tumor cells appeared to grow around existing blood vessels in the brain (Figures 4.6B and 4.6C), thus indicating that the tumor cells relied more on vascular co-option than neo-vascularization for their nutrient supply. This is also in line with previous reports, showing that vascular co-option is more important than angiogenesis for the growth of melanoma brain metastases [131].

An interesting discrepancy between the H10 and Melmet 1 cell line can be seen in Figure 4.3 for the H10 cell line and Figure 4.6 for the Melmet 1. The tumors seemed to be more evident during T1-weighted MRI than T2-weighted MRI for the H10 cell line. This might be explained by minimal vascularization of the H10 cell line tumors, as also seen by Supplementary Figure 6.1 and 6.2. Tumors produced by the H10 might become more rigid, protein dense and fluid deficient compared to other cell lines such as the Melmet 1. Vascularization is also necessary for a large tumor development. This may explain why H10 tumors did not grow as large, as tumors grew until around 1-2mm^3 before growth was restricted, likely due to nutrient deficiencies [132].

This lack of vascularization for the H10 cell line may in some part be attributed to a mutation in the mammalian target of rapamycin (mTOR) protein, as seen in Supplementary Table 6.2. mTOR is a key protein in the PI3K/AKT/mTOR pathway, and this pathway is also involved in angiogenesis. The I388T substitution present for the H10 cell line in mTOR is contained within a domain of unknown function. It is therefore not known if the mutation present within mTOR causes signaling aberrations and thus affects induction of angiogenesis, but it is worth pursuing in the future.

The amount of brain metastases combined with a sufficient survival time of the mice (around 9 weeks), would make the H10 model suitable for testing out targeted therapies. Especially therapies which potentially could inhibit the invasive and migratory capabilities of the tumor cells.

Regarding the Melmet 1 model, a substantial tumor growth could be seen from week 6 to week 8 (Figure 4.7). Tumors not detected at week 6 grew to a detectable size before week 8, and a large leap in average tumor volume, from 5,8 mm^3 to 93,1 mm^3 was seen (Table 4.4). The tumors seemed to be highly permeable to the contrast agent, as indicated by hyperintense tumor areas on MRI (Figure 4.7, bottom right picture).

The histology supports the MRI data, showing multiple brain lesions of varying sizes scattered throughout the brain (Figure 4.9). Unlike the H10 model, there was a distinct border between the tumor and the brain parenchyma (Figure 4.9B). A clear tumor border seen in all tumors indicates that the tumor formation is likely not due to invasive tumor spread within the brain parenchyma. The tumor cells also seemed to grow by vascular co-option (Figure 4.9C). The data suggests that a larger tumor might evolve from clustered tumor collections expanding into a single large tumor, as seen in Figure 4.9A, over time. The clustering of tumors shown in Figure 4.9 is also an interesting insight to tumor distribution and formation. By observation, it looks like multiple CTCs have arrested within the tissue.

The amount of brain metastases combined with a sufficient survival time of the mice (around 8 weeks), would make the Melmet 1 model ideal for testing out targeted therapies.

Regarding the Melmet 5 model, tumor growth within the olfactory bulb was seen in week 5, while relatively few tumors could be detected within the brain parenchyma (Figure 4.10). All

mouse brains showed visible tumors by week 4. The Melmet 5 model produced tumors early, and the mice had to be euthanized early (week 5), most likely due to the number of extracranial tumors, specifically those situated in the lymph system. As evident by Figure 4.2, these tumors were not registered, as it was after this cohort processing that it was decided to start collecting extracranial organs for metastasis confirmation by sectioning and staining with hematoxylin.

The histological evaluation showed a characteristic tumor formation within the olfactory bulb (Figure 4.12C), with a brain parenchymal tumor formation in Figure 4.12B, by the putamen and the striatum. Again, tumor growth was circumscribed, and invasive, single tumor cells could not be detected.

The green arrows in Figure 4.1 indicates how tumors might be visualized differently during MRI. At week 8, it was often difficult to distinguish tumors by T1-weighted MRI prior to contrast injections, while by using T2-weighted MRI or and T1-weighted MRI after contrast injections, the tumors were clearly visualized by its high signal intensity. The difference in appearance is likely due to the fact that the chosen echo time (TE) used to pick up signals from T1 weighted imaging (TE 9 ms) induces a lower signaling intensity to water rich tissues, while the chosen TE (38 ms) for T2 imaging makes water rich tissues reaching a higher signaling intensity. Upon injection of the contrast agent with subsequent imaging by T1 MRI, water rich tissues such as the tumors will experience a faster increase in the T1 signal, resulting in hyperintensive signal areas. This phenomenon was also clearly seen for the Melmet 1 and Melmet 5 tumor cell lines (Figures 4.8 and 4.11, respectively).

5.3 Brain Metastasis Distribution

Interestingly, a diversity in tumor growth patterns to different anatomical brain regions was observed (Figure 4.13), indicating differences in anatomical/physiological and molecular interactions between the tumor cell lines and the brain microenvironment.

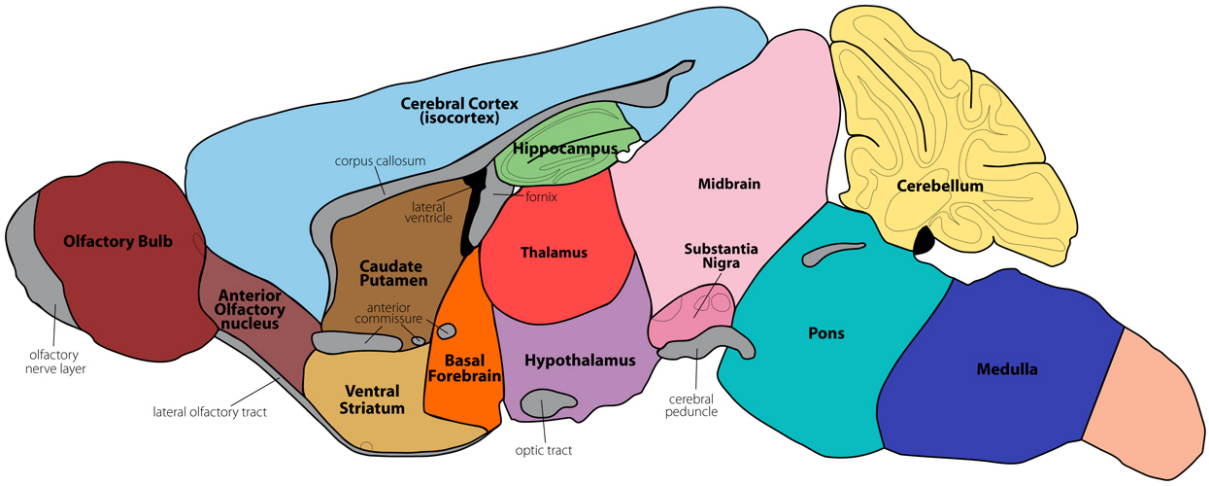

Table 5.1 – Mouse brain anatomy. An illustration of the mouse brain anatomy (sagittal section). The different parts of the cerebral hemispheres are shown, as well as the midbrain, pons, medulla (these 3 areas constitute the brain stem) and the cerebellum. Figure from blogs.brown.edu.

The observed distribution of tumors was based on MR images from week 5 for the Melmet 5 cell line, and week 6 for the H2, H10 and Melmet 1 cell lines (Figure 4.1). For all mice injected with the H2 cells, the tumors appeared to be situated close to the meninges in proximity to the hypothalamus, midbrain and pons. The observed metastatic growth of H2 cells in proximity to the meninges in mice brains may be explained by the growth pattern seen within the patient the cell line was originally derived from. This metastatic lesion was located within or in close contact to the meninges surrounding the brain, above the left orbital cavity, and expanded into the left frontal lobe (unpublished MRI data). This indicates there may be similar unknown molecular mechanisms interacting between tumor cells and the meninges in both the patient and derived mouse model.

The specific placement of the tumors by the hypothalamus, midbrain and pons may also be explained by a hematological spreading pattern. After injection of the tumor cell suspension into the left cardiac ventricle, the tumor cells are transported to the brain via the aorta to the arteria carotis communis before branching into the arteria carotis interna and externa. One of the first bypasses of the arteria carotis interna is in proximity to the hypothalamus, midbrain and pons, which may explain the localization of the H2 tumors. The molecular mechanisms behind this specific spread found in H2 cells and not the other tumor cell lines are yet to be determined.

H10 and the Melmet 1 tumor distribution showed a more commonly seen distribution within the brain. As mentioned in Chapter 1.8, brain metastases seem to follow an 80% distribution

into the brain cerebral hemispheres, 15 % into the cerebellum and meninges and 5% into the brainstem [66]. At week 6, there were no cerebellar tumors detected for the H10 cell line, although they appeared later during tumor development. In contrast, Melmet 1 had tumors arising in the cerebral hemispheres, cerebellum and brain stem as early as week 6. The observational differences might be caused by the H10 cell lines small diffuse tumor size, while tumors arising from the Melmet 1 cell line harbor a denser and clearer tumor border.

The Melmet 5 brain tumor distribution seemed to favor the olfactory bulb in the mice, however a small number of tumors were also seen within the brain parenchyma. Metastatic expansion within the olfactory bulb is quite contradictory to what has been previously reported by others, as one would expect the distribution to primarily be situated in locations with the highest blood flow (i.e. the cerebral hemispheres). Perera and his colleagues have previously described that the microenvironment of the olfactory bulb does not support the growth of brain metastases [121]. In this respect, our findings contradict their conclusion.

To explain the enigmatic directional tumor growth of Melmet 5 cells, we opted to consult our mutational data (Supplementary Figure 6.2). The Melmet 5 cell line contains mutations within the neurotrophic receptor tyrosine kinase 2 (NTRK2). NTRK2 produces a receptor protein called tropomyosin receptor kinase B (TrkB) present in the cellular membrane, which is necessary for brain-derived neurotrophic factor (BDNF) signaling [133]. BDNF is a growth factor that induces neuronal growth, survival of neurons and most importantly, proliferation of neuronal stem cells (NSC) [134]. While neuronal proliferation is not common within the adult mice brain, neurons of the olfactory bulb and neurons of the dendrite gyrus (found in the hippocampus) undergoes neurogenesis, to which BDNF signaling majorly contributes[135]. This could point towards an increased proliferation of the Melmet 5 cells in the olfactory bulb, stimulated by increased BDNF signaling in this area. Further experiments are needed to confirm this hypothesis, as the P481L and P507L mutations within TrkB are in a disordered protein domain and in a non-protein domain area of the protein.

5.4 Extracranial metastases

Some of the mice developed extracranial tumors. M1 from the H10 injected cohort had a tumor produced in its leg, most likely originating from the bone. M4 had tumor formation within the lymph system, inducing morbidity symptoms, which led to early euthanization.

Tumor formation within the heart was not expected, however tumor growth in the bone and the lymph nodes were not surprising. As the inoculation method for metastasis in this project was by ICD, the primary metastatic pathway is to the brain, and organs in the abdominal cavity (such as lymph nodes) and bone, as seen in Figure 1.4. Therefore, the extracranial tumors seen within these organs were anticipated. However, the tumor formation within the heart was not expected, and may be explained by cancer cells injected into the heart wall when retrieving the needle during inoculation. Such cancer spread is suboptimal, since it can induce earlier morbidity symptoms in the mice. This could however be avoided by letting the needle stay within the ventricle for a few more seconds after injection, before being retracted.

Commonly, extracranial tumors lead to early morbidity symptoms, which may be a potential problem when doing future drug testing with these models. Early morbidity symptoms in mice decrease the levels of brain tumor growth before the mice must be euthanized, and thus reduces the number of mice that can potentially be tested over a longer period of time. A way to circumvent early morbidity symptoms is serial passaging of brain metastatic cells in mice. This passaging will increase the metastatic cells homing ability to the brain, in turn diminishing their homing ability to other organs.

5.5 Mutational Analysis

To enable thorough, comprehensive characterization of the cell lines for future targeted drug testing in both *in vivo* and *in vitro* experiments, a mutational analysis was performed. The mutation table in Supplementary Figure 1.2 displays the genomic DNA mutation and the amino acid change in the protein expressed under the column AA change.

In general, the melanoma cell lines seemed to be recapitulate the mutational and transcriptional profiles reported for patient tumors [136]. Cell line models may therefore be regarded as genetically valid, compared to patient tumors. However, additional mutations may be acquired *in vitro,* due to different selection pressure on cells in culture [137].

The 5 most common somatic mutations found for melanoma is displayed in Table 4.6 [118]. BRAF V600E mutations were found in all cell lines except the H3 cell line. This accounts for an 85,7% frequency within the selected lines, which is substantially higher than the approximate 46% that is seen in the COSMIC databases. This may be explained by acquired

mutations during culture, small subclones of BRAF V600E mutated cells that have been selected for *in vitro*, or the fact that we worked with a smaller sample size, skewing our statistics. The L577F mutation found within BRAF of the H3 cell line was unexpected, as there is no previous description of this mutation in the COSMIC database. Thus, its oncogenic potential is not known, and further testing is required to understand the role of this mutation. The H3 cell line will nevertheless play an important role in future drug testing in our group, where effects of drugs targeting the BRAF V600E mutation can be compared to a cell line not harboring this mutation.

Mutations in CDKN2A were found for the H9 and H10 cell lines (i.e. 25% of our cell lines, as compared to 26% in the COSMIC database). H3 harbored an NRAS mutation (14% versus 14.3% in COSMIC), and PTEN was mutated within the H9 cell line (14% versus 15% in COSMIC). TP53 mutations were found in 3 of our cell lines (42,8%), compared to 15% in the COSMIC database.

In general, it has been established that melanoma has one of the highest mutation frequencies of all cancers, only behind lung cancer, which is also reflected in our mutational analysis (Supplementary Figure 6.2) [138]. A major benefit of having these genetically different cell lines is that it enables us to study a wide variety of targeted drugs *in vivo* and *in vitro.* Due to low passage numbers of our cell lines, they should be comparable to the genetic differences originally found in the patient tumors.

5.6 *In Vitro* Cell Proliferation

The proliferative capabilities of the cell lines were studied by a cell confluency assay (Figure 4.14). To properly assess the proliferative capabilities, both a confluency assay and a cell counting assay would be necessary, however, time did not permit the latter to be conducted. A cell counting assay would give both qualitative (cell growth patterns) and quantitative (cell numbers, cell doubling time) assessments of the proliferative capabilities of the cell lines. For instance, qualitatively, the Melmet 1 cell line tended to spread out more uniformly in culture, while the Melmet 5 line grew more in clumps.

A main motivation behind the cell proliferation assay was to assess whether growth *in vitro* and *in vivo* was comparable, as future experiments, such as testing of a new drug, would study

the inhibitory effects of the drug on tumor cell growth *in vitro* before performing animal experiments. Although relatively small animal cohorts were used, the *in vitro* data were relatively consistent with the *in vivo* results. For instance, the Melmet 1 cell line exhibited a high percentage of cells in S and G2/M phases (42.6%) and showed high tumor numbers and volumes in the mouse brain. Thus, the *in vitro* proliferation and *in vivo* tumor burden seemed to correlate for the cell lines.

To further substantiate the correlation between tumor cell growth *in vitro* and *in vivo*, we also tried to assess the tumor doubling time within the mouse brains. This parameter varied however strongly, depending on which time the MR volume data were obtained. For example, the tumor doubling time of H2 tumors varied between 4 and 30 days, depending on which weeks that were included in the analysis. Therefore, these data have not been included in this thesis. For future work, larger animal cohorts and weekly MRI should be used to assess tumor doubling time *in vivo* more accurately.

5.7 Flow Cytometry

5.7.1 Cell Cycle Analysis

Checkpoints within the cellular cycle helps maintain genomic stability, thereby preventing mutational development [139]. As cancer cells characteristically have a high frequency of genomic rearrangements, it is important to assess whether the different mutations found in our cell lines resulted in variations in advancement through the cell cycle [140].

There seemed to be a high population percentage in the S phase of the cell cycle for the Melmet 1 and the Melmet 5 cell lines. The two high percentage populations in the S-phase could indicate a G1 checkpoint failure or intra S-phase checkpoint inhibition. Checkpoint inhibition within the 2 Melmet cell lines was supported by the low percentage of cells within G0/G1 phase. G1 checkpoint failure can be derived from G1 checkpoint proteins being mutated, while intra S-phase inhibition can be caused by genomic mutations or replication failures that needs to be repaired, therefore slowing down cell cycle progression [141,142].

S phase accumulation for the Melmet 1 cell line is likely due to a limited ability of the cell line to repair DNA damage. Melmet 1 harbors a mutation within the Fanconi anaemia of

complementation group A (FANCA) gene. FANCA promotes DNA DS break repair by single-strand annealing and strand exchange [143]. The Melmet 1 line also contains two mutations within the NBN gene which produces the protein nibrin. Nibrin is involved in the repair of DSB within the genome. Melmet 1 cells do not seem to harbor mutations within G1 checkpoints. S phase arrest in the Melmet 1 cell line may thus be caused by multiple mutations within genomic repair proteins, with reduced ability to repair DNA damage.

The accumulation of Melmet 5 cells in the S phase could be due to mutations within the ATR or TP53 genes, seen in Supplementary Figure 6.2. This would be in accordance with what Paulovich and colleagues have shown, as Table 1 shows confirmed proteins involved in checkpoint fail or arrest within humans [144]. ATR normally induces DSB repair within the genome. Improper or delayed repair would thus inhibit transitioning into the G2/M phase. Melmet 5 also harbors a mutation within tumor protein 53 (p53). p53 is a major contributor to DNA repair [145]. P53 has also been shown to be responsible for G1 arrest during DNA damage [146]. The G134E mutation is located within the DNA binding domain of the p53 protein, responsible for DNA sequence binding. During binding to DNA, p53 stabilizes the DNA strands so that other proteins may interact with it and repair mutations. Mutations within p53 may therefore prevent G1 checkpoint inhibition and slow down cell cycle progression through S phase.

5.7.2 Apoptosis Analysis

The percentages of viable cells, apoptotic cells and necrotic cells are displayed in Table 4.8. The number of necrotic cells were low, varying between 0.6-1.3%. The percentages of viable cells were around 89-93% for all four cell lines, implying that the harvesting of cells at 70-80% confluency appears to be optimal, in order to avoid large, apoptotic subpopulations. The live cell populations were similar in size, except when comparing H10 and Melmet 5 cells for early apoptosis (4,62% versus 1,53%, $p < 0.0125$). However, the small, observed variations in early apoptotic cells does likely not have any practical value in future *in vitro* and *in vivo* experiments. Our results may thus be regarded as a basis for any future, apoptosis related experiments, for instance in drug testing. Our results also establish that if high numbers of apoptotic cells occur in future control experiments, this would likely be due to wrong use of protocols or wrong handling of the cells.

Conclusions

As a main conclusion, 4 novel mouse models were successfully generated, using the H2, H10, Melmet 1 and Melmet 5 human melanoma metastatic cell lines. The other cell lines tested did not meet the requirements that are needed for a reliable, induced brain metastasis model. The H3, H5 and H9 cell lines seemed to induce blood clots upon injection, and the H6 cell line did not grow well *in vitro.*

The mutational landscape of multiple cell lines was screened in order to elucidate questions about the tumor growth *in vivo,* and to obtain data for future targeted drug testing assays.

The 4 cell lines were then tested *in vitro.* The cell proliferation assay showed that the *in vitro* growth characteristics correlated with the growth patterns seen *in vivo*. The cell cycle assay by flow cytometry showed that the Melmet 1 and 5 lines were found to be situated in a relatively high S-phase percentage value compared to the H2 and H10 cell lines. The apoptosis assay by flow cytometry showed that there were not any abnormal apoptotic tendencies *in vitro*.

Future Prospects

Based on the results of this thesis, there is quite a lot of future work that could be performed. First, one could try to minimize the numbers of extracranial metastases by inducing a selection pressure on the tumor cells, so they primarily only to the brain. This is commonly done by intracardial injections of cells, followed by generating new cell lines from the brain metastasis, as previously explained. This is usually repeated 3 times in mice[147]. By this, the cell lines would experience a selection pressure by circulating in the bloodstream and from the microenvironment in the brain.

The potential genetic changes over time during the training procedure should be studied, to see if more aggressive brain tumor cell lines are developed. By doing mutational analysis panels for newly generated cell lines, as done in this project, one could study genetic changes as a result of the selection pressure. Mutations in genes encoding a more aggressive brain tumor phenotype might thus be discovered, which also opens up the possibility to test out other targeted therapies in the lab.

The differences in metastatic spreading patterns seen for the H2, H10, Melmet 1 and Melmet 5 cell lines also warrants further investigations. For instance, an immunohistological study could be performed, to understand in more detail the distribution patterns seen for the H2 cells (one large caudally situated tumor), H10 cells (diffuse, metastatic spread) and Melmet 5 cells (spread to the olfactory bulb).

6. Supplementary Figures

Table 6.1 – ROI converter. Code designed to read the exported text files from OsiriX containing the tumor ROIs. The code will register the total tumor number while also converting all radiuses registered to total volume by the input through the formula of a sphere. This code was written in Python.

```
import math

def con():

    # Open file and list values
    in_file = input("Filename (including .txt): ")
    file = open(in_file, 'r')
    lines = file.readlines()

    values = []
    for line in lines:
        if " mm" in line:
            value = line.strip()
            value = value.strip(' mm')
            values.append(float(value))

    # Calculates the total volume for all tumors
    volume = 0
    for diameter in values:
        radius = diameter/2
        volume += (4/3)*math.pi*math.pow(radius,3)

    # Print result
    print("Number of tumors: ", len(values))
    print("Total volume of tumors: ", round(volume, 3))
```

Table 6.2 – Mutational analysis of H2, H3, H5, H9, H10, Melmet 1, Melmet 5 cell lines. The selected cell lines were tested on a panel of 360 mutations. Shown in the table are the genes mutated, with the corresponding genetic mutation mutation. Some genetic mutations were not available, as it was not provided by the software. Amino acid changes are displayed as "AA change" in the table. Changes are marked as orange if they are known to be pathogenic drivers. The Cosmic ID is included for known pathogenic drivers.

Gene	g.DNA Mutation	AA Change	Cosmic ID	H2	H3	H5	H9	H10	Melmet1	Melmet5
ALK	29456463 C>T	G819R	-		x					
APC	112174853 C>T	P1188S	-		x					
ARID1A	N/A	S1490G	-							x
	N/A	S1707G	-							x
ARID1B	N/A	35_35del	-						x	x
ARID2	46233207 C>T	Q476X	COSM1512173	x						
ATR	N/A	S601F	-							x
ATRX	76776898 C>T	D2352N	COSM6959594		x					
	76939979 T>A	M257L	-		x					
AURKA	N/A	Y246H	-							x
BCL11A	N/A	M424I	-						x	
BRAF	140453999 G>A	L577F	-		x					
	140453136 A>T	V600E	COSM476	x		x	x	x	x	x
BRCA1	N/A	Q1064P	-						x	
	N/A	Q1111P	-						x	
BUB1B	40492533 C>T	S497F	-				x			
	N/A	P334L	-						x	
CDH20	59221758 C>T	Q746X	COSM5608087				x			
CDKN2A	21974702 T>A	N42I	COSM4428602				x			
	21971120 G>A	R80X	COSM12475					x		
CIC	42791278 C>T	P113	-	x						
	N/A	S545L	-						x	
	N/A	S1454L	-						x	
COL22A1	139788216 C>T	G599E	-	x						
CREBBP	N/A	A1869T	-						x	
	N/A	A1907T	-						x	
DDX3X	41204458 C>T	R351W	COSM3973666		x					
DICER1	95582064 AA -	L616fs	COSM6942696		x					
EGFR	55270250 G>A	R1068Q	COSM6947106		x					
EPHA3	N/A	P375Q	-							x
	N/A	P530L	-							x
EPHA6	N/A	P1031L	-							x
EPHA7	94120574 G>C	D159E	-	x						
ERBB2	N/A	A1186D	-						x	
	N/A	A1201D	-						x	
	N/A	A1216D	-						x	
ERBB4	N/A	E317D	-							x
ESR1	N/A	D321N	-							x
FANCA	N/A	C625S	-						x	
FBXO11	48046178 A>G	Y529H	-		x					

FGFR3	1804750 C>T	A347V	-			x				
FLT1	28885776 C>T	E1196K	-		x					
	28897065 C>T	E939K	COSM4540271			x				
FLT3	N/A	C625S	-						x	
	N/A	S404F	-							x
GABRG1	N/A	C281X	-							x
GUCY1A2	N/A	H244Y	-							x
HSP90AA1	102549409 T>A	K695X	-	x						
IGF2R	N/A	L1240V	-							x
IL7R	35876472 C>A	Q422K	-		x					
	35875648 C>T	H279Y	COSM3615754					x		
INSR	N/A	V1000M	-						x	
	N/A	V1012M	-						x	
IRS2	N/A	G882A	-						x	
	N/A	G879S	-						x	
KDM5A	N/A	P1645S	-							x
KDM6A	44937707 C>G	N965K	-	x						
KMT2C	N/A	E4319K	-							x
KMT2D	49433766 G>A	P2596L	-					x		
LTK	41799387 G>A	P422S	-		x					
MAP2K7	N/A	P213S	-							x
	N/A	P229S	-							x
MAP3K1	N/A	941_942del	-						x	x
MAP3K4	N/A	Q584H	-						x	
MAP4K4	N/A	D737Y	-							x
	N/A	D819Y	-							x
	N/A	D789Y	-							x
MED13	60088238 C>T	G547E	-		x					
MTOR	11307744 A>G	I388T	-					x		
MYO5B	N/A	V1703A	-						x	x
NBN	N/A	N558S	-						x	
	N/A	N640S	-						x	
NGFR	47590361 C>T	S425F	-					x		
NOTCH3	15302911 G>A	S180F	-		x					
NOTCH4	N/A	S727C	-							x
NRAS	115256528 T>A	Q61H	COSM586		x					
NTRK2	N/A	P491L	-							x
	N/A	P507L	-							x
OR5L1	N/A	C6F	-							x
PAX9	37145624 A>T	E331D	-				x			
PDGFRB	149498359 G>A	S952F	-		x					
PIK3C3	39647367 C>T	R847C	COSM988348				x			
PRDM1	N/A	D147N	-						x	
	N/A	D281N	-						x	
PREX2	N/A	G393E	-						x	
	N/A	R280K	-							x
	N/A	R297C	-							x
PRG4	N/A	A389T	-						x	
	N/A	A430T	-						x	
	N/A	A482T	-						x	
PRG4	N/A	L498P	-						x	
	N/A	L539P	-						x	
	N/A	L591P	-						x	
PTEN	89692908 C>T	T131I	COSM5104				x			
PTK6	62162259 G>A	P285L	-			x				
RICTOR	N/A	K541E	-						x	
	N/A	A766G	-						x	
ROBO2	77595585 C>T	A344V	-			x				
RRM2B	103238262 C>T	V69I	-	x						
SF3B1	N/A	P465S	-						x	
SFTPA1	N/A	V19A	-						x	
	N/A	V34A	-						x	
SLIT2	20541096 G>A	G622E	-			x				
TERT	N/A	Q961H	-							x
	N/A	Q1024H	-							x
TP53	7577538 C>T	R248Q	COSM10662		x					
	7576865 A>T	Y327X	COSM4398579				x			
	N/A	G134E	-							x
TP73	3649637 C>G	I635M	-			x				
	3649638 C>T	H636Y	-			x				
U2AF1	44515806 C>T	E83K	-		x					
XPA	N/A	R228Q	-							x
ZNF217	N/A	P450S	-						x	

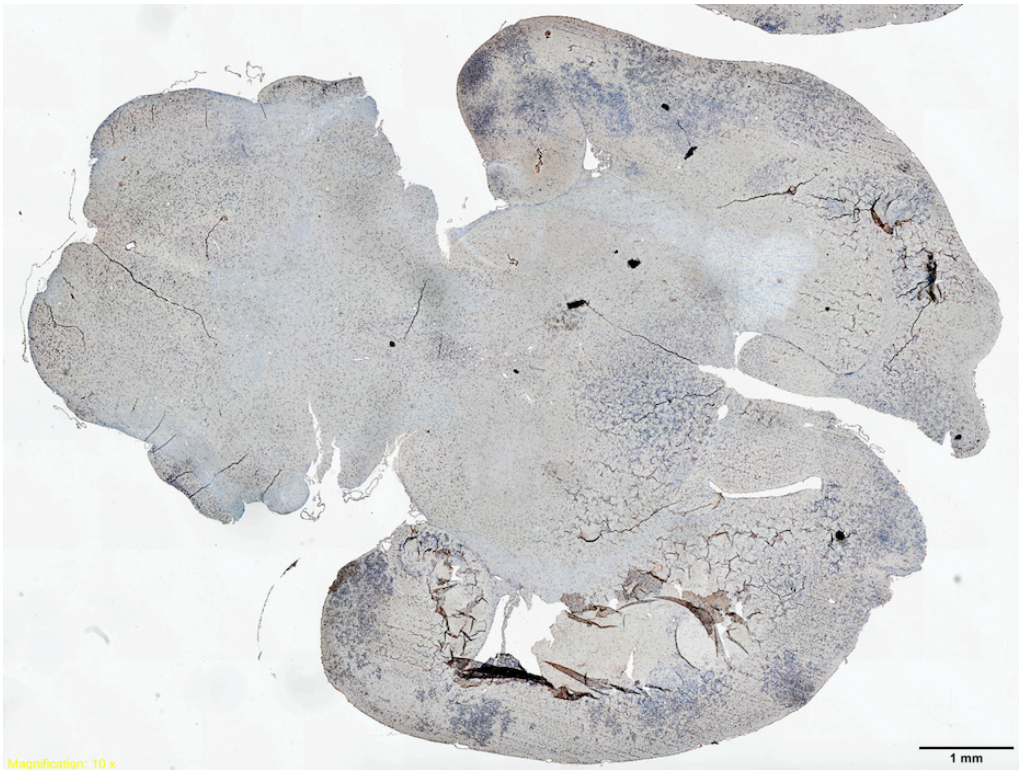

Figure 6.1 – H10 injected mouse brain (mouse M5, see also Figure 4.6 in results section) slice stained for CD34 and hematoxylin. The light microscopy images are color corrected after imaging. The image is a whole brain sliced in a transversal direction scanned at 10x. Scale bar = 1mm.

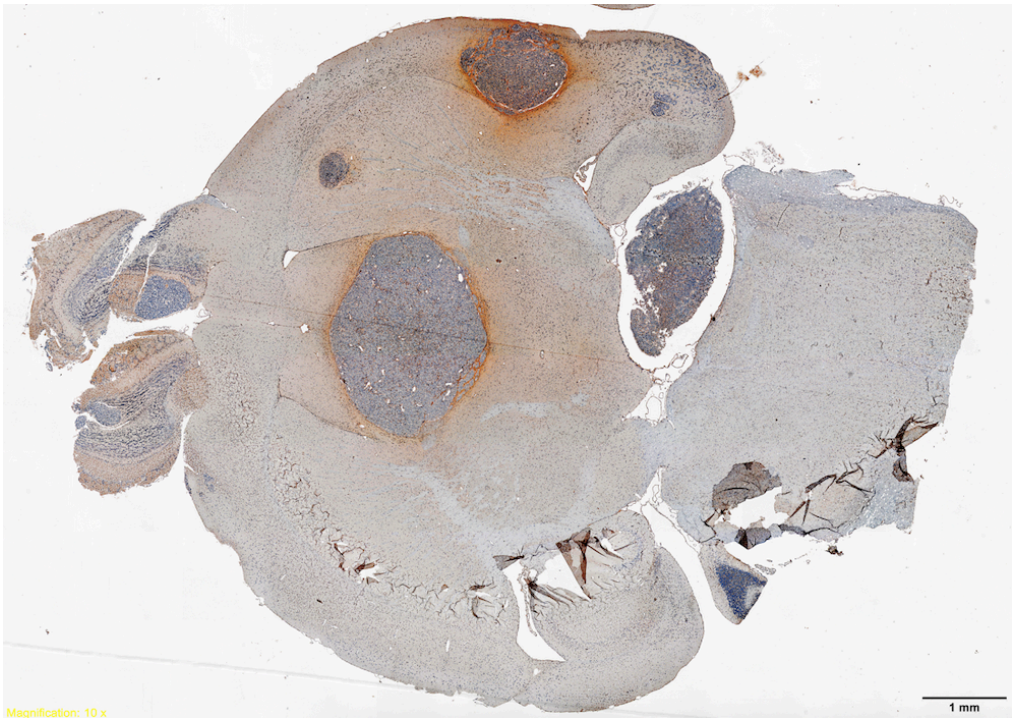

Figure 6.2 – Melmet 1 injected mouse brain (mouse M3, see also Figure 4.12 in results section) slice stained for CD34 and hematoxylin. The light microscopy images are color corrected after imaging. The image is a whole brain sliced in a transversal direction scanned at 10x. Scale bar = 1mm.

References

1. What are basal and squamous cell skin cancers. *Am. Cancer Soc.* 1–4 (2016). (Accessed: 27rd May 2019)
2. Reinau, D., Surber, C., Jick, S. S. & Meier, C. R. Epidemiology of basal cell carcinoma in the United Kingdom: Incidence, lifestyle factors, and comorbidities. *Br. J. Cancer* **111,** 203–206 (2014).
3. Cakir, B. Ö., Adamson, P. & Cingi, C. Epidemiology and Economic Burden of Nonmelanoma Skin Cancer. *Facial Plastic Surgery Clinics of North America* **20,** 419–422 (2012).
4. Garbe, C. & Leiter, U. Epidemiology of melanoma and nonmelanoma skin cancer-the role of sunlight. *Advances in Experimental Medicine and Biology* **624,** 89–103 (2008).
5. Cichorek, M., Wachulska, M., Stasiewicz, A. & Tymińska, A. Skin melanocytes: biology and development. *Postep. Dermatologii i Alergol.* **30,** 30–41 (2013).
6. Marks, R. Epidemiology of melanoma. Clinical dermatology . Review article. *Clin. Exp. Dermatol.* **25,** 459–463 (2000).
7. Matthews, N. H., Li, W.-Q., Qureshi, A. A., Weinstock, M. A. & Cho, E. *Epidemiology of Melanoma*. *Cutaneous Melanoma: Etiology and Therapy* (Codon Publications, 2017). doi:10.15586/codon.cutaneousmelanoma.2017.ch1
8. Meredith, P. & Riesz, J. Radiative Relaxation Quantum Yields for Synthetic Eumelanin. *Photochem. Photobiol.* **79,** 211 (2004).
9. Abbott, N. J., Patabendige, A. A. K., Dolman, D. E. M., Yusof, S. R. & Begley, D. J. Structure and function of the blood-brain barrier. *Neurobiol. Dis.* **37,** 13–25 (2010).
10. Pollitt, R. A. *et al.* The expanding melanoma burden in California hispanics: Importance of socioeconomic distribution, histologic subtype, and anatomic location. *Cancer* **117,** 152–161 (2011).
11. SEER*Explorer. Available at: https://seer.cancer.gov/explorer/. (Accessed: 23rd April 2019)
12. De Snoo, F. A. *et al.* Increased risk of cancer other than melanoma in CDKN2A founder mutation (p16-Leiden)-positive melanoma families. *Clin. Cancer Res.* **14,** 7151–7157 (2008).
13. Garbe, C. *et al.* Diagnosis and treatment of melanoma. European consensus-based interdisciplinary guideline - Update 2016. *Eur. J. Cancer* **63,** 201–217 (2016).
14. Chin, L., Garraway, L. A. & Fisher, D. E. Malignant melanoma: Genetics and therapeutics in the genomic era. *Genes and Development* **20,** 2149–2182 (2006).
15. Orlow, S. J. Melanosomes are specialized members of the lysosomal lineage of organelles. *Journal of Investigative Dermatology* **105,** 3–7 (1995).
16. Sullivan, R. J. & Fisher, D. E. Understanding the Biology of Melanoma and Therapeutic Implications. *Hematology/Oncology Clinics of North America* **28,** 437–453 (2014).
17. Mitra, D. *et al.* An ultraviolet-radiation-independent pathway to melanoma carcinogenesis in the red hair/fair skin background. *Nature* **491,** 449–453 (2012).
18. Karachaliou, N. *et al.* Melanoma: oncogenic drivers and the immune system. *Ann Transl Med* **3,** 265 (2015).
19. Hanahan, D. & Weinberg, R. A. Hallmarks of Cancer: The Next Generation. *Cell* **144,** 646–674 (2011).
20. Takeuchi, H. *et al.* Altered p16/MTS1/CDKN2 and cyclin D1/PRAD-1 gene expression is associated with the prognosis of squamous cell carcinoma of the esophagus. *Clin. Cancer Res.* **3,** 2229–2236 (1997).
21. Kunz, M. Oncogenes in melanoma: An update. *European Journal of Cell Biology* **93,** 1–10 (2014).

22. Mehnert, J. M. & Kluger, H. M. Driver mutations in melanoma: Lessons learned from bench-to-bedside studies. *Curr. Oncol. Rep.* **14,** 449–457 (2012).
23. Winder, M. & Virós, A. Mechanisms of Drug Resistance in Melanoma. in 91–108 (Springer, Cham, 2017). doi:10.1007/164_2017_17
24. Ascierto, P. A. *et al.* The role of BRAF V600 mutation in melanoma. *Journal of Translational Medicine* **10,** 85 (2012).
25. Forbes, S. A. *et al.* COSMIC: Somatic cancer genetics at high-resolution. *Nucleic Acids Res.* **45,** D777–D783 (2017).
26. Hodis, E. *et al.* A landscape of driver mutations in melanoma. *Cell* **150,** 251–263 (2012).
27. Davies, H. *et al.* Mutations of the BRAF gene in human cancer. *Nature* **417,** 949–954 (2002).
28. Rubinstein, J. C. *et al.* Incidence of the V600K mutation among melanoma patients with BRAF mutations, and potential therapeutic response to the specific BRAF inhibitor PLX4032. *Journal of Translational Medicine* **8,** 67 (2010).
29. Daphu, I. *et al.* In vivo animal models for studying brain metastasis: Value and limitations. *Clinical and Experimental Metastasis* **30,** 695–710 (2013).
30. Cirenajwis, H. *et al.* NF1-mutated melanoma tumors harbor distinct clinical and biological characteristics. *Mol. Oncol.* **11,** 438–451 (2017).
31. Boespflug, A., Caramel, J., Dalle, S. & Thomas, L. Treatment of NRAS -mutated advanced or metastatic melanoma: Rationale, current trials and evidence to date. *Therapeutic Advances in Medical Oncology* **9,** 481–492 (2017).
32. Sarkisian, S. & Davar, D. MEK inhibitors for the treatment of NRAS mutant melanoma. *Drug Des. Devel. Ther.* **12,** 2553–2565 (2018).
33. Kiuru, M. & Busam, K. J. The NF1 gene in tumor syndromes and melanoma. *Laboratory Investigation* **97,** 146–157 (2017).
34. Carriaga, M. T. & Henson, D. E. The histologic grading of cancer. *Cancer* **75,** 406–21 (1995).
35. Baas, P. Principles of cancer staging. in *Principles and Practice of Interventional Pulmonology* **10,** 117–123 (ecancer Global Foundation, 2013).
36. Byrd, D. R. *et al.* Final Version of 2009 AJCC Melanoma Staging and Classification. *J. Clin. Oncol.* **27,** 6199–6206 (2009).
37. Brain Tumor : Grades and Prognostic Factors. 1–3 (2017).
38. Cancer Staging. *National Cancer Institute* 1–4 (2010).
39. Hüsemann, Y. *et al.* Systemic Spread Is an Early Step in Breast Cancer. *Cancer Cell* **13,** 58–68 (2008).
40. Chambers, A. F., Groom, A. C. & MacDonald, I. C. Dissemination and growth of cancer cells in metastatic sites. *Nature Reviews Cancer* **2,** 563–572 (2002).
41. Onder, T., Talmadge, J. E., Weinberg, R. A., Karnoub, A. & Scheel, C. Adaptation versus Selection: The Origins of Metastatic Behavior. *Cancer Res.* **67,** 11476–11480 (2007).
42. Eger, A. & Mikulits, W. Models of epithelial-mesenchymal transition. *Drug Discovery Today: Disease Models* **2,** 57–63 (2005).
43. Kalluri, R. & Weinberg, R. A. The basics of epithelial-mesenchymal transition. *Journal of Clinical Investigation* **119,** 1420–1428 (2009).
44. Thiery, J. P. Epithelial–mesenchymal transitions in tumour progression. *Nat. Rev. Cancer* **2,** 442–454 (2002).
45. Kaushik, S., Pickup, M. W. & Weaver, V. M. From transformation to metastasis: deconstructing the extracellular matrix in breast cancer. *Cancer Metastasis Rev.* **35,** 655–667 (2016).

46. Pecorino, L. *Molecular Biology of Cancer, Mechanisms, Targets, and Therapeutics: Biology, Molecular biology*. **4,** (2015).
47. Van Zijl, F., Krupitza, G. & Mikulits, W. Initial steps of metastasis: Cell invasion and endothelial transmigration. *Mutation Research - Reviews in Mutation Research* **728,** 23–34 (2011).
48. Azevedo, A. S., Follain, G., Patthabhiraman, S., Harlepp, S. & Goetz, J. G. Metastasis of circulating tumor cells: Favorable soil or suitable biomechanics, or both? *Cell Adhesion and Migration* **9,** 345–356 (2015).
49. Potter, R. F. & Groom, A. C. Capillary diameter and geometry in cardiac and skeletal muscle studied by means of corrosion casts. *Microvasc. Res.* **25,** 68–84 (1983).
50. Bendas, G. & Borsig, L. Cancer Cell Adhesion and Metastasis: Selectins, Integrins, and the Inhibitory Potential of Heparins. *Int. J. Cell Biol.* **2012,** 1–10 (2012).
51. Nguyen, D. X., Bos, P. D. & Massagué, J. Metastasis: From dissemination to organ-specific colonization. *Nature Reviews Cancer* **9,** 274–284 (2009).
52. Deryugina, E. I. & Quigley, J. P. Matrix metalloproteinases and tumor metastasis. *Cancer and Metastasis Reviews* **25,** 9–34 (2006).
53. Patel, P. & Chen, E. I. Cancer stem cells, tumor dormancy, and metastasis. *Frontiers in Endocrinology* **3,** 125 (2012).
54. Pepper, M. S., Tille, J. C., Nisato, R. & Skobe, M. Angiogenesis and Tumor Metastasis. *Cell and Tissue Research* **314,** 167–177 (2003).
55. Groom, A. C. *et al.* Multistep Nature of Metastatic Inefficiency. *Am. J. Pathol.* **153,** 865–873 (2011).
56. Pardridge, W. M. Drug transport across the blood-brain barrier. *Journal of Cerebral Blood Flow and Metabolism* **32,** 1959–1972 (2012).
57. Allt, G. & Lawrenson, J. G. Pericytes: Cell biology and pathology. *Cells Tissues Organs* **169,** 1–11 (2001).
58. Ballabh, P., Braun, A. & Nedergaard, M. The blood-brain barrier: An overview: Structure, regulation, and clinical implications. *Neurobiology of Disease* **16,** 1–13 (2004).
59. Daneman, R. & Prat, A. The blood-brain barrier. *Cold Spring Harb. Perspect. Biol.* **7,** a020412 (2015).
60. Pardridge, W. M. The blood-brain barrier: Bottleneck in brain drug development. *NeuroRx* **2,** 3–14 (2005).
61. Brastianos, P. K., Curry, W. T. & Oh, K. S. Clinical discussion and review of the management of brain metastases. *JNCCN Journal of the National Comprehensive Cancer Network* **11,** 1153–1164 (2013).
62. Barnholtz-Sloan, J. S. *et al.* Incidence Proportions of Brain Metastases in Patients in the Metropolitan Detroit Cancer Surveillance System. *J Clin Oncol* **22,** 2865–2872 (1973).
63. Gavrilovic, I. T. & Posner, J. B. Brain metastases: Epidemiology and pathophysiology. *Journal of Neuro-Oncology* **75,** 5–14 (2005).
64. Barnholtz-Sloan, J. S. *et al.* Incidence Proportions of Brain Metastases in Patients in the Metropolitan Detroit Cancer Surveillance System. *J Clin Oncol* **22,** 2865–2872 (1973).
65. Bedikian, A. Y. *et al.* Predictive factors for the development of brain metastasis in advanced unresectable metastatic melanoma. *Am. J. Clin. Oncol. Cancer Clin. Trials* **34,** 603–610 (2011).
66. Sloan, A. E., Nock, C. J. & Einstein, D. B. Diagnosis and treatment of melanoma brain metastasis: A literature review. *Cancer Control* **16,** 248–255 (2009).
67. Delattre, J. Y., Krol, G., Thaler, H. T. & Posner, J. B. Distribution of Brain Metastases.

Arch. Neurol. **45,** 741–744 (1988).
68. Stelzer, K. Epidemiology and prognosis of brain metastases. *Surg. Neurol. Int.* **4,** 192 (2017).
69. Bhatia, S., Tykodi, S. S. & Thompson, J. A. Treatment of metastatic melanoma: an overview. *Oncology (Williston Park).* **23,** 488–96 (2009).
70. C.M., B. *et al.* Final version of the American Joint Committee on Cancer staging system for cutaneous melanoma. *J. Clin. Oncol.* **19,** 3635–3648 (2001).
71. Moser, R. P. & Johnson, M. L. Surgical management of brain metastases: how aggressive should we be? *Oncology (Williston Park).* **3,** 123–7; discussion 128, 134 (1989).
72. van Vliet, J. J., Hovestadt, A., Verbiest, H. B. C., Vecht, C. J. & van Putten, W. L. J. Dose-effect relationship of dexamethasone on Karnofsky performance in metastatic brain tumors: A randomized study of doses of 4, 8, and 16 mg per day. *Neurology* **44,** 675–675 (2012).
73. Chen, Z. *et al.* Assessment of stereotactic radiosurgery treatment response for brain metastases using MRI based diffusion index. *Eur. J. Radiol. Open* **4,** 84–88 (2017).
74. Patchell, R. A. *et al.* A Randomized Trial of Surgery in the Treatment of Single Metastases to the Brain. *N. Engl. J. Med.* **322,** 494–500 (1990).
75. Vecht, C. J. *et al.* Treatment of single brain metastasis: Radiotherapy alone or combined with neurosurgery. *Ann. Neurol.* **33,** 583–590 (1993).
76. Brown, J. M., Carlson, D. J. & Brenner, D. J. The tumor radiobiology of SRS and SBRT: Are more than the 5 Rs involved? *International Journal of Radiation Oncology Biology Physics* **88,** 254–262 (2014).
77. Lin, X. & DeAngelis, L. M. Treatment of Brain Metastases. *J. Clin. Oncol.* **33,** 3475–3484 (2015).
78. Lavine, S. D. *et al.* Gamma knife radiosurgery for metastatic melanoma: an analysis of survival, outcome, and complications. *Neurosurgery* **44,** 59-64; discussion 64–6 (1999).
79. Tsao, H., Atkins, M. B. & Sober, A. J. Management of Cutaneous Melanoma. *N. Engl. J. Med.* **351,** 998–1012 (2004).
80. Margolin, K. *et al.* High-Dose Recombinant Interleukin 2 Therapy for Patients With Metastatic Melanoma: Analysis of 270 Patients Treated Between 1985 and 1993. *J. Clin. Oncol.* **17,** 2105–2105 (2017).
81. Dummer, R. *et al.* Vemurafenib in patients with BRAFV600 mutation-positive melanoma with symptomatic brain metastases: Final results of an open-label pilot study. *Eur. J. Cancer* **50,** 611–621 (2014).
82. Hamid, O. *et al.* Ipilimumab in patients with melanoma and brain metastases: an open-label, phase 2 trial. *Lancet Oncol.* **13,** 459–465 (2012).
83. Garbe, C. *et al.* Combined Vemurafenib and Cobimetinib in BRAF -Mutated Melanoma. *N. Engl. J. Med.* **371,** 1867–1876 (2014).
84. Kim, K. B. *et al.* Survival in BRAF V600–Mutant Advanced Melanoma Treated with Vemurafenib. *N. Engl. J. Med.* **366,** 707–714 (2012).
85. Camacho, L. H. CTLA-4 blockade with ipilimumab: Biology, safety, efficacy, and future considerations. *Cancer Med.* **4,** 661–672 (2015).
86. Régina, A. *et al.* Multidrug resistance in brain tumors: Roles of the blood-brain barrier. *Cancer Metastasis Rev.* **20,** 13–25 (2001).
87. Cheon, D.-J. & Orsulic, S. Mouse Models of Cancer. *Annu. Rev. Pathol. Mech. Dis.* **6,** 95–119 (2011).
88. Vladutiu, A. O. The severe combined immunodeficient (SCID) mouse as a model for the study of autoimmune diseases. *Clin. Exp. Immunol.* **93,** 1–8 (2008).

89. Hansen, K. & Khanna, C. Spontaneous and genetically engineered animal models. *Eur. J. Cancer* **40,** 858–880 (2004).
90. Palmer, K. *et al.* Discovery and characterization of spontaneous mouse models of craniofacial dysmorphology. *Dev. Biol.* **415,** 216–227 (2016).
91. Talmadge, J. E., Singh, R. K., Fidler, I. J. & Raz, A. Murine models to evaluate novel and conventional therapeutic strategies for cancer. *American Journal of Pathology* **170,** 793–804 (2007).
92. Nødtvedt, A., Berke, O., Bonnett, B. N. & Brønden, L. Current status of canine cancer registration - report from an international workshop. *Vet. Comp. Oncol.* **10,** 95–101 (2012).
93. Pospischil, A., Grüntzig, K., Graf, R. & Boo, G. Spontaneous Animal Tumor Models. in 129–152 (2016). doi:10.1002/9783527695881.ch8
94. Talmadge, J. E., Singh, R. K., Fidler, I. J. & Raz, A. Murine models to evaluate novel and conventional therapeutic strategies for cancer. *American Journal of Pathology* **170,** 793–804 (2007).
95. Price, J. E., Tarin, D. & Fidler, I. J. Influence of organ microenvironment on pigmentation of a metastatic murine melanoma. *Cancer Res.* **48,** 2258–64 (1988).
96. Cekanova, M. & Rathore, K. Animal models and therapeutic molecular targets of cancer: utility and limitations. *Drug Des. Devel. Ther.* **8,** 1911–21 (2014).
97. Van Dyke, T. & Jacks, T. Cancer Modeling in the Modern Era. *Cell* **108,** 135–144 (2004).
98. Francia, G., Cruz-Munoz, W., Man, S., Xu, P. & Kerbel, R. S. Mouse models of advanced spontaneous metastasis for experimental therapeutics. *Nature Reviews Cancer* **11,** 135–141 (2011).
99. Uthamanthil, R., Tinkey, P. & De Stanchina, E. *Patient Derived Tumor Xenograft Models Promise, Potential and Practice.* (Academic Press, 2017).
100. Fidler, I. J. Selection of successive tumour lines for metastasis. *Nat. New Biol.* **242,** 148–149 (1973).
101. Cranmer, L. D., Trevor, K. T., Bandlamuri, S. & Hersh, E. M. Rodent models of brain metastasis in melanoma. *Melanoma Res.* **15,** 325–56 (2005).
102. Lowery, F. J. & Yu, D. Brain metastasis: Unique challenges and open opportunities. *Biochimica et Biophysica Acta - Reviews on Cancer* **1867,** 49–57 (2017).
103. Morse, D. L. *et al.* Development of an Orthotopic Human Pancreatic Cancer Xenograft Model Using Ultrasound Guided Injection of Cells. *PLoS One* **6,** e20330 (2011).
104. Hashemi, R. H., Bradley, W. G. & Lisanti, C. J. *MRI : the basics*. (Lippincott Williams & Wilkins, 2010).
105. Brown, M. A. & Semelka, R. C. *MRI : Basic Principles and Applications.* (John Wiley & Sons, Inc, 2011).
106. Lee, N. & Hyeon, T. Designed synthesis of uniformly sized iron oxide nanoparticles for efficient magnetic resonance imaging contrast agents. *Chemical Society Reviews* **41,** 2575–2589 (2012).
107. Bloch, F. Nuclear Induction. *Phys. Rev.* **652,** (1946).
108. Elster, A. D. An index system for comparative parameter weighting in MR imaging. *J. Comput. Assist. Tomogr.* **12,** 130–134 (1988).
109. De León-Rodríguez, L. M., Martins, A. F., Pinho, M. C., Rofsky, N. M. & Sherry, A. D. Basic MR relaxation mechanisms and contrast agent design. *J. Magn. Reson. Imaging* **42,** 545–65 (2015).
110. BIO-RAD. *Flow Cytometry Flow Cytometry Basics Guide*. (2016).
111. Shapiro, H. M. (Howard M. *Practical flow cytometry*. (Wiley-Liss, 2003).
112. Koopman, G. *et al.* Annexin V for flow cytometric detection of phosphatidylserine

expression on B cells undergoing apoptosis. *Blood* **84,** 1415–20 (1994).
113. Roederer, M. Spectral compensation for flow cytometry: visualization artifacts, limitations, and caveats. *Cytometry* **45,** 194–205 (2001).
114. Bagwell, C. B. & Adams, E. G. Fluorescence spectral overlap compensation for any number of flow cytometry parameters. *Ann. N. Y. Acad. Sci.* **677,** 167–84 (1993).
115. Yates, L. R. *et al.* Subclonal diversification of primary breast cancer revealed by multiregion sequencing. *Nat. Med.* **21,** 751–759 (2015).
116. Jones, D. *et al.* cgpCaVEManWrapper: Simple execution of caveman in order to detect somatic single nucleotide variants in NGS data. *Curr. Protoc. Bioinforma.* **2016,** 15.10.1-15.10.18 (2016).
117. Raine, K. M. *et al.* cgpPindel: Identifying Somatically Acquired Insertion and Deletion Events from Paired End Sequencing. *Curr. Protoc. Bioinformatics* **52,** 15.7.1-15.7.12 (2015).
118. Bello, D. M., Ariyan, C. E. & Carvajal, R. D. Melanoma mutagenesis and aberrant cell signaling. *Cancer Control* **20,** 261–281 (2013).
119. Hart, I. R., Talmadge, J. E. & Fidler, I. J. Comparative Studies on the Quantitative Analysis of Experimental Metastatic Capacity. *Cancer Res.* **43,** 400–402 (1983).
120. Hanna, N. & Fidler, I. J. Expression of metastatic potential of allogenic and xenogeneic neoplasms in young nude mice. *Cancer Res.* **41,** 438–44 (1981).
121. Lowery, F. J. & Yu, D. Brain metastasis: Unique challenges and open opportunities. *Biochimica et Biophysica Acta - Reviews on Cancer* **1867,** 49–57 (2017).
122. Li, J.-P. Heparin, heparan sulfate and heparanase in cancer: remedy for metastasis? *Anticancer. Agents Med. Chem.* **8,** 64–76 (2008).
123. Sundstrøm, T. *et al.* Automated tracking of nanoparticle-labeled melanoma cells improves the predictive power of a brain metastasis model. *Cancer Res.* **73,** 2445–2456 (2013).
124. Perera, M. *et al.* In Vivo Magnetic Resonance Imaging for Investigating the Development and Distribution of Experimental Brain Metastases due to Breast Cancer. *Transl. Oncol.* **5,** 217–25 (2012).
125. Hott, J. & Rekate, H. L. Intracranial Pressure. in *Encyclopedia of the Neurological Sciences* **30,** 744 (Springer-Verlag, 2014).
126. Kumar, V., Cotran, R. S. & Robbins, S. L. *Robbins Basic Pathology, 10E*. (2002).
127. Kierans, A. S., Leonardou, P., Shaikh, F. & Semelka, R. C. Body MR imaging: Sequences we use and why. *Appl. Radiol.* **38,** 7–12 (2009).
128. Aoyama, H. *et al.* Stereotactic radiosurgery plus whole-brain radiation therapy vs stereotactic radiosurgery alone for treatment of brain metastases: A randomized controlled trial. *J. Am. Med. Assoc.* **295,** 2483–2491 (2006).
129. Gaziel-Sovran, A., Osman, I. & Hernando, E. In vivo Modeling and Molecular Characterization: A Path Toward Targeted Therapy of Melanoma Brain Metastasis. *Front. Oncol.* **3,** 127 (2013).
130. Neves, S. *et al.* Pseudogliomatous growth pattern of anaplastic small cell carcinomas metastatic to the brain. *Clin. Neuropathol.* **20,** 38–42 (2001).
131. Thorsen, F. *et al.* Multimodal imaging enables early detection and characterization of changes in tumor permeability of brain metastases. *J. Control. Release* **172,** 812–822 (2013).
132. Hillen, F. & Griffioen, A. W. Tumour vascularization: Sprouting angiogenesis and beyond. *Cancer and Metastasis Reviews* **26,** 489–502 (2007).
133. Liu, H. & Song, N. Molecular Mechanism of Adult Neurogenesis and its Association with Human Brain Diseases. *J. Cent. Nerv. Syst. Dis.* **8,** JCNSD.S32204 (2016).
134. Tamura, M. *et al.* PTEN Interactions with Focal Adhesion Kinase and Suppression of

the Extracellular Matrix-dependent Phosphatidylinositol 3-Kinase/Akt Cell Survival Pathway. *J. Biol. Chem.* **274,** 20693–20703 (1999).
135. Pallotto, M. & Deprez, F. Regulation of adult neurogenesis by GABAergic transmission: signaling beyond GABAA-receptors. *Front. Cell. Neurosci.* **8,** (2014).
136. Vincent, K. M. & Postovit, L.-M. Investigating the utility of human melanoma cell lines as tumour models. *Oncotarget* **8,** 10498–10509 (2017).
137. Boesen, J. J. B., Niericker, M. J., Dieteren, N. & Simons, J. W. I. M. How variable is an spontaneous mutation rate in cultured mammalian cells? *Mutat. Res. - Fundam. Mol. Mech. Mutagen.* **307,** 121–129 (1994).
138. Maeda, H. & Khatami, M. Analyses of repeated failures in cancer therapy for solid tumors: poor tumor-selective drug delivery, low therapeutic efficacy and unsustainable costs. *Clin. Transl. Med.* **7,** 11 (2018).
139. Vermeulen, K., Van Bockstaele, D. R. & Berneman, Z. N. The cell cycle: A review of regulation, deregulation and therapeutic targets in cancer. *Cell Proliferation* **36,** 131–149 (2003).
140. Lengauer, C., Kinzler, K. W. & Vogelstein, B. Genetic instabilities in human cancers. *Nature* **396,** 643–649 (1998).
141. Iyer, D. R. & Rhind, N. The intra-S checkpoint responses to DNA damage. *Genes* **8,** 74 (2017).
142. Ye, X. *et al.* Defective S Phase Chromatin Assembly Causes DNA Damage, Activation of the S Phase Checkpoint, and S Phase Arrest. *Mol. Cell* **11,** 341–351 (2003).
143. Benitez, A. *et al.* FANCA Promotes DNA Double-Strand Break Repair by Catalyzing Single-Strand Annealing and Strand Exchange. *Mol. Cell* **71,** 621–628.e4 (2018).
144. Paulovich, A. G., Toczyski, D. P. & Hartwell, L. H. When checkpoints fail. *Cell* **88,** 315–321 (1997).
145. Shaw, P. H. The Role of p53 in Cell Cycle Regulation. *Pathol. - Res. Pract.* **192,** 669–675 (1996).
146. Kastan, M. B. *et al.* A mammalian cell cycle checkpoint pathway utilizing p53 and GADD45 is defective in ataxia-telangiectasia. *Cell* **71,** 587–597 (1992).
147. Ilhan-Mutlu, A. *et al.* Bevacizumab Prevents Brain Metastases Formation in Lung Adenocarcinoma. *Mol. Cancer Ther.* **15,** 702–710 (2016).